A Thesis Submitted for the Degree of PhD at the University of Warwick

Permanent WRAP URL:

http://wrap.warwick.ac.uk/165782
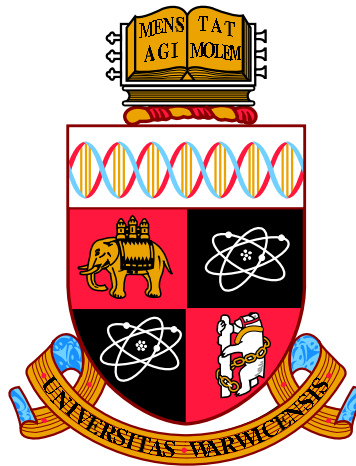
Studies of Electronic Structure of Novel Phenomena using Magnetic Compton Scattering

by

Daniel J O'Neill

Thesis

Submitted to the University of Warwick

for the degree of

Doctor of Philosophy

Department of Physics

September 2019

Contents

List of Tables

List of Figures

Acknowledgments

It is with much gratitude and appreciation that I, firstly, thank my Supervisor, Dr Jon Duffy. Without his great support and guidance over the last four years none of this would be possible. His enthusiasm for Physics in general and Compton scattering in particular has been inspiring. His willingness and readiness to provide help during the period of my PhD has been invaluable.

I would also like to thank all those friends and colleagues, from Warwick and the wider world of physics, who have provided support and encouragement.

Outside the world of physics I would like to thank my friends, whose support has been greatly appreciated. I would like to give a special thanks to Laura and Chris McIndo, with whom I started on this long road at Cardiff University some eight years ago. Their unwavering support and enthusiasm has helped me get through many a problem, even if this consisted of much needed trips to the pub for a drink and a quiz.

I would also like to thank my girlfriend, Rosie Hughes, who has put up with me through the entire PhD. Her constant support has been as indispensable in this thesis as it is in everything else.

Finally I would like to thank my parents whose unconditional support, both financially and more importantly emotionally, I have always been able to rely on. I would like to dedicate this thesis to them with all my love.

Declarations

This thesis has been submitted to the University of Warwick in support of my application for the degree of Doctor of Philosophy and has not been submitted either wholly or in part to any other institution. The thesis details my own independent research except where explicitly acknowledged in the text.

All the work took place in the Department of Physics under the supervision of Dr Jon Duffy in the period from October 2015 to October 2019

Abstract

In this thesis the spin densities of three groups of materials are investigated, these are $GdCo_{5-x}Ni_x$, $Nd_2Ir_2O_7$, and $NbFe_2$, primarily using the technique of Magnetic Compton Scattering, supported using magnetometry and density functional theory.

Four samples of the polycrystalline $GdCo_{5-x}Ni_x$ where $x = 1, 1.28, 2$, and 3 formed the first group with varying amounts of nickel replacing cobalt in the parent compound $GdCo_5$, a member of the $RETM_5$ class of materials (where RE is rare earth and TM is transition metal). The second group of materials, the pyrochlore iridate $Nd_2Ir_2O_7$, consisted of two samples. $Nd_2Ir_2O_7$ has attracted a great deal of interest due to its strong spin-orbital coupling, its electron correlations, and its much-debated metal to insulator transitions. Two different off-stoichiometric single crystal samples of $NbFe_2$ formed the final group of materials having a rich and complex phase diagram.

The experimental Magnetic Compton Scattering (MCS) investigations were carried out using the BL08W beamline at the SPring8 synchrotron in the Hyōgo prefecture in Japan which provided the high energy circularly polarised x-rays required for this technique.

Complementary experimental techniques were used to categorise the samples to provide further results in this study, such techniques included Superconducting Quantum Interference Device (SQuID) magnetometry, Vibrating Sample Magnetometry (VSM) and Laue Diffraction. The SQuID and VSM magnetometry were used to obtain the total moment of the samples which were then used with the measured spin moment to calculate the orbital moment to provide a more complete picture. Laue diffraction was used to align the single crystal measured to the required crystallographic direction. In addition, by using theoretical modelling techniques it was possible to separate the contributions to the total, spin, and orbital moments. The theoretical models were calculated using *ab initio* codes such as ELK, which use Density Functional Theory (DFT) methods. In addition to using the Compton profiles to investigate the magnetic properties and phases of the sample and contributing electrons, MCS was used to measure the spin moment of the samples at a range of temperatures, allowing the study of the temperature dependence of the total, spin and orbital moments.

Of the four $GdCo_{5-x}Ni_x$ samples that were investigated, two had compensation temperatures within the range measurable with the experimental setup. These experiments revealed the behaviour of the bulk spin moment at and around the compensation temperatures for both samples, as well as the behaviour of the moments on the sublattices. This sheds greater light on the samples, and could change the view on the compensation temperature and appropriate methods of measuring it. The third sample only had the single measurement at 300K but did not contradict the conclusions drawn from the other two samples. The fourth sample, $GdCo_2Ni_3$, did not replicate the pattern of the first three samples for its orbital moment, which requires further investigation.

As for the two $Nd_2Ir_2O_7$ samples, the contribution to the moments from the $4f$ electrons on the neodymium atoms were highly temperature dependent whereas the contributions to the moments from the $5d$ electrons on the iridium atoms were constant within error over the temperature range measured, 2K to 60K. Whilst this was expected, the spin to orbital ratio result for the iridium $5d$ atoms were found to be -1 which does not follow Hund's rules. Further experimentation is required to test the validity of the conclusion.

The iron rich sample of $NbFe_2$ ($Nb_{0.998}Fe_{2.002}$), was much more closely aligned to the ferrimagnetic stoichiometric configuration of the electronic structure calculations, than the ferromagnetic. In addition, of the configurations tested, the ferrimagnetic configuration using the LSDA functional best agreed with the data. This corresponds with the earlier MCS results, although there are other studies which have suggested that the result should be ferromagnetic. The debate would need more calculations, particularly using off-stoichiometric values, to resolve. The other sample of the $NbFe_2$ group, the niobium rich sample ($Nb_{1.004}Fe_{1.996}$) produced inconclusive results and thus did not show a clear distinction, largely because of insufficient data.

Abbreviations

AIAO All In All Out

AOAI All Out All In

DFT Density Functional Theory

FP-LAPW Full-Potential Linearised Augmented Planewave

GAMESS General Atomic and Molecular Structure System

GGA Generalised Gradient Approximation

LAPW Linearised Augmented Planewave

LSDA Local Spin Density Approximation

MCP Magnetic Compton Profile

MCS Magnetic Compton Scattering

MIT Metal to Insulator Transition

RE Rare Earth

RKKY Ruderman Kittel Kasuya Yosida

SCF Self-Consistent Field

SDW Spin Density Wave

SQuID Superconducting Quantum Interference Device

TM Transition Metal

VSM Vibrating Sample Magnetometer

XMCD X-Ray Magnetic Circular Dichroism

Chapter 1

Introduction

This thesis details the investigation into three groups of materials; $GdCo_{5-x}Ni_x$, $Nd_2Ir_2O_7$, and off-stoichiometric $NbFe_2$, using magnetic Compton scattering techniques. The purpose behind this work is to use magnetic Compton scattering and other, supporting techniques, along with theoretical methods to investigate the novel magnetic phases and properties of the above materials. The MCS technique uses high energy circularly polarised x-rays to directly probe the spin-polarised electron momentum density projected along one dimension; this is called a Compton profile. The theoretical techniques which have been used in this thesis to calculate theoretical Compton profiles, are Hartree-Fock and Density Functional Theory (DFT).

$GdCo_5$ belongs to the $RETM_5$ group of materials (where RE = rare earth and TM = transition metal). Some of the cobalt in this material is replaced with nickel in $GdCo_{5-x}Ni_x$. These materials are of note due to the interplay of the rare earth and transition metal electrons. Four samples where $x = 1$, $x = 1.28$, $x = 2$, and $x = 3$, were investigated. Previous work on these materials showed a transition, at a particular temperature (dependent on composition), where the direction of the spin on the gadolinium and the cobalt-nickel sublattices, which are antiparallel, flipped. In this thesis, it is shown that when the spin and orbital moments on the sublattices are investigated separately, the picture becomes more complicated.

Secondly, two nominally identical samples of the pyrochlore iridiate, $Nd_2Ir_2O_7$, were studied. $Nd_2Ir_2O_7$ has attracted a great deal of interest due to strong spin-orbit coupling and electron correlations and a much-debated metal to insulator transition. Previous work has highlighted that different samples of $Nd_2Ir_2O_7$, that are nominally identical, can behave in very different ways. This thesis aimed to investigate a few of these samples to investigate these discrepancies in greater detail. Outside factors limited the scope of this work, however we were able to show a significant discrepancy in the spin moment in the two samples investigated.

Finally, two slightly off-stoichiometric samples of $Nb_{1-y}Fe_{2+y}$ were looked at (where $y = 0.002$ and $y = -0.004$). These were chosen due to them being part of a rich phase diagram including several exciting phases and a proposed quantum critical point. Previous Compton scattering work looked at a sample of $Nb_{1-y}Fe_{2+y}$ where $y = 0.015$ and, contrary to other studies, found it to be in a ferrimagnetic state (rather than the expected ferromagnetic state). In this thesis the two samples investigated were expected to reach a spin-density wave (SDW) state at low temperatures, however were provisionally found to be in a ferrimagnetic state as well. This opens questions for further investigation discussed later in the thesis.

1.1 Compton Scattering

Compton scattering, as depicted in figure 1.1, is the inelastic scattering of a photon off an electron. The fact that it is inelastic scattering means there is a change in energy. This change is called the Compton shift.

The Compton shift can be expressed as

$$\Delta E = \frac{1}{2m_e} \left(\mathbf{p} + \hbar \left(\mathbf{k} - \mathbf{k}' \right) \right) = \frac{\hbar^2 \mathbf{q}^2}{2m_e} + \frac{\hbar \mathbf{q} \cdot \mathbf{p}}{m_e}, \tag{1.1}$$

where $\mathbf{p}$ is the initial momentum of the electron, $\mathbf{k}$ and $\mathbf{k}'$ are the incoming and scattered wavevectors respectively, $\mathbf{q}$ is the scattering wavevector ($\mathbf{q} = \mathbf{k} - \mathbf{k}'$), m_e
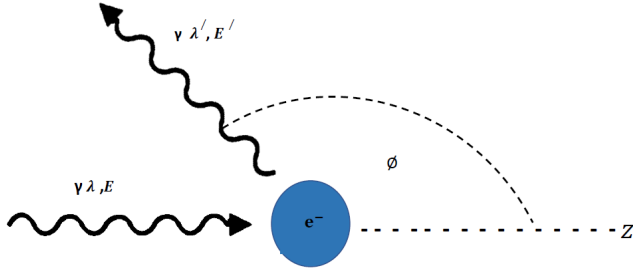
Figure 1.1: Sketch of the Compton scattering process

is the mass of the electron, and $\hbar$ is the reduced Planck's constant.

Magnetic Compton scattering expands on this by measuring a sample in a magnetic field with high energy circularly polarised x-rays. The external field applied to the sample is flipped between measurements and the difference measurement can produce a magnetic Compton profile. The magnetic Compton profile is only dependent on the unpaired electrons in a system and therefore with calculations, modelling, and data analysis it is possible to gain insight into the magnetic properties and phases of a system.

1.2 Motivation

A constant theme across the three series of samples is the extent to which the magnetic structure and properties are dependent on their composition. With $GdCo_{5-x}Ni_x$, varying amounts of cobalt are replaced with nickel from the parent compound $GdCo_5$. This has a fundamental effect on the magnetic properties as at low temperatures $GdCo_5$ is ferrimagnetic with the cobalt sublattice aligned with the field whilst $GdNi_5$ is ferrimagnetic with the gadolinium aligned with the field. This change happens at $x \approx 1$. Furthermore, the different temperature dependences of the sublattices creates an interesting bulk temperature dependence. The differences seen in the two nominally identical samples of $Nd_2Ir_2O_7$ have been attributed to slight

changes in the stoichiometry, likely caused by different growth methods. With the $Nb_{1-y}Fe_{2+y}$ series a rich and complex phase diagram is composition driven, going through several distinct phases as the series progresses from niobium rich to iron rich.

Some compositions of $GdCo_{5-x}Ni_x$ have a temperature at which the moment on the gadolinium sublattice, which is much more temperature dependent than the cobalt-nickel $3d$ moment, becomes smaller than the moment on the cobalt-nickel sublattice. This is defined as the compensation temperature and is often given as the temperature at which the minimum of the total moment is located. This is not necessarily the temperature at which the sublattices compensate for each other. In this thesis, Compton scattering is used to find the spin moment at a range of temperatures. This allows the temperature dependence of the total, spin, and orbital moments to be studied, especially the behaviour around the compensation point. In addition, it is possible through modelling the Compton profiles to separate out the contributions to the total, spin and orbital moments from the gadolinium $4f$ sublattice and the cobalt-nickel $3d$ sublattice. Being able to discern the behaviour of the individual contributions will aid the understanding of this series of materials. Compton scattering provides a way of separating the bulk, spin and orbit moments that form the bulk total moment obtained from SQuID magnetometry. Once again, as with $GdCo_{5-x}Ni_x$, by modelling the profiles from the magnetic electrons the contributions from the neodymium $4f$ and the iridium $5d$ electrons can be separated out.

The rich phase diagram of $Nb_{1-y}Fe_{2+y}$ has raised significant debate. In this thesis, theoretical Compton profiles, obtained from the *ab inito* DFT code, ELK, and using different ground states, can be fit to the experimentally obtained Compton profile to find the ground state which best matches the data.

4

1.3 Chapter Overview

Chapter 2 covers the theoretical aspects of this thesis, starting with the theory behind the Compton effect and the concepts of scattering cross sections. This is followed by a discussion of how electrons behave within a crystal. Various forms of magnetism are introduced, including the electronic interactions associated with them. The chapter concludes with an exploration on the theoretical aspects of the magnetic Compton scattering technique and the magnetic Compton profiles.

In Chapter 4 the experimental and computational techniques are investigated. Firstly the two codes used in this thesis are discussed, ELK and GAMESS, briefly summarising the models these codes are built on and the key parameters required for convergence, as well as where in the thesis each code is used to provide computational Compton profiles that support the experimentally produced profiles. Next the history of magnetic Compton scattering is discussed followed by details on the experimental setup used for this thesis. Finally, a brief overview of the techniques used for the characterisation of samples is included.

Chapter 5 involves the study of a series of samples that belong to the $RETM_5$ group of materials. These materials have the formula $GdCo_{5-x}Ni_x$ where $x = 1$, $x = 1.28$, $x = 2$, and $x = 3$. Magnetic Compton profiles were obtained at a large number of temperatures to investigate the effect of temperature on the spin moment of the samples. Concurrence was found with earlier work on these materials. Transition temperatures, where the total spin moment changes sign as well as the sign of the antiparallel contributions from the $3d$ and $4f$ sublattices, were found in the $x = 1.28$ and $x = 2$ samples.

Chapter 6 details the investigation into two nominally identical samples of $Nd_2Ir_2O_7$. Strong spin-orbit coupling, and electron correlations dominate the magnetic properties seen in this system. In this chapter the spin and orbital moments from the $5d$ electrons from iridium and the $4f$ electrons from neodymium are sepa-

rated out.

Chapter 7 is the final experimental chapter, discussing the itinerant ferromagnet $NbFe_2$. $NbFe_2$ has a complex and rich phase diagram, going through several different ground states dependent on slight variations to the stoichiometry. In this chapter two samples were investigated, $Nb_{0.998}Fe_{2.002}$ and $Nb_{1.004}Fe_{1.996}$. The phases of these two slightly off-stoichiometric samples were tested.

Chapter 8 summarises this thesis and the work within it. This chapter also discusses ideas for future work and experiments that could be performed on the samples to further understanding.

Chapter 2

Compton Scattering Theory, Crystals, Electrons, and Magnetism

In this chapter the theory and history of magnetic Compton scattering as a technique, including the Compton effect, scattering cross-sections and Compton profiles, are discussed. In addition some aspects of condensed matter physics such as the theory of crystalline solids, how electrons behave in these solids, and the magnetism that can arise from this behaviour are discussed to give a grounding on what this technique is used for.

To begin with, as the magnetic Compton scattering technique is key to this thesis, the Compton effect that forms the basis of this technique is discussed.

2.1 The Compton Effect

The main effect discussed throughout this thesis is Compton scattering. A process where a photon scatters inelastically off a charged particle. This forms the basis of the knowledge used in the processes and techniques studied [1]. However, within

this thesis it is intended to look solely at the electron as the charged particle, a diagram of this interaction is seen in figure 2.1.
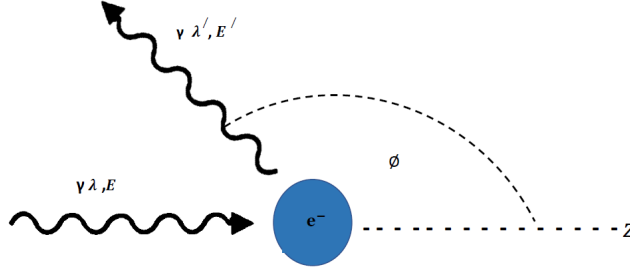
Figure 2.1: Sketch of a scattering event between a photon, γ, and an electron.

There is a change in energy, termed the Compton shift, which occurs during the collision of the photon and electron. In addition to this, the direction of the scattered photon alters from its original trajectory [2]. This Compton shift can be written as:

$$\Delta E = E - E' = E - \frac{E}{1 + \left(\frac{E}{m_e c^2}\right)(1 - cos\phi)} \tag{2.1}$$

where E is the energy of the incoming photon, E' is the energy of the scattered photon and therefore ΔE is the change in energy. E' can be calculated for the experimental configuration used in this thesis by using these equations. However, it is also possible to directly observe E' experimentally by measuring the energy of the Compton peak as discussed below.

As energy can be converted into wavelength, this Compton shift can also be written as a wavelength shift. However, as this is of less use to our investigations the shift will be discussed only in terms of energy.

This simplified picture assumes a stationary electron with no momentum, which would give a delta function-like peak at E', but broadened by the energy range of the incoming beam, the range of scattering angles that can reach the detector,

8

the resolution of the detector, and other such experimental factors. This peak would be much narrower than the observed profile since the broadening of the observed peak is as a result of the motion of the electrons in the sample, whilst the shape of the observed peak gives information about the electronic structure of the material being investigated.

2.2 Effect of Electron Momentum on the Scattered Photon

In order for the Compton shift equation to be useful and closer reflect the experimental reality it needs to incorporate additional parameters. One of these is the momentum of the electron. The probability of a scattering event should also be considered. The simplified equation discussed above is limited by its assumption that the electron is stationary. When the momentum of the electron is discussed, the peak broadens in a doppler shift. The peak of the observed 'Compton peak' is still at the energy of this stationary electron example as the average of the momenta would be 0. However, this broadening of the peak represents the full range of momenta in the system The shift in energy due to the Compton scattering can now be written as

$$\Delta E = \frac{1}{2m_e} \left[\left(\mathbf{p} + \hbar \left(\mathbf{k} - \mathbf{k}' \right) \right)^2 - \mathbf{p}^2 \right] = \frac{\hbar^2 \mathbf{q}^2}{2m_e} + \frac{\hbar \mathbf{q} \cdot \mathbf{p}}{m_e} \tag{2.2}$$

This equation now takes into account the momentum of the electron in the collision, $\mathbf{p}$ ($\mathbf{k}$ and $\mathbf{k}'$ are the incoming and scattered wavevectors, respectively, and $\mathbf{q}$ is the scattering wavevector ($\mathbf{q} = \mathbf{k} - \mathbf{k}'$)). As can be seen this equation has two terms. the first corresponds to the original Compton shift equation, i.e. when the momentum of the electron is 0 with respect to the photon. The second term represents the broadening discussed above. For a single scattering event, as this equation describes, this either reduces or increases the Compton shift depending on

the momentum of the electron in the collision. A large number of photons scattering off a large number of electrons with different momenta gives a broadening of the profile centred about E'.

While the equation now better reflects the realities of a single scattering event it is still simplified in respect to the complexities of an entire system. These will be discussed in later sections.

2.2.1 Scattering Cross Section

To start describing an entire system we now need to discuss the likelihood of a scattering event occurring. To do this we will look at the scattering cross section as this is proportional to the probability of this event. In this section we will discuss three different models and their corresponding cross sections. These examine increasingly complex systems until we reach the Compton cross section which will accurately describe our system and can lead to parameters that closer match reality.

The first cross section to be considered is the Thomson scattering cross section, a non-relativistic model. This cross section is only dependent on the radius of the electron and the scattering angle. However, this would not accurately describe the interactions in this thesis as, at the energies used in Compton scattering, a cross section need to include relativistic effects.

The Klein-Nishina (KN) cross section [3] takes into account relativistic effects and in addition to the scattering angle of the photon, it takes into account the energy of the photon. This is shown clearly in figure 2.2 when the KN cross section is plotted for different energies, including those used experimentally. At lower energies, such as 5.11KeV on the figure, this tends towards the simpler Thomson cross section.

The KN cross section is an improvement, at the energies used in this thesis, on the Thomson model but still does not take into account any properties of the electron. This effectively describes a compton scattering event only if the electron completely stationary. To describe the Compton scattering events a cross section

10
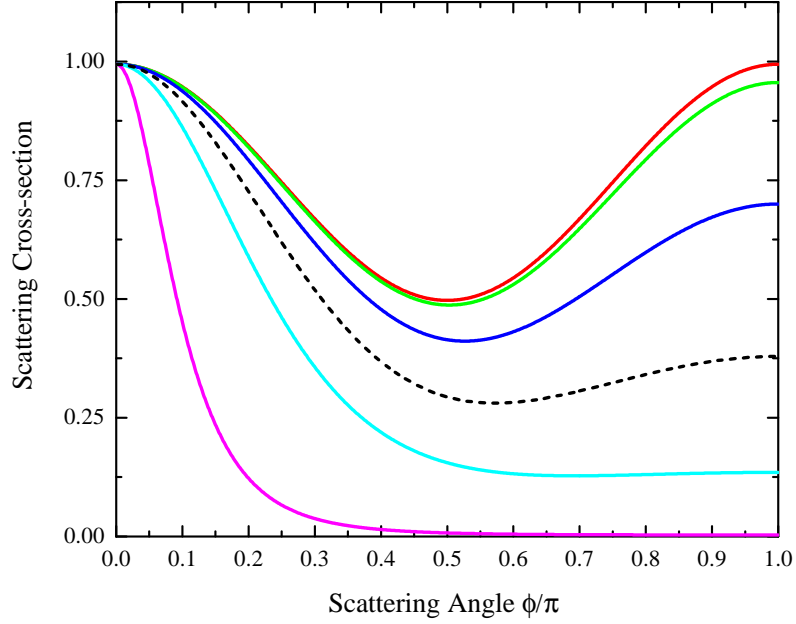
Figure 2.2: Cross-section against energy. Thomson cross section in red, KN cross section with an incident energy of 5.11KeV, 51.1KeV, 511KeV, and 5.11MeV are in green, blue, cyan, and magenta respectively, and 175KeV is black dashed (experimental incident energy)

that includes the momentum of the electrons is necessary. For this the Compton cross section needs to be defined [4; 5]. This cross section can be written as

$$
\begin{aligned}
\frac{d\sigma}{d\Omega}_{Compton} = \frac{r_e^4}{4}\frac{k'^2}{k^2}\Big[&\left(1 + \cos^2\phi\right) + \Delta\mathbf{k}\left(1 - \cos\phi\right) \\
&+ \xi_1 \sin^2\phi - \xi_3\left(1 - \cos\phi\right)\left(\mathbf{k} + \mathbf{k}'\cos\phi\right)\hat{\varsigma}\Big]
\end{aligned}
\tag{2.3}
$$

where ξ_1 and ξ_3 are the Stokes parameters for linearly and circularly polarised light and $\hat{\varsigma}$ is the unit vector for the direction of the electron spin. It is then possible to split this into two cross sections, dependent and independent of the spin, as shown in equations 2.4 and 2.5 respectively.

$$
\frac{d\sigma}{d\Omega}_{mag} = \frac{r_e^4}{4}\frac{k'^2}{k^2}\left(-\xi_3\left(1 - \cos\phi\right)\left(\mathbf{k} + \mathbf{k}'\cos\phi\right)\hat{\varsigma}\right)
\tag{2.4}
$$

$$
\frac{d\sigma}{d\Omega}_{charge} = \frac{r_e^4}{4}\frac{k'^2}{k^2}\left(\left(1 + \cos^2\phi\right) + \Delta\mathbf{k}\left(1 - \cos\phi\right) + \xi_1 \sin^2\phi\right)
\tag{2.5}
$$

11

As shown in these two equations, if the helicity of the circular polarisation, ξ_3, or the direction of the electronic spin, $\hat{\varsigma}$, is flipped then the sign of equation 2.4 changes whilst equation 2.5 remains the same. If circularly polarised photons are used to obtain Compton profiles a difference can be determined, making it possible to isolate the spin-dependent term. Consequently, if two Compton profiles are obtained, before and after flipping either the helicity or the external field (which would change the spin on the electrons), then the difference between these profiles can be obtained (cancelling out the charge term) to leave twice the magnetic Compton profile, implying equation 2.6.

$$\frac{d\sigma}{d\Omega}_{\uparrow} - \frac{d\sigma}{d\Omega}_{\downarrow} = 2\frac{d\sigma}{d\Omega}_{mag} \tag{2.6}$$

At this point a step back, and a discussion of crystals that the magnetic Compton scattering technique used to investigate, is now required as the behaviour of these crystalline solids affects the properties that this techniques measures.

2.3   Crystals

All of the samples used throughout this thesis are crystalline solids, characterised by their highly ordered structure, with the arrangement of atoms forming a crystal lattice. [6] Therefore it is important at this point to discuss this arrangement, also, called the crystal structure.

2.3.1   Real and Reciprocal Space Crystal Structure

There are two ways of describing this structure: one in real space and one in reciprocal space. In both cases these are described by the simplest, or smallest, repeating section. The repetition of this can be used to describe the entire crystal. In real space this is called the unit cell and in reciprocal space it is called Brillouin zone.

Real Space Crystal Structures

To define the crystal structure in real space there are three main pieces of information required: the space group, the Wyckoff positions and the lattice parameters and angles.

Firstly, the space group is a way of describing the arrangement of atoms within the unit cell. There are 230 unique space groups which are derived from 14 types of lattices named Bravais lattices. These lattices include, for example, simple cubic, face centred cubic, hexagonal, and triclinic amongst others.

The second piece of information required is the Wyckoff position. These describe the positioning of atoms and elements within the space group. Whilst these are always necessary these become vital when describing complex space groups or crystals with multiple elements.

The last piece of information required to completely describe the unit cell are the lattice parameters and angles. These lattice parameters detail the size of the unit cell and, for simplicity, are often used as the axes of the structure. Therefore, they can be used to describe any point within the crystal. The lattice angles are sometimes already defined by the Bravais lattice, as $90°$ or $120°$. However, they are required for lattices where this is not defined.

Reciprocal Space Crystal Structure

As stated above, the crystal structure can be defined in reciprocal space as well as real space. There are many analogous parameters, such as the Brillouin zone rather than the unit cell, as discussed above, and reciprocal vectors take the place of real space vectors. These reciprocal vectors are orthogonal to the real space vectors.

The first Brillouin zone, defined as the simplest repeating unit in reciprocal space, can often be further reduced to a small wedge; known as the irreducible Brillouin zone. From this the properties of the entire system can be calculated. This helps to reduce the computational power needed to model the system.

2.4 Energy Levels

The previous section describes the positions of the atoms within the lattice. This section will endeavour to describe, firstly the position of the electrons on the atoms, and then how these electrons interact with the electrons on neighbouring atoms.

With the current model of the atom the electrons occupy orbitals surrounding it. The energy of these orbitals are discrete and quantized as these energy levels are the eigenvalues of the Schrödinger equation that describes the atom. Electrons in large atoms occupy different orbitals as the Pauli exclusion principle disallows them from all having the same energy. No two electrons can occupy the same quantum state, two can occupy the same orbital as they can have different spin, therefore any atom with more than two electrons requires multiple orbitals.

The Schrödinger equation that describes single atoms, especially smaller atoms with fewer electrons, is comparatively simpler to solve than large systems, as each additional electron requires more coordinates. For larger systems with multiple atoms this is made more complex by the atomic orbitals being replaced by molecular orbitals. With systems that approximate real solids these energy levels start to form a continuum, called energy bands

2.4.1 Energy Bands

Energy bands need to be discussed in further detail due to their roles in complex multi-atom systems. To explain this phenomenon, we first consider a system where two atoms are brought into close proximity with each other. If the atoms have any unpaired electrons then two new orbitals will form, a lower energy bonding orbital where these now paired electrons will sit, and higher energy, empty, antibonding orbital [9]. This lowers the energy of the system. Energy bands occur when a large number of atoms are brought into this system. These filled bonding orbitals, and the unfilled antibonding orbitals, cannot occupy exactly the same energy as each

other, again due to Pauli's exclusion principle. Therefore, as the number of atoms approaches that which is found in a real solid these massive number of orbitals with very close energies, form a continual band [10]. These bands can contain both bonding and anti-bonding orbitals. The picture becomes more complex with the introduction of larger atomic species, with a greater number of electrons. As a result, this can cause these bands to be unoccupied, occupied, or partially occupied. This leads to macroscopic behaviour and the difference between metals and insulators [11].

The structure of the bands is a good way of identifying a material's conductive properties, i.e. whether it is a conductor, semiconductor or insulator. In the case of sodium, which is both a metal and a conductor, the bonding and anti-bonding orbitals, with increasing atoms, reach a point where they meet in energy space. This creates a single half-filled band. Electrons can be freely and easily promoted, to higher energy levels, within this band. This defines sodium as a conductor. In other materials, a filled band is formed and an energy gap exists between this and any unfilled band. A larger amount of energy is required to promote electrons to a higher energy level, as a result of this gap. Materials with these properties are defined as insulators and semiconductors.

Several models have been put forward to explain the electronic structure of materials to predict their behaviour. The earliest model was the Drude model [12; 13], which was later expanded upon to form the free electron model. The Drude model used the idea of a 'gas' of electrons. These electrons were free to move between the ionic cores, on the basis of several assumptions. These were that the electrons were only allowed to collide with the ionic cores and nothing else. It was only through these collisions that the electrons were able to reach thermal equilibrium. In addition, outside of these collisions, the electrons were influenced by neither the ions or each other. A scattering rate, τ^{-1}, was defined as the probability, per unit time, of one of these collisions. Whilst treating the electrons as a classical

gas was a leap forward in thought at the time, less than 3 years after the discovery of the electron, this model has many flaws. Its most severe failings are the incorrect prediction of electron heat capacity and thermal conductivity, amongst others. This was significantly improved upon by the Sommerfeld, or free electron model. This started to treat the electrons as quantum mechanical particles as opposed to atoms in a classical gas. This correctly predicted the temperature dependence and magnitude of electron heat capacity and was able to approximate the thermal and electrical conductivity of metals. It was able to predict metallic properties in some materials, for example sodium. However, it uses the approximation that the potential $V(\mathbf{r})$ is equal to zero; i.e the electrons do not interact with each other. This is not a particularly good approximation in many materials, with the result that the model fails to correctly categorise them (for example semiconducting silicon and metallic calcium).

2.5   Electrons in the Lattice

Electrons in a solid, even in a metal, are not completely free; they move through the potential created by the array of nuclei that make up the lattice. Applying a crystal potential to the free electron model gives the nearly free electron model. As this potential is formed by these nuclei, which are periodic in the lattice structure, it follows that this potential would have to be periodic as well.

Due to this, boundary conditions are enforced on the wave function to require the periodicity of the wave function to be identical to the periodicity of the potential. The boundary conditions used are called the Born-von-Karman conditions [14]. This implies that the wave function is a planewave that must obey these periodic boundary conditions. By enforcing these conditions, as well as the correct normalization, it is possible to show the solution to this is a particular form of planewave, called a Bloch wave [15]. This is written as

$$\psi_{n\mathbf{k}}(\mathbf{r}) = e^{i\mathbf{k}\cdot\mathbf{r}} u_{n\mathbf{k}}(\mathbf{r}) \tag{2.7}$$

This leads to Bloch's theorem which states that the eigenstates of the Hamiltonian used to describe the atom can be a planewave multiplied by a function with the same periodicity of the lattice, i.e it can be a Bloch wave as long as $u_{n\mathbf{k}}(\mathbf{r}) = u_{n\mathbf{k}}(\mathbf{r} + \mathbf{R})$.

The additional subscript n here is called the band index. For each band n there will be a set of wavefunctions determined by their wavevector, k. These will lie along a dispersion curve, this is the basic concept of a material's band structure.

2.5.1 Band Structure

The periodic potential applied to this model creates band gaps at the Fermi level in some materials. *Ab initio* electron structure calculations are often used to calculate the band structure of materials because the three dimensional nature and complexity of real crystals can make them difficult to study.

2.6 Hund's Rules

Moving on from discussing energies, magnetism and its affect on electrons must now be considered. To begin this, i will first consider the ground state of systems. Hund's rules are useful for this as they are a series of three rules, proposed by F. Hund in 1925 [16; 17], that when followed, estimate the combination of angular momentum quantum numbers that minimise the energy of the system [18]. These rules are given in decreasing importance. The first rule is followed first, followed by second, and then the third, each without breaking a higher rule.

The first rule is to maximise S, the spin angular momentum quantum number. This minimises the Coulomb energy of the system. This is due to the Pauli exclusion principle where two electrons of the same spin cannot occupy the same

orbital [19]. This reduces Coulomb repulsion in the system. The second rule is to maximise L, the orbital angular momentum quantum number, as long as S is still maximised. This also works to reduce Coulomb repulsion. The third rule is to find the value of J, the total angular momentum quantum number. It states that if the shell is more than half full, it is found using $J = |L + S|$. If the shell is less than half full, it is found using $J = |L - S|$. This rule is an attempt to minimise the spin-orbit energy of the system. It is important to note, however, that this rule is only applicable to certain systems where spin-orbit energies are significant enough. For example in rare-earth systems this rule works well however, in transition metal systems this rule is disobeyed as other energies, such as the crystal field, are more important.

An example of the use of these rules, applied to the Gd^{3+} ion can be examined, as this species is found in $GdCo_5$ studied in this thesis. The electronic configuration of Gd^{3+} is $[Xe]4f^7$. Using the first rule, S is maximised. This half fills the shell with all 7 of the electrons in the spin up state. This gives a value of $S = 7 \cdot \frac{1}{2} = \frac{7}{2}$. The second rule is to maximise S. With a half-filled shell this is maximised to 0, as all the spin up electrons cancel out the orbital moment. The final rule is to find J. As the shell is exactly half filled, both equations will calculate the same value for $J = |L + S| = |L - S| = \frac{7}{2}$.

These spin and orbital moments directly lead to different forms of magnetism. These are discussed in detail below.

2.7 Dipole Moments and Long-Range Magnetic Ordering

Magnetism is formed by the existence of spin moments (also called electron dipole moments) as well as their alignment with respect to the lattice and each other.

2.7.1 Types of Magnetism

There are several different types of magnetic ordering or magnetism. These differences are caused by the alignment of the dipole moments with respect to each other and externally applied magnetic fields. In this section I will describe two common arrangements that exist only within an external magnetic field: diamagnetism and paramagnetism. As well as these, I will discuss three common configurations that can align with their own internal fields; caused by the dipole moment within the system and, therefore, can exist without an externally applied field. These are: ferromagnetism, anti-ferromagnetism and ferrimagnetism. This is not an exhaustive list but discusses several of those relevant to this thesis.

Diamagnetism, as stated above, only exists in an externally applied magnetic field and is the weakest form of magnetism under discussion here. In this, the moments within the system align to oppose (or anti-align) the applied field. Paramagnetism, like diamagnetism, requires an external magnetic field. However, the difference is that the moments align with the field rather than oppose it. In both of these the moments are disordered and randomly orientated, having no net magnetism, in the absence of the external field.

However, with other magnetic orderings, the order may remain when the external field is removed, or potentially spontaneously form.

The first example of this type I will discuss is ferromagnetism. Ferromagnetism is where the dipole moments will align with each other, either spontaneously or with an external field. What makes this different to the forms above is that on removal of the external field a net magnetism will remain as these moments will retain alignment and ordering. To remove this net magnetism or change the polarity of the ferromagnet a sufficiently large external magnetic field of the opposite polarity would be required to overcome the remaining order within the magnet. This leads to hysteresis in the magnetism when the magnetic field is flipped.

Anti-ferromagnetism is where the dipole moments within the structure do

not align with each other. This is an ordering system with no net magnetism, as moments on sublattices, which are aligned with each other, oppose or anti-align with the moments on the other sublattices. It is possible for certain external conditions, such as temperature, pressure or external magnetic fields, to change the magnetic ordering of a crystal. For example turning it from an anti-ferromagnet to a ferromagnet. Examples of this are discussed in later chapters when relevant to the samples studied in this thesis.

Ferrimagnetism is the last of these types I will be discussing. In this form of magnetism, the dipole moments behave very much like anti-ferromagnetism with moments on different sublattices opposing each other. However, the difference is the magnitude of the moments on the sublattices are not equal, leading to a net moment that can remain in the absence of an external field, much like ferromagnetism.

There are many other more complex and exotic forms of magnetism and magnetic ordering, some of which will be discussed in later chapters as applicable to the samples used in this thesis.

2.7.2 Long Range Ordering

Some of the forms of magnetism discussed above have long range ordering to spontaneously create or maintain magnetic order within a system. This long-range order is mediated by the exchange interaction [20]. The exchange interaction is mostly dictated by, and dictates, two quantum mechanical ideas. The first of these is the Pauli-exclusion principle. This states that no two electrons cannot occupy the same state in a system. The other idea that is key to the exchange interaction is Hund's Rules. This series of rules, discussed in a previous section, aid us in describing what a system will so, as they help us to describe the lowest energy option.

The system will always align its moments in such a way as to minimise the energy within the system as a whole and, therefore, the energy of the exchange interaction as well. This exchange interaction has an associated exchange energy

for a system. This is expressed as the negative of the sum of the exchange integral, $\mathcal{J}_{ij}$, between every two electrons in the system.

For electrons within the same atom, this exchange integral ($\mathcal{J}_{ij}$), is generally positive, this stabilises a symmetric high spin state following Hund's first rule. With electrons in different atoms, the situation can be very different and different types of exchange need to be considered.

Two forms of exchange will now be discussed: direct exchange and a form of indirect exchange. There are many types of indirect exchange but only the relevant "itinerant" exchange, or the Ruderman-Kittel-Kasuya-Yoshida (RKKY) interaction will be considered at this point.

Direct exchange is when the electrons on neighbouring magnetic ions directly interact via an exchange interaction. This is the simplest form of exchange; however, it is often not an important mechanism in a lot of systems. This is due to this form of exchange mostly occurring between electrons which are very close to each other. This direct exchange generally leads to anti-ferromagnetic ordering, caused by the overlap of the wave functions within real space. As stated above, this phenomenon is often negligible as the electronic orbitals are often significantly smaller than the interatomic spacing; therefore there is not a significant enough overlap of the wave functions for direct exchange. As a result of this, it is often necessary to consider a form of indirect exchange.

The next form of exchange to discuss is a form of indirect exchange. Indirect exchange is responsible for coupling over larger distances, this is where the exchange interaction takes place via an intermediary. One form of this exchange is itinerant exchange or the Ruderman-Kittel-Kasuya-Yoshida (RKKY) interaction [21]. The intermediary used in this form of exchange are conduction electrons. These electrons, which are often found in metals, are very delocalised, allowing for this long-range coupling. At large distances (i.e. large values of r) what the RKKY exchange integral is proportional to is;

$$\mathcal{J}_{RKKY}\left(r\right) \propto \frac{\cos\left(2k_F r\right)}{r^3} \tag{2.8}$$

where k_F is the radius of a spherical Fermi surface. As can be seen, depending on the distance between the magnetic moments, the value of $\mathcal{J}_{RKKY}$ can be either positive or negative, meaning the system can be ferromagnetic or antiferromagnetic.

2.7.3 Spin-Split Bands

The theory discussed above implies that magnetism is solely caused by unpaired electrons and their moments. This would further imply that the strength of magnetism per atom would always have to be in integer multiples of the magnetism of a single unpaired electron. However, this is not the case, as the vast majority of magnetic materials have a non-integer value per atom for their magnetism. To explain and rationalise this discrepancy spin-splitting of the bands is necessary [22]. Certain materials, with strong Coulomb effects and a large density of states at the Fermi level, will find it energetically favourable for unequal occupations of the spin-up and spin-down bands. The change in energy due to spin-down electrons moving to the spin-up band is defined as

$$\Delta E = 1/2 n\left(E_F\right)\left(\delta E\right)^2\left[1 - U_g\left(E_F\right)\right] \tag{2.9}$$

where $n\left(E_F\right)$ is the number of electrons at the Fermi level, and δE is the change in energy as a result of moving electrons from the spin-down band to the spin-up band, and $U_g\left(E_F\right)$ is the Stoner parameter. As can be seen, it is energetically favourable for spin-splitting to occur when the Stoner parameter is greater than one; this is known as the Stoner criterion [23]. For materials where this is true, spontaneous ferromagnetism occurs. In addition, some materials, where the criterion is not satisfied, the susceptibility can be altered. For example, platinum and palladium can be thought of as systems on the verge of ferromagnetism; as the Stoner parameter is

not sufficiently close to 1 to cause spontaneous ferromagnetism. It has a significant effect on the susceptibility, making them easy to magnetise. This is known as Stoner enhancement.

2.7.4 Spin-Orbit Coupling

In addition to discussing how the moments of a system interact to form magnetic phases, it is also necessary to discuss the two moments that combine to form the total magnetic moment of an electron in a system. This is the orbital moment and the spin moment. They each play a role in the magnetism of the system. This is further complicated as, in many systems, they are not independent and there is a coupling interaction between the spin and orbital moments. This can change the energy levels of the electrons in the system and can cause energy bands to split.

This effect can be crucial in theoretically describing some systems and in other systems this can be completely negligible. As a rule of thumb systems which rely on electrons with large orbital moments, such as f electrons, require this phenomenon to be taken into account. In other systems, where the orbital moments are much smaller, for instance ones which rely on d electrons, this phenomenon can be ignored. In this thesis, in all the modelling done, the spin orbital coupling was tested to eradicate doubt over its need [24].

To measure the magnetism, and specifically the magnetic moment, magnetic Compton scattering is used in this thesis. Therefore it is important at this point to discuss the theory of the Compton profiles, as they are both experimentally and computationally obtained in this thesis and therefore it is key to explore what they physically represent and what is actually measured.

2.8   Compton Profiles

Now that we have discussed the various forms of magnetism, and their causes, we can return to discussing how they were measured in this thesis, starting from the cross sections discussed above. In themselves, these are not experimentally observable nor do they produce actual quantities that can be measured. To be able to produce a quantity that can be measured the *Doubly Differential Compton Scattering Cross-Section* (DDCSCS) needs to be introduced [25]. The DDCSCS is the weighted sum of the charge and magnetic Compton cross section. They are weighted by the charge and magnetic Compton profiles respectively ($J(p_z)$ and $J_{mag}(p_z)$)

These Compton profiles are related to the electron momentum density as they are the one-dimensional projections along the z axis in momentum space, p_z. In other words, they are the momentum density twice integrated along p_x and p_y. The difference between these Compton profiles is the charge Compton profile uses the spin independent or charge momentum density ($\rho(\mathbf{p})$), whereas the magnetic Compton profile uses the difference between the spin dependent or magnetic momentum densities ($\rho \uparrow (\mathbf{p})$ and $\rho \downarrow (\mathbf{p})$). This can be represented by the equations:

$$J(p_z) = \iint \rho(\mathbf{p}) dp_x dp_y \tag{2.10}$$

$$J_{mag}(p_z) = \iint \rho \uparrow (\mathbf{p}) - \rho \downarrow (\mathbf{p}) dp_x dp_y \tag{2.11}$$

These Compton profiles are defined so that the integral of the charge profile is equal to the number of electrons per formula unit, and the integral of the magnetic profile is equal to spin moment per formula unit for the system.

Magnetic Compton scattering, as a technique, is an extremely effective method for directly measuring the spin moment of a crystal. This is due to the energies involved, which are high enough to allow the impulse approximation to apply, as

interaction times are short. The result of this is that the measurement is completely independent of the orbital moment. In addition, the x-ray energies used are particularly ineffective at exciting electrons into higher orbitals, meaning that this technique is well suited to observing the ground state of a crystal.

As discussed above, it is possible to separate $J_{mag}(p_z)$ and $J(p_z)$ by using circularly polarised x-rays. As seen in equation 2.4 the magnetic scattering cross section depends on the helicity and the direction of the electronic spin. This means two things; firstly, circularly polarised light is required for this cross section to be non-zero and the magnetic Compton profile to be measurable at all. Secondly, it provides two experimental ways of changing the sign of this cross section, allowing the magnetic term to be isolated by summing two appropriate profiles. These two ways are flipping the helicity of the circular polarization or using an external magnetic field to flip the electronic spin of the sample.

2.8.1   Shape of the Magnetic Compton Profile
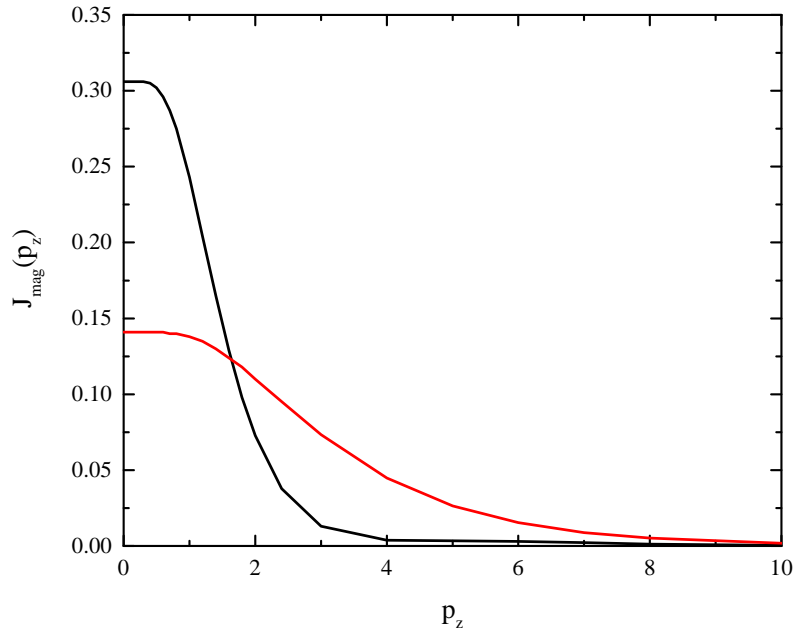
Figure 2.3: Theoretical Hartree-Fock Profile for iridium $5d$ and the neodymium $4f$ electrons (black and red respectively). Both profiles have the same area.

At the beginning of this chapter (section 2.2) the need to incorporate electron momenta, and its subsequent effect on the shape of the magnetic Compton profile, was discussed. The more tightly bound the electron, such as core electrons, the greater the momentum and the broader the profile. Less tightly bound, delocalised electrons have a much narrower profile and a larger contribution at low momentum. The real space and the momentum space wavefunctions, $\phi(\mathbf{r})$ and $\tilde{\phi}(\mathbf{p})$ respectively, are related by a 3D Fourier transform. This effectively means that the broader and more delocalised the real space wave function is in $\mathbf{r}$, the narrower the reciprocal momentum space wave function will be in $\mathbf{p}$. This is illustrated in figure 2.3 as the neodymium $4f$ electrons are more localised than the iridium $5d$, thus having a broader profile. Investigating the broadness of the profile can help identify the electrons that contribute to the profile [28]. This will be used later in the thesis to separate the Compton profiles of contributing electrons in compounds from the total, experimentally obtained profile.

Chapter 3

Computational and Experimental Techniques

In this chapter the experimental aspects of this thesis are discussed. This is investigated in two halves, the first discusses the computational techniques, the ELK and GAMESS codes that are used to provide the theoretical profiles for this thesis. In the second half of the chapter the experimental aspects of measuring the profiles are discussed, including how the experimental profiles are obtained and normalised. Throughout this thesis these theoretical and experimental profiles are compared and used to compliment each other to aid in the understanding of these systems. In addition the experimental set up at SPring8 in Japan is explained and finally the other techniques used in this thesis, to support the magnet Compton scattering technique and to characterise the samples will be covered.

The first code that will be discussed is the ELK code, as well as the Full-Potential Linearised Augmented PlaneWave (FP-LAPW) method that it uses.

3.1   ELK Code

In this thesis the Denisty Functional Theory (DFT) code predominantly used is the ELK code [29]. This is used in Chapter 6 to study $NbFe_2$. This code uses the Full-Potential Linearised Augmented Planewave (FP-LAPW) Method [30] to determine the properties of crystals. Along with the GAMESS code, it is used in this thesis to obtain theoretical Compton profiles from ab initio inputs. These can be then compared to the experimental profiles, aiding in the understanding of the systems.

The FP-LAPW method views each wavefunction as two separate entities. This allows a simplified approximation of these wavefunctions to be made for the interstitial region and the region close to each atom. The approximation to the wavefunction close to the atom would not be valid in the interstitial region and vice versa. Without this method it would not be possible to easily approximate the wavefunction across the entire system.

Near the atomic nuclei, these wavefunctions approximate as nearly spherical in shape and in the interstitial region they are approximated to planewaves. Enough freedom is provided for these approximations to be able to force the value and gradient to be equivalent at the boundary of these regions, requiring the combined wavefunction to be continuous. Once these wavefunctions are described, they can be used by the ELK code to provide properties and parameters of the system; such as band energies and, importantly for this thesis, Compton profiles.

A functional, dependent on the electron denisity, can be proved to exist. This existence thus tells us that an exact analytical solution must exist but the exact nature of this has yet to be determined. Due to this lack of a solution, approximations of this functional are required. The ELK code has many such approximations included in it's package, in this thesis two are used: the Local Spin Density approximation (LSDA) [31] and the Generalised Gradient Approximation (GGA) [32]. The LSDA functional, as the name suggests, is dependent on the electron density (spin

dependent) whereas the GGA functional, as well as taking into account this electron density, also takes into account the gradient of the electron density. Each of these functionals has flaws in its approach. The LSDA, famously, misidentifies the ground state of iron. In this instance, the GGA correctly predicts this but has been known to fail to replicate the ground state of other structures [33]. A benefit of LSDA can be its slightly quicker run time, due to not needing to calculate the gradient of the electron density. It is often useful to try both functionals, if possible, as a sense check for the data produced. In this thesis, the functionals are explicity referenced in the later chapters, when used. There are a few more complex functionals, such as meta-GGA included in the ELK package but these are not used in this thesis.

When running a system through this code, the parameters for describing the system, such as the space group, Wyckoff positions, and the lattice parameters and angles (discussed in Chapter Two), are required. These parameters are fixed for each crystal. Changing these would change the physical properties of the material being investigated. There are other parameters, which are input, which describe the calculation rather than the crystal. These include the following key parameters: the hkmax and the ngridk. The hkmax is the maximum length of the h + k vectors. This affects the maximum value of p_z the Compton profiles are calculated to. The ngridk, with three values, defines the number of k-points sampled in three dimensions. These parameters allow realistic results to be achieved by the code, limiting the effect of the calculation on the results.

It is important that these calculation parameters are converged. This is where, changing the value of a parameter, for example increasing the number of k-points the code is sampling over, no longer has an effect on the output. Ideally a result should converge to every numerical value used in the code that is not related to the system being tested. However, this is not feasible with the time constraints on most applications, so important parameters are chosen. There are a few parameters which, with infinite time, would be converged as well as the hkmax and ngridk

chosen for this thesis. Examples of these include: the size of the initial external field, the rate of decay of the field, the type of mixing the code uses at the end of each loop, as well as others.

Other parameters included in the code, but not requiring convergence due to their nature, are: spinorb, xctype, and fsmtype. Spinorb is a binary command which informs the code if spin orbit coupling is to be included in the calculations. Xctype defines the functional that the code will use. In this instance, GGA and LSDA are the functionals selected for use, as discussed above. Finally, the fsmtype allows for the magnitude or direction of the spin moments, or both, to be fixed for the calculation. This allows particular states to be forced, meaning the profiles, and other parameters, can be compared [34].

The ELK code is a particularly powerful and robust code and is useful for many systems and crystals. However, it struggles with systems with large atomic species and complex crystal structures, with little to no symmetry in their space groups. This is due to the much higher demand for computational power presented by these systems, making calculations unfeasible. In this thesis, GAMESS is used as an alternative code for these systems.

3.2   GAMESS Code

The GAMESS, General Atomic and Molecular Structure System, code [35] uses several variations, selectable in the code, on the Hartree-Fock method [36] to calculate the wavefunctions of the electrons within a system. GAMESS is predominately designed as molecular code rather than one which calculates across the entire crystal, like the ELK code. The way it is used in this thesis, is that a single atom, or small group of atoms, is chosen within the unit cell to calculate their contribution to the system. This atom, or cluster, is sat in the potential generated by a larger, but still comparatively small, subset of the repeating crystal. This is usually a few hundred,

to a few thousand, atoms. In this thesis, this code is used in Chapter 5 to study $Nd_2Ir_2O_7$.

GAMESS assumes that the wavefunctions are a linear combination of atomic orbitals, which are selected by the user. As the number of atomic orbitals used increases the closer to the exact wavefunction the calculation gets. The group of atomic orbitals used in a calculation are referred to as a basis set. To reach the exact wavefunction an infinite basis set would be required. However, a compromise between accuracy and CPU time is needed, because as the number of sets increase the computational work increases by $\approx N^4$, which can quickly become unmanageable. [37]

There are several basis sets that are generally used, starting from the minimal basis set, through the double zeta and the double zeta plus polarisation, and ending with the triple zeta plus polarisation. The minimal basis set includes one atomic orbital for each occupied orbital in the atom. The double zeta and the double zeta plus polarisation both include two atomic orbitals, per occupied orbital, but the double zeta plus polarisation includes the lowest unoccupied orbital as well. Finally the triple zeta plus polarisation includes three atomic orbitals per occupied orbital as well as the first unoccupied orbital. This final basis set, the triple zeta plus polarisation, is the basis set used for calculations in this thesis.

Like in ELK, convergence is important here. In addition to similar parameters, discussed above, the size of the larger structure the cluster sits in should be tested and ideally should reach convergence. This structure should also be as close to symmetrical, about the cluster, as possible. This avoids false and uneven results from unsymmetrical potentials.

The limitations of the GAMESS code can be seen in the way it deals with metals. The small, non-repeating, structures used by the GAMESS code makes it struggle with many materials; such as metals. The dependence on the potentials and the itinerant electrons are not well dealt with. The strength of the code lies

in its ability to focus in on the individual atoms within the larger structures. This allows modelling of large atoms, such as iridium, that ELK struggles with due their size within the repeating structure. For the same reason, GAMESS also has an advantage with unit cells with low symmetry as ELK would have to model the entire cell and GAMESS can choose to focus on key parts.

It is important to note that DFT codes, such as ELK and GAMESS, require the calculation of several parameters which all depend on each other. To calculate these, there is no one parameter you can start with which will lead to the others. Therefore, to perform these calculations an iterative process is required. This process is called the Self Consistent Field (SCF) method [38]. In this method, the key parameters, such as electron density, total energy, and internal potentials, are calculated from an initial guess in iterative loops until these parameters converge and stop changing, as the loop cycles.

The next topics which need to be discussed are the experimental techniques and the setup used in this thesis. To start with, a grounding in the history of magnetic Compton scattering and how it developed as a technique is needed.

3.3 History of Magnetic Compton Scattering

The history of Magnetic Compton Scattering begins with the experiments of Laue and Braggs, which won them Nobel prizes in 1914 and 1915. These experiments are generally considered the start of the the study of the structure of solids at an atomic level. It was around this time that Karl Compton, along with others, were noticing the effect of magnetic fields on scattering experiments [39], although this effect was not understood at the time. Karl Compton, was the elder brother of Arthur Compton who the effect and technique was named after. At this time Arthur Compton was trying to reconcile the inelastic scattering, later named Compton scattering, with classical electromagnetism.

In 1929, another step forward was taken as Klein and Nishina purposed a scattering cross section [3] that correctly described the asymmetry of the scattering with regards to direction. It was about this time that diffraction experiments were providing strong evidence for the wave-like behaviour of light and scattering experiments were simultaneously providing compelling evidence of the particle-like behaviour. This debate within physics as a whole is also seen reflected in the growth of Compton scattering, whilst Compton strongly believed in that light was a wave and tried to reconcile this with the inelastic scattering, he suggested a quantised solution [2] of his results [40], which won him the Nobel prize in 1927.

The theory and technique of Compton scattering progressed over the next 50 years culminating in 1976 where Sakai and Ono performed the first magnetic Compton experiment [41]. This experiment measured the magnetic Compton profile of iron using circularly polarised γ rays. The experiment used a ^{57}Co source, creating γ rays at 122KeV via the beta decay of this isotope. This had a couple of issues, predominately the need to keep the source at 50mK to get a net amount of circularly polarised γ rays, this limited the strength of the source as self heating from the beta decay would raise the temperature above this if the activity was too high. Despite these limitations this experiment confirmed the validity of this technique for studying solids.

The main problem with this technique at this time was finding a way of providing circularly polarised photons at high energy and high flux. At the advent of synchrotrons the access to high energy, high flux photons was addressed but initially they were not sources of circularly polarised photons, as the bending magnets produced mostly linearly polarised light and the symmetric undulators produced equal amounts of both helicities of circularly polarised light. At low energies, half wave plates or other optics can be used to effect the polarity of incident light but this is not possible at higher energies. Only the use of a helical undulator or an asymmetric wiggler (as is used on the beamline used in this thesis) can produce a

sufficiently high flux of high energy circularly polarised x-rays to be used for this technique. However initally these sources were rare.

The first attempt at a magnetic Compton experiment at a synchrotron was performed by Holt *et al* in 1986 [42], like Sakai and Ono [41] 10 years earlier, this was performed on ferromagnetic iron but provided worse statistical accuracy than the earlier γ ray experiments. This was followed two years later by the first interpretable magnetic Compton experiment [43], this confirmed the use of synchrotrons and marked the entry into the modern era of magnetic Compton scattering.

From here the key experimental aspects of magnetic Compton scattering and the setup used in this thesis can be discussed.

3.4   Experimental Magnetic Compton Scattering

It is important to correctly calibrate the obtained magnetic Compton scattering data. After first normalising the data to the monitor's count rate to remove any effects caused by any changes in the intensity of the beam, the spectra are calibrated using well known energies of known absorption edges. Several different known energies are usually used; lead is particularly common as it is found in many of the spectra since there is lead in numerous places in and around the experimental set-up. Figure 3.1 shows an example of nickel data against channel number, with the Compton peak being visible along with lead fluorescence peaks for calibration [44]. As can be seen, the peaks are all slightly misaligned with each detector. Calibrating the spectra to an energy scale for each detector separately fixes this issue.

A second, more complex, example of a group of these spectra is shown in figure 3.2, i.e. a profile for $Nd_2Ir_2O_7$ with both lead and iridium florescence lines used for normalisation, The lead kβ and the iridium kα are used but, because of their similarity in energy, the iridium kβ and the lead kα overlap and are therefore not used.
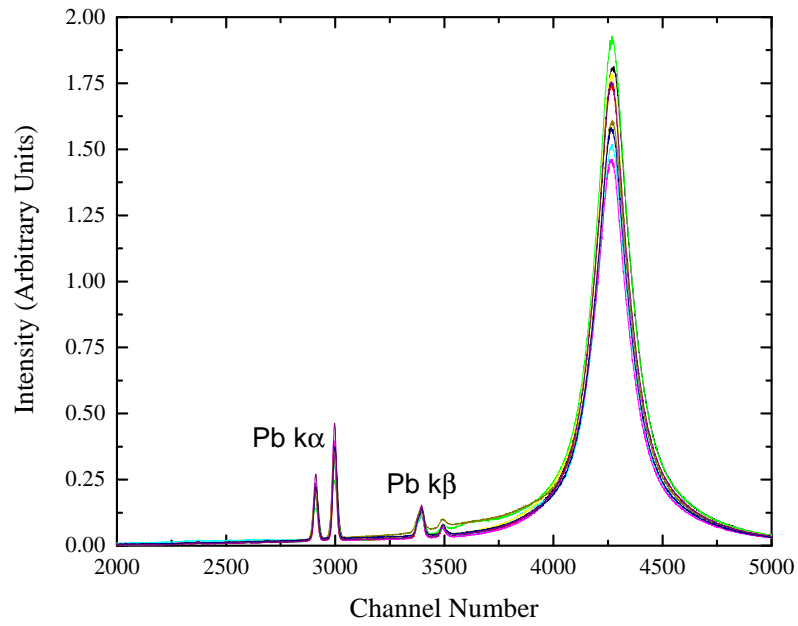
Figure 3.1: Unprocessed nickel data collected at 300K and 1T, showing all 9 working detectors. The difference in the positions of the Compton peaks is as a result of the different calibrations of the detectors and is fixed by the calibration using the well-defined lead fluorescence peaks
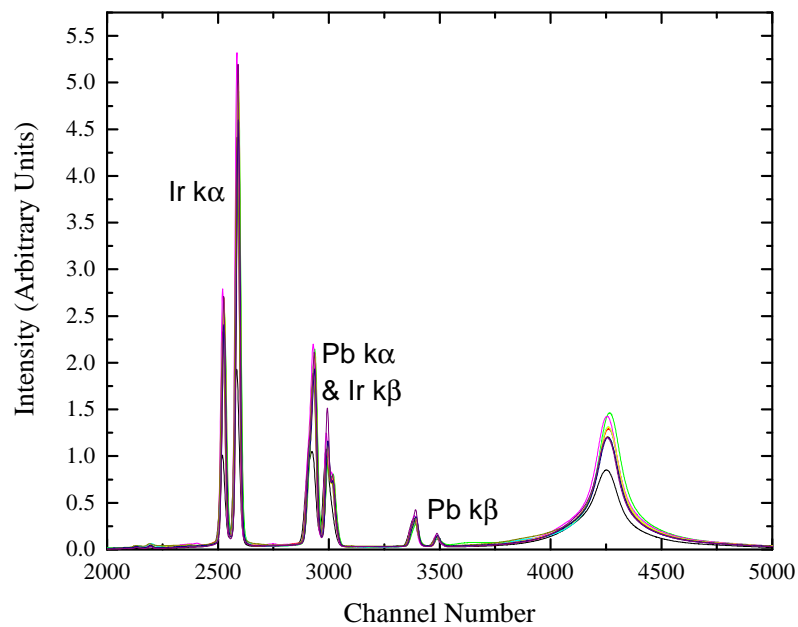
Figure 3.2: Unprocessed $Nd_2Ir_2O_7$ data collected at 10K and 5T, showing all 9 working detectors, as well as the fluorescence peaks for lead and iridium

This energy scale is converted to a momentum scale. In order to do so, a relationship between the scattered photon's energy and the momentum of the electron involved in the scattering event is required [45]; this relationship is given by

$$p_z = \frac{1}{\alpha mc^2} \left(\frac{|\mathbf{k}_1 - \mathbf{k}_2|}{2} + \frac{E' - E}{2} \sqrt{1 + \frac{2mc^2}{E'E(1 - cos\phi)}} \right) \qquad (3.1)$$

where

$$|\mathbf{k}_1 - \mathbf{k}_2| = \sqrt{E'^2 + E^2 - 2E'Ecos\phi} \qquad (3.2)$$

These equations allow an ability to convert from the energy scale to a momentum scale using the scattering angle, ϕ, and the energy of the scattered photon, E'. The Compton profile is a one-dimensional projection of the momentum density along the scattering vector and, therefore, the momentum scale used is along that direction as well. The $(\alpha mc^2)^{-1}$ term in equation 3.1 is necessary to convert the p_z scale to atomic units (a.u.) and is equal to 0.26817. As the equations suggest $p_z = 0$ is at the peak of the Compton profile.

As determined previously, the MCP is the difference between the spin up and spin down Compton profile and this difference is symmetrical about $p_z = 0$. It is possible to take advantage of this fact to improve the statistics of the data by *folding* the data around $p_z = 0$. To further increase the statistics the data is *binned*, decreasing the number of points but reducing the error on each point.

The errors on a Compton profile are calculated by propagating Poisson counting statistics. This error is propagated with all the post-processing performed on the data.

The integral of a magnetic Compton profile, obtained experimentally, is proportional to the spin moment of the sample. This data needs to be normalised to calculate the spin moment from experimental data. To normalise the data a flipping

ratio is used with the flipping ratio, FR, defined as

$$FR = \frac{I\uparrow - I\downarrow}{I\uparrow + I\downarrow} \qquad (3.3)$$

where $I\uparrow$ and $I\downarrow$ are the intensity of the Compton profiles measured in the two field directions and are referred to as the spin up and spin down Compton profiles, respectively. The error on this is calculated based on the error on $I\uparrow$ and $I\downarrow$ being $\sqrt{I\uparrow}$ and $\sqrt{I\downarrow}$ respectively. This means the error on FR can be written as,

$$\sigma_{FR} = FR\sqrt{(I\uparrow + I\downarrow)^{-1} + \frac{(I\uparrow + I\downarrow)}{(I\uparrow - I\downarrow)^2}} \qquad (3.4)$$

This flipping ratio can be used to calculate the spin moment by comparing it to a calibration sample [46], (in this thesis nickel is used). The spin moment of the sample, μ_s, can be calculated using the equation;

$$\mu_s = \frac{FR_s}{FR_{Ni}} \times \frac{Z_s}{Z_{Ni}} \times \mu_{Ni} \qquad (3.5)$$

where Z_s and Z_{Ni} are the atomic number for the sample and nickel respectively and μ_{Ni} is the spin moment of nickel, which equals $0.56\mu_B$ [47]. As above the error was propagated through, using equation 3.4 to find the error on FR_s and FR_{Ni} and then using this to calculate the error on μ_s.

The experimental orbital moment can be calculated as a difference between the total moment, obtained from the characterisation techniques discussed below and this spin moment.

More information than just these bulk moments can be obtained from these experimentally obtained profiles, for instance, information about the magnetic moments on different species within the crystal can be obtained from the shape. In this thesis, theoretically calculated profiles are mathematically fitted to the tails of the experimental data (above a particular value p_z), using a least squares fit using

a script written for this thesis in Matlab, the errors are propagated through using this code as well. This can be done on crystals, where the magnetism is due to spin on electrons with different constraints in real space (i.e localised or delocalised electrons). As discussed above, constrained, localised, electrons have a much broader profile in momentum space which allows them to be separated.

3.5 SPring8

In this thesis, much of the experimental data was collected on the BL08W beamline at SPring-8 synchrotron in the Hyōgo prefecture, Japan.

3.5.1 Synchrotron Radiation

Synchrotrons can produce radiation in a broad range, for example SPRing-8 can produce a range from soft x-rays at 300eV to hard x-rays of 300KeV. As previously seen, high energy photons are required for high quality Compton scattering.

Synchrotrons are important for Compton scattering as they are the only practical way to get sufficiently high energy x-rays with sufficiently high flux. At these energies x-rays are also non-destructive, making Compton scattering experiments also non-destructive, a point which is useful with important or hard to grow samples from which many measurements are needed.

Synchrotron radiation is created by accelerating charged particles. Simply, when charged particles, such as electrons, are accelerated along curved trajectories they emit radiation known as synchrotron radiation. [48]

In synchrotrons, bending magnets are used to steer the beam of electrons, creating this radiation. To increase the flux of radiation these facilities can produce over just the bending magnets, other insertion devices are used as well such as wigglers. These periodic field devices have periodic magnetic fields which accelerate the electron beam and therefore produce this radiation. This is further improved by

the helical wiggler which, as the name suggests, have helical magnetic fields, which allows for shorter magnetic periods, further increasing the brightness. [49]

These wigglers can emit light that is linearly polarised but many experiments, such as Compton scattering, require circularly polarised light. For the experiments within this thesis an asymmetric helical wiggler is used to provide the required circularly polarised light. The principle of these devices is that the magnetic field that accelerates the beam is not symmetric. Generally strong positive poles are surrounded by two weaker negative poles, these combinations are then surrounded by air gaps. Over the period the positive and negative fields are equal but not symmetric. This asymmetric field provides the required circularly polarised photons. [50]

3.5.2   The Experimental Set Up

The experimental magnetic Compton profiles were measured on beamline BL08W at SPring8 in Japan. The energy spectrum of the scattered flux was measured using a 10-element Ge detector at a mean scattering angle of $173°$. The incident energy of 175keV and scattering angle of $173°$ resulted in a resolution of 0.44 a.u. of momentum (where 1 a.u.$=1.99 \times 10^{-24}\, \mathrm{kg\, m\, s^{-1}}$).

When x-rays are absorbed, electron-hole pairs are created, creating a charge pulse. The charge pulse is converted to a voltage pulse, which is converted to a digital signal by an analog-to-digital converter (ADC) and analysed by a multi-channel analyser with 8190 channels. The pulse's voltage is proportional to the energy and is converted to an energy scale, using known energy values as discussed above.

During the time that the detector and the analyser are processing a count they are unable to process another. The time when a second count cannot be received is called dead-time. The experimentalist needs to balance the experimental process in order to minimise dead-time whilst keeping the count-rate as high as

possible. This is achieved by varying the size of the beam profile that can hit the sample by controlling the width of the beam slits from the optics hutch. An approximate maximum count-rate of $15000cps$ and a maximum dead time of approximately 4% was used. For this reason, materials with the correct absorption profiles were placed in front of the detector to filter out particular fluorescence peaks and increase the proportion of counts in the Compton peak. For example using 1mm of tin in front of the detector when measuring $Nd_2Ir_2O_7$ will absorb $\approx 100\%$ of neodymium fluorescence, 86% of iridium fluorescence, 74% of lead fluorescence, and 58% of the photons at the Compton peak energy. These values can be tuned with the thickness of the tin and mean that a greater proportion of the count is from the Compton peak. This can be seen in figure 3.3 that shows the percentage absorption against energy for two different thicknesses of tin.
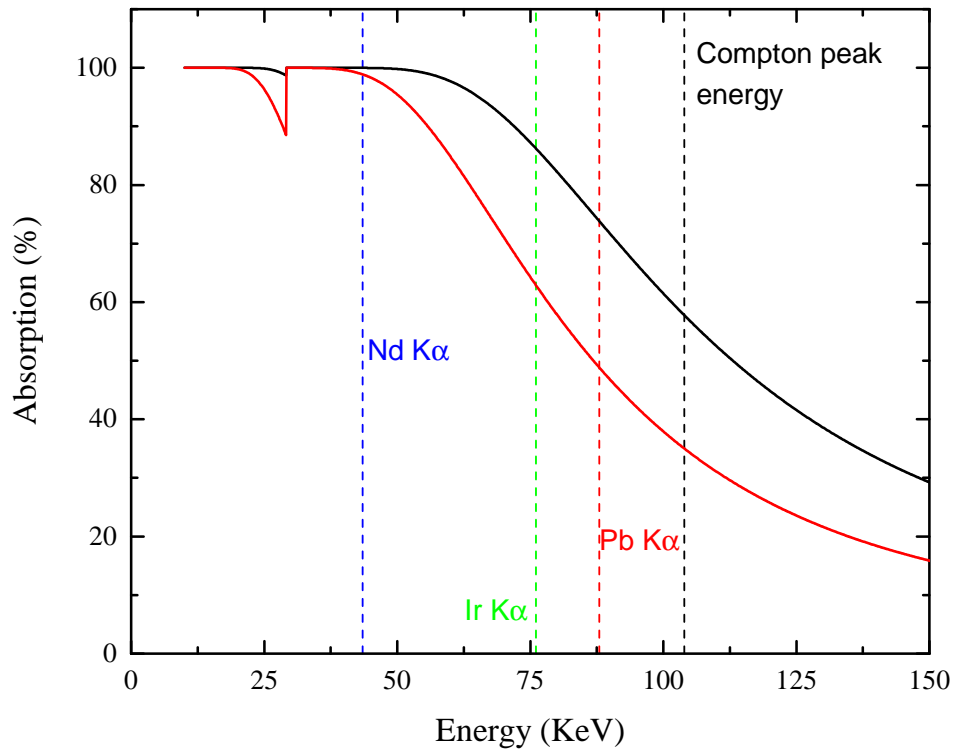
Figure 3.3: Percentage absorption against energy for 1mm (black) and 0.5mm (red) of tin. Dotted lines show the energies of neodynium, irridium and lead fluorescence as well as the energy of the compton peak.

3.6   Characterisation Techniques

To obtain more information, other techniques were used in this thesis alongside magnetic Compton scattering including SQuID and VSM magnetometry and Laue diffraction. These techniques were used to characterise the sample, either to obtain the total magnetic moment or to align a single crystal along a crystallographic direction.

3.6.1   Magnetometry

In this thesis SQuID and VSM magnetometry were used to obtain the total moment of the samples. Using this information, the orbital moment could also be calculated. With most of the samples a SQuID was used as the calibration is more stable and therefore a more exact result can be obtained. The VSM was used when the sample had too large a moment or was too large to fit in the physical confines of the SQuID due to its smaller opening.

SQuID Magnetometry

Superconducting **Qu**antum **I**nterference **D**evices (SQuID) are used to measure the total moment of a sample [51]. The sample is moved through a set of superconducting coils within a magnet, thus inducing a current in the coils. Any change in current is proportional to the magnetic flux.

It is possible to keep the temperature at a fixed point and change the field, making MvsH measurements, or to fix the field and sweep the temperature, making MvsT measurements

VSM

A **V**ibrating **S**ample **M**agnetometer (VSM), vibrates a sample sinusoidally, perpendicular to an applied uniform magnetic field. This oscillates the magnetic field of the

sample inducing a voltage in the detection coils [52]. This voltage is proportional to the samples total moment and therefore, it is possible to make MvsH and MvsT measurements, as with the SQuID discussed above; However, the VSM used in this thesis was set up in such a way as to optimise the taking of MvsH measurements although this made MvsT measurements slow and helium-expensive.

3.6.2   Laue Diffraction

The final characterisation technique used in this thesis was Laue diffraction. This technique was used to identify and align the single crystals measured to the crystallographic direction, or often multiple directions, along the directions chosen for the MCS experiments.

Using the Laue technique, x-rays were scattered off the sample and into a camera, with the camera situated between the incoming beam and the sample itself. The image obtained showed the crystallographic direction facing the incoming x-ray beam and the camera. The sample was then placed on a goniometer which was then adjusted, rotating the sample through three axes into the desired direction before mounting onto the plate used for the MCS experiments. This is referred to as the back-reflection Laue method.

The spots on a Laue diffraction pattern are crystallographic directions and the pattern reflects the symmetry of the sample and of that direction. Bragg's law relates the planar index n, the wavelength of the x-rays λ, the distance between the planes d and the scattering angle θ by;

$$n\lambda = 2dsin\left(\theta\right). \tag{3.6}$$

For constructive interference, the scattering angle is 2θ.

The spots on these patterns are characteristic of the symmetry of the crystals and are used to aid the alignment of the samples. Figure 3.4 shows the Laue pattern
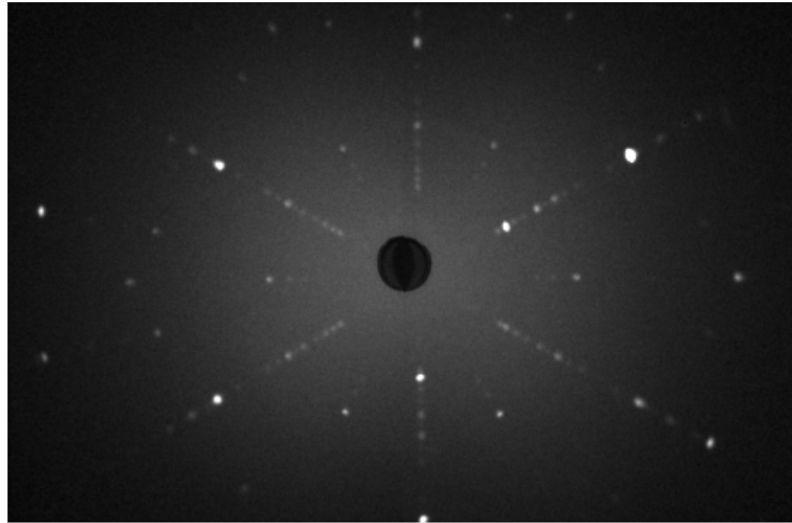
Figure 3.4: Laue diffraction pattern of $NbFe_2$ along the c direction

of $NbFe_2$, the sample has been orientated so a high symmetry direction is facing the camera, in this case the c axis, as can be seen by the spots converging at the centre of the image.

Chapter 4

Temperature Dependence of the Spin Moments in GdCo$_{5-x}$Ni$_x$

4.1   Introduction

GdCo$_5$ is a member of the RETM$_5$ class of materials (where RE is rare earth and TM is transition metal). These materials have a wide range of magnetic properties due to the different number of $4f$ electrons from the rare earth element [53]. Since useful magnetic properties, such as a high T_c, were found in the permanent magnet SmCo$_5$ over fifty years ago [54], there has been a lot of interest in studying this series.

The complexity of this series can be split into three levels by the RE element in the material. The simplest level uses yttrium which is a non-magnetic rare earth metal with no $4f$ electrons. The second level is gadolinium, which has a half filled $4f$ shell, thus removing crystal field interactions and spin-orbit coupling effects. The third and final level consists of the remainder of the rare earth series with partially filled $4f$ shells [55]. In this chapter gadolinium, as the RE element, is considered. In GdCo$_5$, the symmetry of the $4f$ shell removes crystal field interactions. This is particularly useful as it makes it easier to theoretically and experimentally study

the interactions between the rare earth element and the transition metal [56].

Doping a RETM$_5$ system with either a second rare earth element, e.g. Gd$_x$Y$_{1-x}$Ni$_5$ [57], or a second transition metal, such as GdCo$_{5-x}$Cu$_x$ [58], YCo$_{5-x}$Ni$_x$ [59], and GdCo$_{5-x}$Ni$_x$, which is investigated in this chapter, can change the magnetic properties in a systematic manner [56].

There have been previous investigations on the series of samples studied in this chapter. There are some studies which have been completed, examining the properties of RETM$_5$ samples, that are often at tangents to the Ni doped GdCo$_5$ series studied in this chapter but where relevant, these have been discussed throughout. A small number of previous studies have direct correlation to our sample group and are discussed below. The previous work done on these samples is comprehensive for the broad study of the sample series but follows a different line of investigation to our studies, as they deal in the total moment. Because of the relative infancy of this subject area, many of the papers and studies available are continuations of each other: tightening in on various different properties, different sample series, or replicas of each other whilst examining different samples or series.

Chuang *et. al.* [60] investigated GdCo$_{5-x}$Ni$_x$ for values of x between 0 and 5, observing a decreasing T_c with increasing nickel content. Compensation temperatures were also investigated, although the paper focused on temperatures above 300K meaning that compensation temperatures less than 300K would not have been found.

Liu *et. al.* also investigated this series at the low nickel end of the series ($x \leq 1.05$) [61] to find the coupling constant between the transition metal and rare earth sublattices. Compensation temperatures have also been measured in GdCo$_{4-x}$Ni$_x$Al [62] and this was shown to increase as the nickel content increases.

More recently, within the physics department at Warwick University, samples of RECo$_{5-x}$TM$_x$, where RE = Gd and Y, TM = Ni and Fe, and $x \leq 1$, were prepared and experimentally determined properties were compared to DFT calcu-

lations [55]. A decrease in magnetism and Curie temperature was observed, both experimentally and theoretically, with increasing nickel content. This led the way to further work, within the group, into the doping of $GdCo_{5-x}Ni_x$ by A. Tedstone *et. al.* [56]. Compensation temperatures were found for samples within $1 < x < 3$ range; for larger x no compensation temperature was observed below 360K and these temperatures were found to increase with increasing nickel content. While this paper provides broad investigations into the samples, measuring the total moment and compensation temperatures, and excels in its use of computational methods, it does not delve into the contributions to the total moment. This paper emphasises the complimentary nature of theory and experimental investigations and this chapter primarily aims to support the experimental aims of the group.

In this chapter investigations of four different compositions of polycrystalline $GdCo_{5-x}Ni_x$ were carried out: $x = 1$, $x = 1.28$, $x = 2$, and $x = 3$, building on the work performed by A. Tedstone *et.al.*. It not only allows a way to separate the spin and orbital moments from the total moment experimentally, but it also provides a way of isolating the moments on the sublattices rather than just the bulk total moment.

This is something that the previously mentioned studies neglected to incorporate in their investigations. In doing this, we can expand on the previous knowledge and better understand the contributions at the compensation temperature. The Compton scattering technique directly measures the spin moment, with no assumptions required, making it a powerful technique for separating out the bulk spin and orbital moments of these samples. Due to the nature of the Compton profiles it is possible, in this case, to separate out the contributions from the sub lattices. Whilst this has more limitations, this still adds to the understanding of these samples. This technique had yet to be applied and the discussions surrounding these properties were lacking in depth and detail on this point. It is hoped that the work in this chapter goes towards aiding further understanding and discussion.

4.1.1 Crystal Structure

RETM$_5$ materials crystallise into a hexagonal lattice with the space group $P6/mmm$ figure 4.1. The RE element is on the $1a$ site and the TM is on the $2c$ and $3g$ sites. As is seen, alternating layers form, comprising of TM in the $3g$ position and central RE atoms, surrounded by the TM on the $2c$ sites. This general picture holds true for GdCo$_5$ and for GdCo$_{5-x}$Ni$_x$ studied in this chapter.
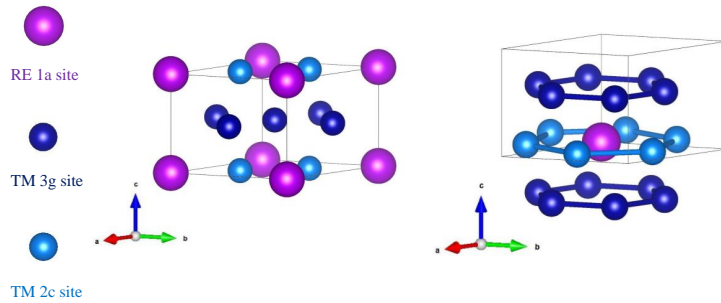
Figure 4.1: Hexagonal structure of RETM$_5$, space group $P6/mmm$ (191) with the RE element on the $1a$ site (purple), and the TM on the $2c$ site (light blue) and the $3g$ site (dark blue). Showing both a unit cell and the alternate layers of TM$_{3g}$ and RE atom surrounded by TM$_{2c}$. (Box in both images represents the unit cell boundary)

The relatively simple structure shown here, coupled with the complex and diverse behaviour of different $4f$ electrons [63] makes this series ideal for investigating different TM-TM, TM-RE interactions as well as interactions with the crystal field. However, as mentioned above, in the particular case of gadolinium as the rare earth element, as is the case for this chapter, the symmetry of the $4f$ shell removes crystal field interactions.

When GdCo$_5$ is doped with nickel there has been previous work on whether this favours the $2c$ or $3g$ sites. Neutron diffraction experiments on YCo$_5$ which was nickel doped [64] found a preference for the $2c$ sites, this was backed up by computational work [55] on Ni-doped GdCo$_5$.

4.2 Electronic Structure and Magnetism

GdCo$_5$, the material on which the samples studied in this chapter are based, is ferrimagnetic [53]. The total moment and the applied field is aligned with the cobalt $3d$ moment and antiparallel with the gadolinium $4f$ moment [65]. However, at the other end of this series with GdNi$_5$, whilst also ferrimagnetic, the total moment is antialigned with the cobalt $3d$ moment and parallel with the gadolinium $4f$ moment [66]. GdNi$_5$ also has a much lower curie temperature of 32K [57]. In this compound, nickel has a much smaller moment than cobalt or gadolinium [67], which implies that as the series progresses from GdCo$_5$ to GdNi$_5$ the magnetisation of the TM sublattice is expected to decrease.

At low temperatures the moment on the gadolinium lattice is smaller than the moment from the cobalt lattice in GdCo$_5$ [55]. However, after a finite amount of doping the moment on the cobalt-nickel sublattice is reduced to below that of the gadolinium moment ($x \approx 1$) [56]. The gadolinium moment has a much greater temperature dependence than the cobalt-nickel lattice which implies that, for values where $x > 1$, there is a temperature that these lattices compensate for each other and cancel out, this is called the compensation temperature. Below this temperature the gadolinium moment aligns with the field and above this temperature the $3d$ lattice aligns. This creates an interesting temperature dependence which is discussed below.

In undoped GdCo$_5$, as the temperature increases the magnetism increases to a maximum at ≈ 800K [68]. Further increasing temperature decreases the magnetism to the Curie temperature of 1014K [69]. This slightly unusual temperature dependence is due to the fact that the gadolinium moments are a lot more temperature dependent and disorder much more rapidly than the cobalt moments that are anti-aligned with them [55].

It was found that in these series (at zero temperature) the gadolinium, cobalt, and nickel moment are 7, 1.6, and 0.6 respectively [56]. This implies that in GdCo$_5$,

and GdCo$_{5-x}$Ni$_x$ with a sufficiently low value of x ($x \lesssim 1$), at low to zero temperatures the moment of the ferromagnetically aligned cobalt-nickel, $3d$, is greater than the gadolinium. Therefore, in these materials the cobalt-nickel aligns with the external field and the gadolinium moment opposes it. In these materials, as discussed above, the gadolinium is more dependent on the temperature this explains the temperature dependence of the magnetisation that is observed [68; 70].

With GdCo$_{5-x}$Ni$_x$ ($x \gtrsim 1$) to GdNi$_5$, at significantly low temperatures the gadolinium moment is larger than the cobalt-nickel moment and therefore will align with the field (with the $3d$ moment anti-aligned). In a subset of these materials, (depending on the T_c of the material) as the temperature increases the magnetisation decreases because the gadolinium moment decreases with temperature, whereas, in comparison, the $3d$ moment is more constant with temperature. A point is reached at a finite temperature where the cobalt-nickel sublattice has a greater moment than the gadolinium atoms. At this transition temperature the signs of the moments for the gadolinium and cobalt-nickel swap. After this the temperature dependence is similar to that of GdCo$_5$, increasing until the Curie temperature is reached. This can only be observed in materials where their T_c is higher than where the transition temperature is or would be (i.e. this effect is not seen in GdNi$_5$ as the curie temperature is 32K).

Using a **V**ibrating **S**ample **M**agnetometer (VSM), the total magnetic moment for the samples used in this chapter was obtained, seen in figure 4.2. The temperatures used are discussed below. A VSM was used as the physical size of the samples was too large for the sample are of the **S**uperconducting **Qu**antum **I**nterference **D**evices (SQuID) that was available.

The results, as seen in figure 4.2, show the discussed pattern for GdCo$_{3.72}$Ni$_{1.28}$, in black and GdCo$_3$Ni$_2$ in red (GdCo$_2$Ni$_3$ in green, has a transition temperature outside the experimental range). A clear minimum can be seen for these two samples where the total moment of the $3d$ and $4f$ sublattice compensate.
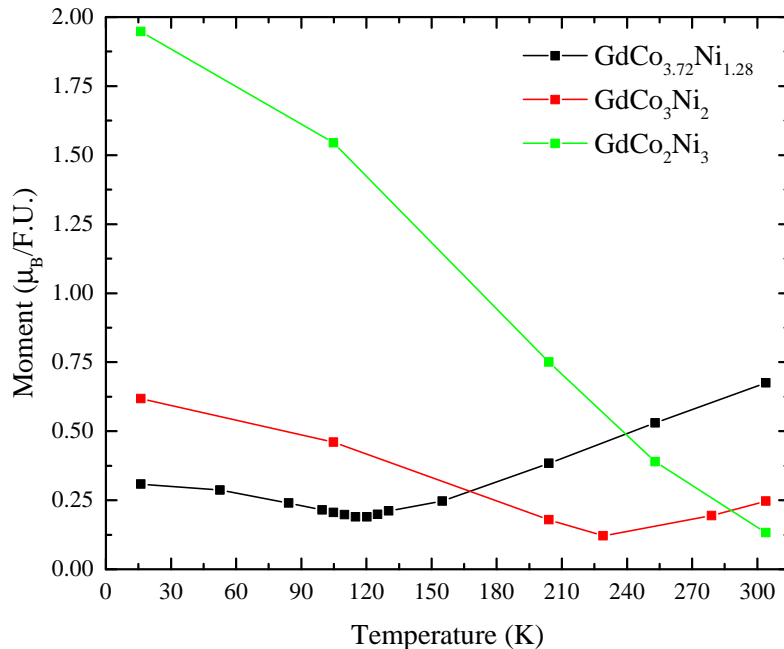
Figure 4.2: VSM data for the total moment against temperature for $GdCo_{3.72}Ni_{1.28}$ (black), $GdCo_3Ni_2$ (red), and $GdCo_2Ni_3$ (green)

4.3   Results

Four samples were investigated in this chapter, with increasing amounts of cobalt replaced with nickel. These samples were $GdCo_4Ni$, $GdCo_{3.72}Ni_{1.28}$, $GdCo_3Ni_2$, and $GdCo_2Ni_3$ ($x = 1$, $x = 1.28$, $x = 2$, and $x = 3$). On all four samples, the Compton scattering measurements were performed at $2T$ with the temperatures that the measurements were taken at shown in table 4.1. The temperature controller used for these experiments would settle at a stable temperature slightly higher than the setpoint. These higher recorded temperatures were also used to obtain the total moments in the VSM (as opposed to the setpoint temperature).

For each of the samples, and temperatures: the total moment was collected using a VSM, the spin moment was collected using the magnetic Compton scattering result, and from these an orbital moment was also calculated by subtracting the spin moment from the total moment. In addition to this, using the fact that the $3d$ moment from the cobalt/nickel is a lot more itinerant and therefore narrower

50

Sample	Set-point	Actual Recorded Temperature
$GdCo_4Ni$	300K	304K
$GdCo_{3.72}Ni_{1.28}$	15K	16.1K
$GdCo_{3.72}Ni_{1.28}$	50K	52.6K
$GdCo_{3.72}Ni_{1.28}$	80K	84.3K
$GdCo_{3.72}Ni_{1.28}$	95K	99.6K
$GdCo_{3.72}Ni_{1.28}$	100K	104.9K
$GdCo_{3.72}Ni_{1.28}$	105K	110K
$GdCo_{3.72}Ni_{1.28}$	110K	115K
$GdCo_{3.72}Ni_{1.28}$	115K	120.2K
$GdCo_{3.72}Ni_{1.28}$	120K	125.2K
$GdCo_{3.72}Ni_{1.28}$	125K	130.2K
$GdCo_{3.72}Ni_{1.28}$	150K	155K
$GdCo_{3.72}Ni_{1.28}$	200K	204K
$GdCo_{3.72}Ni_{1.28}$	250K	253K
$GdCo_{3.72}Ni_{1.28}$	300K	304K
$GdCo_3Ni_2$	15K	16.1K
$GdCo_3Ni_2$	100K	104.9K
$GdCo_3Ni_2$	200K	204K
$GdCo_3Ni_2$	225K	229K
$GdCo_3Ni_2$	275K	279K
$GdCo_3Ni_2$	300K	304K
$GdCo_2Ni_3$	15K	16.1K
$GdCo_2Ni_3$	300K	304K

Table 4.1: List of temperature the magnetic Compton scattering experiments were performed at for all four samples investigated. The setpoint the temperature controller was set to and the temperature recorded by the sample.

Total Moment	Spin Moment	Orbital Moment	$3d$ Spin	$4f$ Spin
1.052	0.41 ± 0.02	0.64 ± 0.02	1.7 ± 0.2	-1.2 ± 0.1

Table 4.2: Total, spin and orbital moments, in $\mu_B/F.U.$ for GdCo$_4$Ni at $2T$ and $300K$. Including the calculated contributions to the spin moment from the narrow $3d$ and broader $4f$ orbitals.

in momentum space than the much more localised Gadolinium $4f$ moment, it is possible to separate out the contributions to the spin moment from these orbitals, as is discussed in chapter 2.

The results from the VSM and Compton scattering experiments will be discussed separately for each material in the sections that follow and then referred to collectively in the discussion section later in the chapter.

4.3.1 GdCo$_4$Ni

Although GdCo$_4$Ni was one of the samples investigated in this chapter, taking into account the fact that a change in sign of the spin moment would happen at a temperature that could not be attained with the set-up used, if one existed at all, and bearing in mind time constraints, only one temperature, 300 K, was measured with this sample. Table 4.2 shows the moments obtained experimentally as well as the $3d$ and $4f$ contributions.

As can be seen, the $3d$ moment is parallel to the applied field and the $4f$ moment is antiparallel. This fits with the theory for the series. The one value that was taken, is not enough to tell if there is a transition temperature, or if the $3d$ spin moment remains positive at zero temperature. However A. Tedstone *et al.* [56] did not observe a compensation temperature down to 10K.

The Compton profile obtained for this sample is shown in figure 4.3.

Figure 4.3 demonstrates the method used in this chapter to separate out the contributions to the total spin moment from the sublattices. The figure shows the Compton profile of GdCo$_4$Ni at 2T and 300K. A gadolinium profile is fit to the data
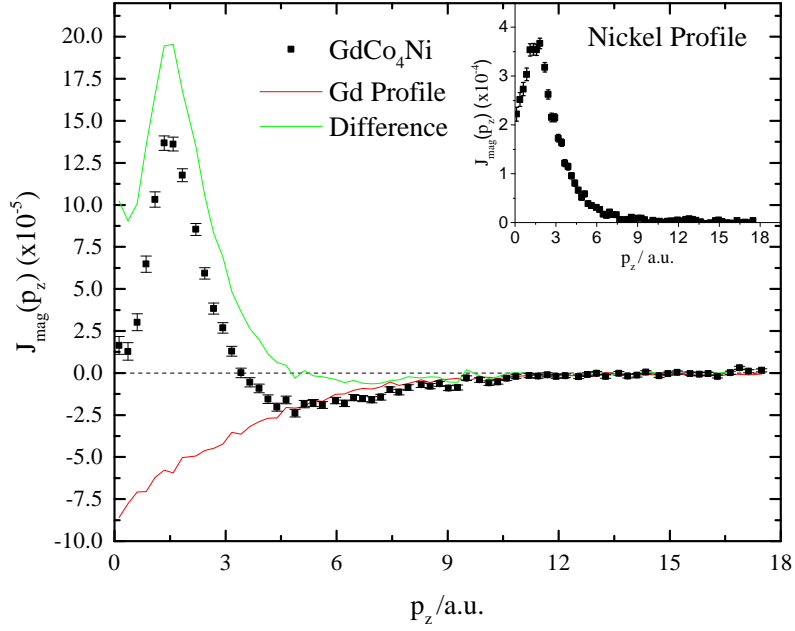
Figure 4.3: Compton profile of GdCo$_4$Ni (Black squares) with gadolinium profile (red) and difference (green) i.e. GdCo$_4$Ni profile − Gd profile. Inset shows a nickel profile, collected at 300K and 2T, to give a reference of a 3d system.

where $p_z \geq 4A.U..$ This gives the gadolinium contribution to the Compton profile. The difference between the profiles, shown in figure 4.3 in green, is a typical 3d shaped profile (as is demonstrated by the nickel profile in the inset). This reinforces the idea that the profiles are made of 4f and 3d sublattices.

The value of momentum, $p_z \geq 4A.U.$, chosen to be the zero value of the fit (i.e the Gd profile was fit to the data above this value), was chosen by eye. This took into account the point at which the gadolinium contribution was dominant in the experimental profile. This fit was not strenuously tested, for different values of p_z, due to time constraints. Further work is required to confirm the results of this chapter. The work done provides a starting place for this further study.

In addition, an experimental Gd profile was used in this fitting, therefore introducing experimental errors on the fit. This further work may include the use of theoretical profiles to check for agreement.

4.3.2 GdCo$_{3.72}$Ni$_{1.28}$

GdCo$_{3.72}$Ni$_{1.28}$ along with GdCo$_3$Ni$_2$, of the four samples referred to in this chapter, were the samples on which the most investigation was carried out. This was due to the compensation temperature for these two samples being comfortably within the measurable range (10K-300K). Figure 4.4 shows all the moments collected at all the temperatures, this has been split into four regions based on the behaviour of the moments.
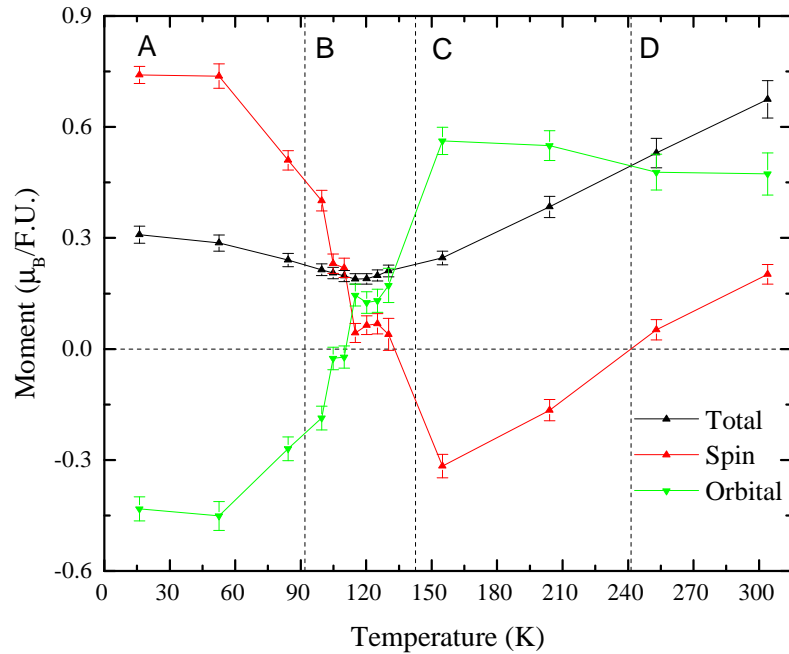
Figure 4.4: Total (black), spin (red) and orbital (green) moments for GdCo$_{3.72}$Ni$_{1.28}$ at 2T. Four regions (A, B, C, and D) have been defined based on the behaviour of the moments and are explained in the text.

Figure 4.4 clearly shows the point at which the spin moment changes sign and the orbital moment dominates the system, occurring just above $130K$, at the boundary of region C. After this the spin moment increases, it changes sign again at between $200K$ and $250K$ at the boundary of region D.

Figure 4.5 shows what is happening to the contributions to the spin moment. Starting with the $4f$ contribution the sign flips at the minima of the total moment
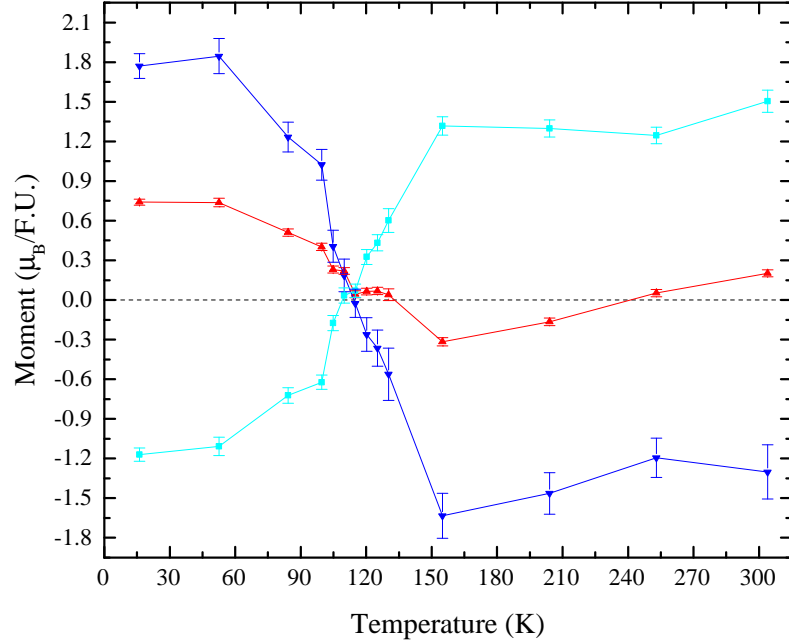
Figure 4.5: Total spin moment (red) (as in figure 4.4) with contributions to the spin moment from the $3d$ (light blue) and $4f$ (dark blue) orbitals for GdCo$_{3.72}$Ni$_{1.28}$ at 2T. Using the same regions as figure 4.4.

(region B). However the $4f$ spin moment remains larger than the $3d$ spin moment, causing the total spin moment to become negative, (region C). This is due to an orbital moment attached to the $3d$ orbitals. At the point where the anti-parallel $4f$ moment has reduced to less than the parallel $3d$ moment, the spin moment becomes positive again. (Region D boundary)

The behaviour of these four regions (A, B, C, and D) are shown in figure 4.6. Region A represents the region where the gadolinium sublattice dominates, there is a large total spin moment (red) parallel to the gadolinium contribution (dark blue) and antiparallel to the orbital moment (green) and the cobalt-nickel contribution (light blue). Region B represents the transition region in which the moments are flipping. In addition to this there is a possible canting as discussed below. Region C represents the region where the cobalt-nickel $3d$ sublattice is aligned with the total moment and the applied field, and it is antialigned with the larger gadolinium moment. This means that the total spin moment is negative and the system is
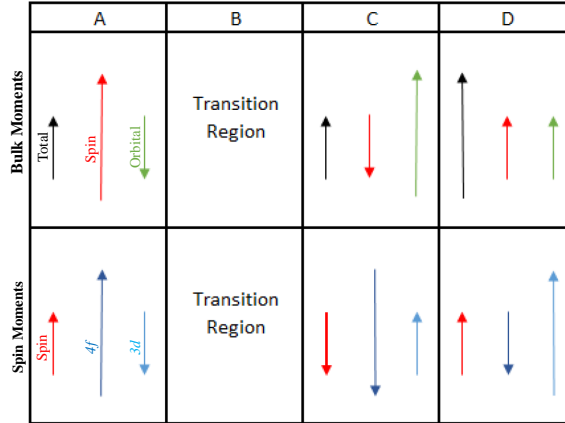
Figure 4.6: Sketch of the alignment of the moments in GdCo$_{3.72}$Ni$_{1.28}$ in the four regions discussed. Colours match figures 4.4 and 4.5 i.e. total moment in black, spin moment in red, and orbital moment in green in the top figure and the total spin moment in red and the $3d$ and $4f$ contributions in light and dark blue respectively.

dominated by the orbital moment, aligned with the $3d$ spin contribution.

The transition temperature can be seen to be between $\approx$ 110K and $\approx$ 130K. However, defining a transition temperature as a minimum of the total magnetism, as previous studies have, is no longer a sensible definition. This is because the minimum in the total moment is at 115K, the temperature at which the spin moment passes zero is $\approx$ 130K for the first time, a second transition temperature could be defined as the second point the spin moment passes through zero at $\approx$ 240K and, thirdly, the temperature that the $3d$ and $4f$ moments pass through zero is 110K. Any of these temperatures could be used to define a transition temperature.

Comparing the Compton profile obtained at 16.1 K (in region A) to the profile obtained at 304 K (region D), figure 4.7 clearly shows the change in sign of the two contributions. The high momentum region, dominated by the localised $4f$ electrons, is positive at 16.1 K and is negative at 304K. At low momentum the sign on the $3d$ moment also changes between low and high temperatures. In addition, the ratio of these moments change with temperature, implying a different temperature dependence to the moments of the sublattices.
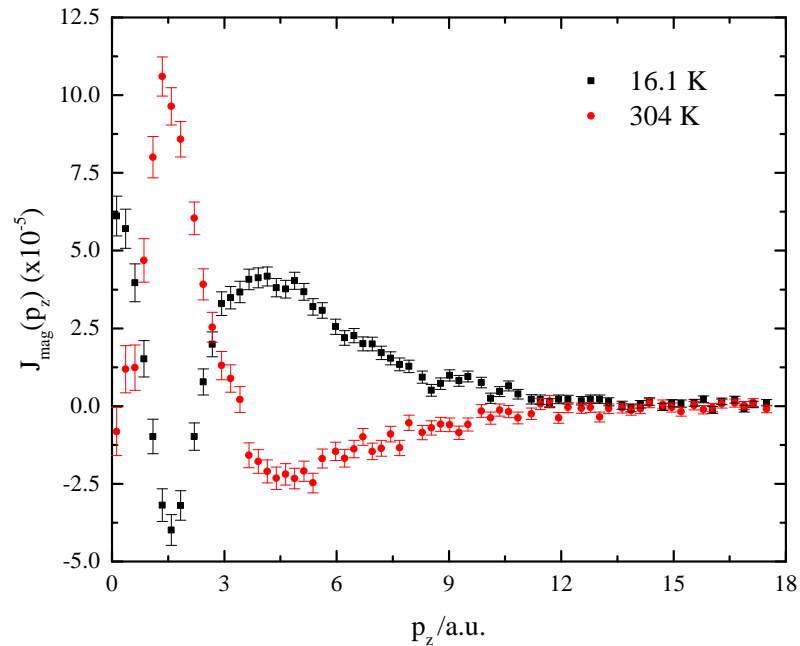
Figure 4.7: Compton profiles of $GdCo_{3.72}Ni_{1.28}$, obtained at 16.1K (black) and 304K (red). Both profiles were obtained at 2T

A second important comparison is between 115K and 130.2K, both within the transition region (B). This is shown in figure 4.8.

The comparison in figure 4.8 is interesting because, as can be seen in figure 4.5, whilst the spin moment plateaus between these temperatures, the contributions in this region changes dramatically. As is seen in figure 4.8, whilst both profiles have the same area, at 130.2K there are much larger contributions from the sublattices. The size of the contributions to the spin moment are shown in figure 4.5, coloured light and dark blue and are calculated by fitting a gadolinium profile to the data. The clear change in shape of the profiles in figure 4.8 explains the change in the contributions in figure 4.5.

Looking at a profile before and after the spin moment changes sign for the second time, i.e. a profile in region C and D respectively, shows that there is not a drastic change in the profiles. Figure 4.9 shows a comparison between the profiles at 155 K and 304 K. The change in sign in the total spin moment is due to a gradual
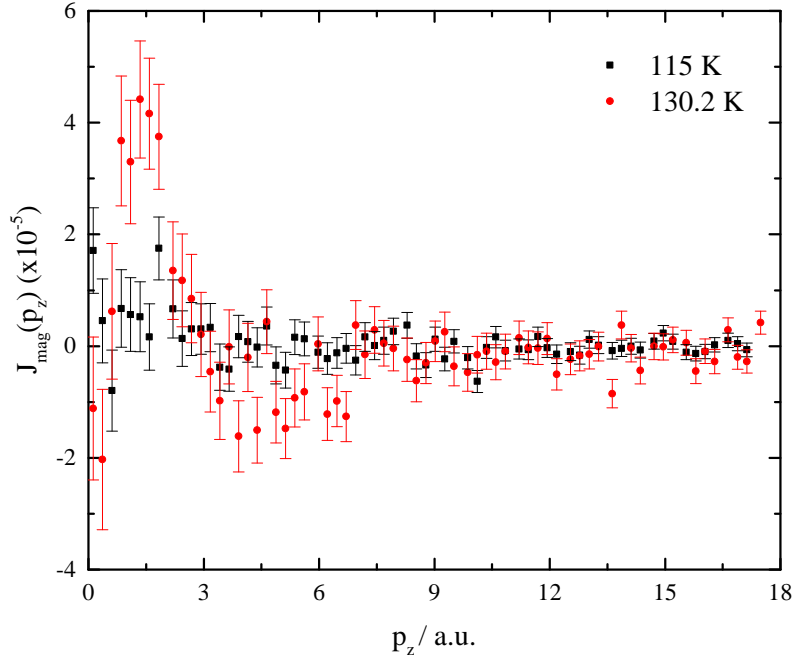
Figure 4.8: Compton profiles of GdCo$_{3.72}$Ni$_{1.28}$, obtained at 115K (black) and 130.2K (red). Both profiles were obtained at 2T

decrease in the $4f$ moment whilst the $3d$ moment remains comparatively constant.

4.3.3 GdCo$_3$Ni$_2$

GdCo$_3$Ni$_2$ was the second of the four samples to have its transition temperature within the range measured. The transition temperature is between 230 K and 280 K. However, unlike GdCo$_{3.72}$Ni$_{1.28}$, the temperature at which the parallel $3d$ spin moment is larger than the anti-parallel $4f$ spin moment and the total spin moment becomes positive again (defined as the boundary of region D above) is outside the range measured (> 300 K). This is seen in figures 4.10 and 4.11.

Previous studies find the transition temperature to be 230 K [56]. This fits reasonably with the data which shows a transition temperature between the measured 229 K and 279 K. However, once again, the validity of only using the minimum of the total moment to calculate the transition temperature is in question.
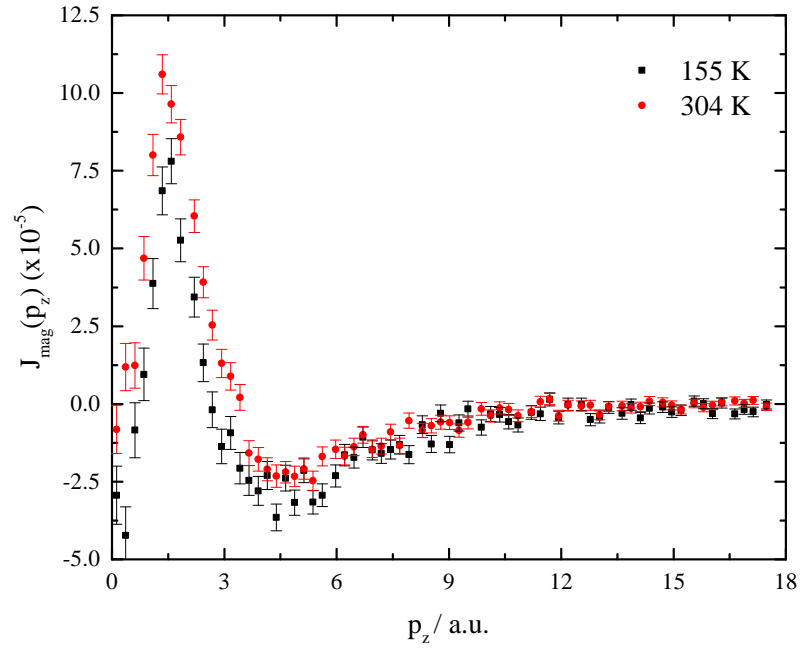
Figure 4.9: Compton profiles of $GdCo_{3.72}Ni_{1.28}$, obtained at 155K (black) and 304K (red). Both profiles were obtained at 2T
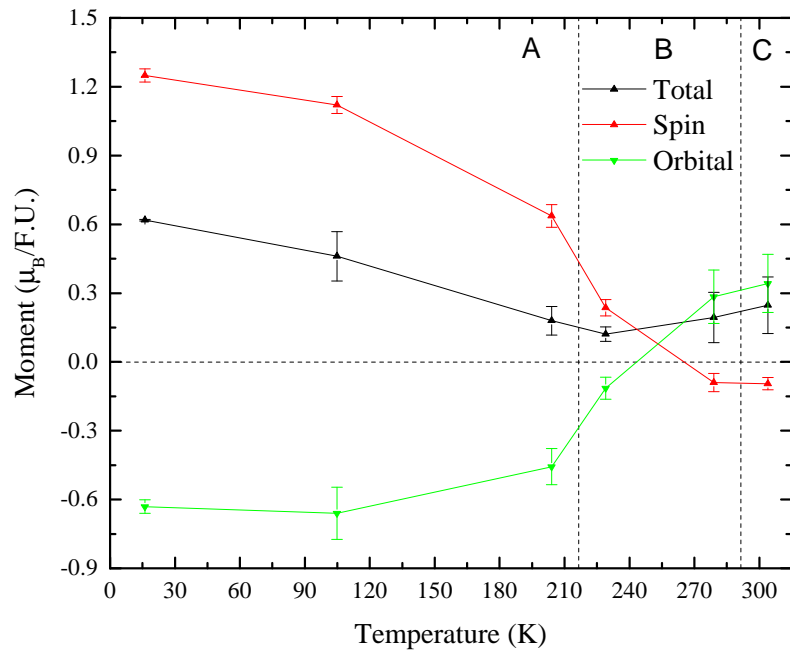
Figure 4.10: Total (black), spin (red) and orbital (green) moments for $GdCo_3Ni_2$ at 2T. Using the same concept of region discussed above (region D is at too high a temperature and was not measured for this sample)
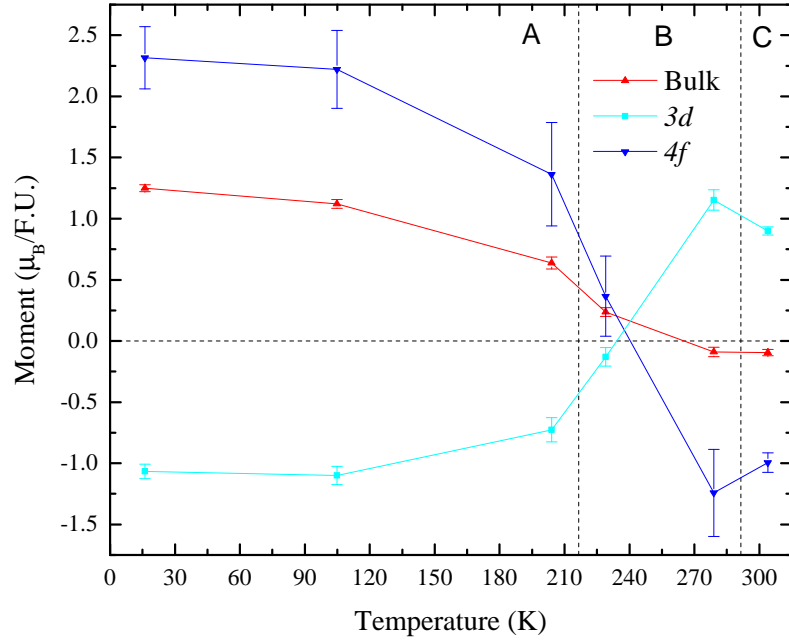
Figure 4.11: Total spin moment (red) with contributions to the spin moment from the $3d$ (light blue) and $4f$ (dark blue) orbitals for $GdCo_3Ni_2$ at 2T. Separated into three regions discussed in text as in figure 4.10.

4.3.4 $GdCo_2Ni_3$

$GdCo_2Ni_3$ was measured at five temperatures within the achievable temperature range but, like $GdCo_4Ni$, the temperature at which the spin moment changes sign was outside the experimental range. However, unlike $GdCo_4Ni$, it is too high a temperature, i.e. above $300K$. A. Tedstone *et al.* found the compensation temperature to be 323K [56]. Figures 4.12 and 4.13 clearly show the moment tending towards a point above 300K but it is not possible to extrapolate an exact temperature. This suggests that it would follow the same pattern as the previously discussed samples in this series if it were possible to measure this sample to a higher temperature with this set-up.
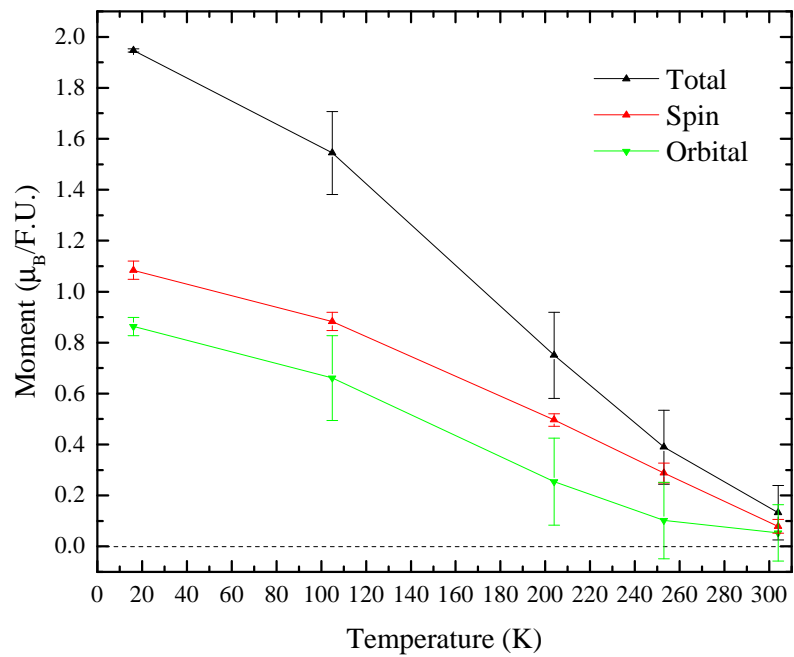
Figure 4.12: Total (black), spin (red) and orbital (green) moments for GdCo$_2$Ni$_3$ at 2T.
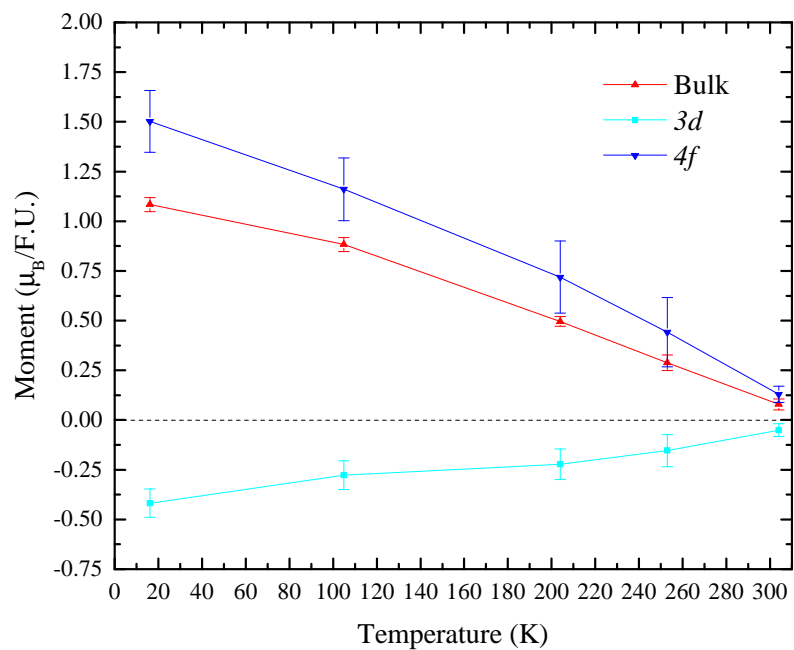
Figure 4.13: Total spin moment (red) with contributions to the spin moment from the 3d (light blue) and 4f (dark blue) orbitals for GdCo$_2$Ni$_3$ at 2T.

4.4 Discussion

The four samples investigated showed increasing transition temperatures with increasing nickel content. This supports the theory of the electronic structure discussed above and agrees with previous literature [55; 56].

Looking at the samples as a series, a few interesting trends appear. Firstly, the total moment reaches a minimum value at the compensation temperature but does not reach zero. It has been suggested that a cause of this is that with $RETM_5$ sufficiently high fields can cause the moments on the sublattices to precess from ferrimagnetic to ferromagnetic. These samples stop being ferrimagnetic at a field B_1 and become ferromagnetic at a second field strength B_2. For values of field between these values the moments cant, creating a non-collinear phase [71]. For $GdCo_5$ this first field, B_1, was calculated theoretically to be 46.1 T at 0 K [73] and found experimentally to be 46 T at 5 K [72], much higher than the 2T measured at. However, it was found in $GdCo_{12}B_6$ that also has a compensation point, that this value of B_1 decreases as the temperatures approach the compensation point [71]. This has been proposed as the reason for the non-zero magnetisation [56].

Another interesting point is that, as seen in figures 4.5 and 4.11, the flipping of spins at the compensation temperature does not happen when the two spin contributions are equal; this is made clear by the fact that the total spin moment continues to drop after this point. The compensation temperature occurs when the $3d$ spin and orbital moments are greater than the gadolinium spin moment, which allows a negative spin moment because the orbital moment dominates the system. This is seen in region C in figures 4.4 and 4.10. The fact that the orbital moment found closely follows the shape of the cobalt moment tells us that orbital moment stems from the $3d$ orbitals. This is reinforced by Hund's rules that postulate that there is no orbital moment on gadolinium.

This leads to an unexpected result from the data where $GdCo_2Ni_3$, with

the largest amount of nickel, has an orbital moment that is opposite to the $3d$ moment. This result is different from the other three samples at all temperatures and requires further investigation to establish whether this continues with increasing nickel content. Another technique, such as X-Ray Magnetic Circular Dichroism (XMCD), could be used to check this unexpected result. One possibility is that the cobalt-nickel sublattice is disordered enough to quench the orbital moment on the $3d$ moments. However, it is still unexpected that the orbital moment would align with the gadolinium moment or antialign with the $3d$ moment. To investigate this, the first step would be to repeat the measurements of the moments and then, ideally, obtain data on other samples with large nickel content, $x > 2$. This comparison would allow us to see if this effect is observable in other samples of similar nickel content, and if a value when this effect first appears can be ascertained. Further DFT theory work could also be used to attempt to discover the cause of this result.

The transition temperature of $GdCo_{3.72}Ni_{1.28}$ appears to be very broad, taking approximately 100K to completely flip spins. This broadness makes it difficult to accurately find a transition temperature. This could be due to the mechanism of the flipping of spins discussed above, as the 2T field could be causing increasing quantity of the moments to cant by increasing angles. However, a second possibility could be the purity of the samples. Whilst with these samples, the values of x are well characterised there is a possibility that there are nickel or cobalt rich regions within the crystal (the average composition of the entire crystal being the known value of x). This would cause the nickel deficient regions flipping at a lower field than the nickel rich regions, smearing out the transition. The moments started to flip between 52.6K and 84.3K and had definitely finished between 130.2K and 155K. Assuming the maximum range, and extrapolating from given values [56], the maximum range of values for x would be $1.1 \gtrsim x \gtrsim 1.4$, and likely less. A possible solution to this would be to first repeat the experiment at different fields to see if there is a significant change to the width of the transition. A second option would

be to repeat the experiment using a single crystal, if available.

4.5 Conclusion

In this chapter, four samples of $GdCo_{5-x}Ni_x$, with increasing levels of nickel were investigated. Two of these samples had transition temperatures within the measurable range ($10 \leq T \geq 300$), these were $GdCo_{3.72}Ni_{1.28}$ and $GdCo_3Ni_2$ ($x = 1.28$ and $x = 2$). $GdCo_3Ni_2$ has previously been experimentally shown to have a transition temperature of 230K [56]. Whilst the work in this chapter agrees with this result, the investigation of the spin moments, on the separate sublattices, suggests that this is no longer a sensible characterisation of this series of samples. This compensation temperature is only defined as the minimum of the bulk total moment and therefore hides the complexity of this region. Potentially a more useful, or interesting, characteristic to define, would be the two temperatures at which the bulk spin moment passes zero, or the range of temperatures at which the spin moments on the sublattices cancel each other out, and the system is driven by the bulk orbital moment.

$GdCo_{3.72}Ni_{1.28}$, found a transition temperature to be between $\approx 110K$ and $\approx 130K$, which follows the pattern of transition temperatures found in this chapter and demonstrated in literature. The large temperature range over which the transition takes place suggests similar complex behaviour to $GdCo_3Ni_2$. However, with this sample, as the transition temperature was more centred on our experimental range, and more data points were gathered, this behaviour was even clearer. Over the range of temperatures where the moments on the sublattices have approximately the same magnitude, although opposite sign; cancelling each other out, Compton profiles at several points were obtained. It is immediately clear, in these Compton profiles, that there is a large change in this magnitude of the moments. This is abundantly clear in figure 4.8, which shows a comparison between the Compton profiles at 115K and

130.2K. Whilst both of these temperatures are within the 'transition region; B', and both have low total moments, there is a large difference in the contributions from the sublattices which is immediately visible in the figure. In addition, the spin moment on the sublattices compensate a second time at a significantly higher temperature; where the total moment is comprised exclusively of the orbital moment. Whilst this is not seen in $GdCo_3Ni_2$ as it is outside the experimental range, it is observed in this sample, where it occurs at approximately 240K. This second compensation point, and the temperature range between them, where the spin moment is significantly negative, can not be seen on any technique that measures the bulk total moment. This makes Compton scattering a particularly useful technique to investigate this phenomena.

A single Compton profile was obtained for $GdCo_4Ni$ at 300K. Whilst one result can not confirm the ideas supposed from the other samples it equally does not contradict any of the conclusions drawn and follows the pattern expected, i.e. having a positive $3d$ moment and a negative $4f$ moment at high temperature.

All these samples, except $GdCo_2Ni_3$, had the bulk orbital moment being parallel to the cobalt-nickel $3d$ spin moment. In $GdCo_2Ni_3$ however, the orbital moment is positive and antiparallel to the cobalt-nickel $3d$ spin moment. Despite this the spin moments, for this sample, both the total and the $3d$ and $4f$ contributions, followed the expected trend, i.e. the gadolinium moment is positive and the cobalt-nickel moment is negative (the expected transition temperature of 323K [56] is outside the experimental range). This difference in orbital moment to the other three samples requires more research. A repeat of the Compton scattering experiment, in order to replicate the result and rule out experimental error, as well as more profiles and moments from samples, with a similar nickel doping, would aid in understanding. Theoretical work using DFT codes could also be used to further understanding of the change in pattern observed in this sample.

Chapter 5

Spin and Orbital Moments of the Pyrochlore Iridate, $Nd_2Ir_2O_7$

5.1 Introduction

$Nd_2Ir_2O_7$ has a cubic pyrochlore structure. Along with other pyrochlore iridates of this structure, $Nd_2Ir_2O_7$ has attracted a great deal of interest due to strong spin-orbit coupling and electron correlations [74]. $Nd_2Ir_2O_7$ has shown, experimentally and theoretically [75], to have novel transport properties, for example, a possible metal to insulator transition (MIT) from a magnetically ordered insulator to a disordered metallic phase. [76]

This novel behaviour has been attributed to the Ir^{4+} $5d$ electrons, which, together with the Nd^{3+} $4f$ electrons, comprise the magnetic electrons that contribute to the magnetism in this material. In this chapter two nominally identical samples of $Nd_2Ir_2O_7$ are investigated. These samples produce different total, spin and orbital moments, and were studied in an attempt to discern any observable change which could explain this discrepancy. Earlier studies have also found differing results for

both the existence and temperature of the MIT, [77; 78] the total magnetism, and the spin and orbital contributions. It has been suggested that this is due to extremely small changes to the stoichiometry of the samples, of the order of around 1% [79]. It is probable that the biggest source of the discrepancy in this material is due to the different synthesis methods.

The previous studies for these samples have a tendency to disagree with each other on several of the physical and magnetic properties of the samples. Many of the studies are similar to one another, with small changes in technique or theory while other are repetitions to confirm or disprove others' work.

A particular area of interest to our study is the proposed MIT, as discussed above. While these studies disagree on these properties, an attempt to add to the discussion by using Magnetic Compton scattering to observe a change, or lack thereof, of magnetic behaviour and configurations has yet to be done. This technique may not be the most powerful to be using, in this instance, and has issues with regards to the samples used. These are discussed in detail below. However, it was deemed worth the effort to perform the experiment and test whether it could add support to one side or the other. The impact of this study to the current state of the art knowledge is examined in the discussion.

5.1.1 Iridates

Iridate compounds continue to attract interest for several reasons [80], particularly their electron-electron correlation effect and unusual phase transitions proposed in several of these materials [81], and the behaviour of the $5d$ electrons in the iridium, which are highly material dependent. These electrons can cause many interesting magnetic and electronic phases, such as topological Mott insulator, Weyl semimetals and axion insulators [82]. This also makes it difficult to accurately predict the behaviour of the material.

Two other materials were proposed for this project, $CaIrO_3$ and Sr_2IrO_7.

67

CaIrO$_3$ shows a phase transition from a perovskite phase, space group *Pbnm*, to a post-perovskite phase, space group *Cmcm* [83]. In addition, like the other iridates, there is strong spin-orbit coupling driving the groundstate [84]. Sr$_2$IrO$_7$ has strong spin-orbit coupling and electron correlations that give rise to a Mott insulator. Also its similarities to La$_2$CuO$_4$ have suggested that it would be a good candidate for novel states of matter, such as unconventional superconductivity (with doping) [85; 86]. However, the spin moments on the samples of CaIrO$_3$ were too small to be measured and the samples of Sr$_2$IrO$_7$ were physically too small to measure with the current experimental setup.

5.1.2 Pyrochlore Iridates

Nd$_2$Ir$_2$O$_7$ belongs arguably to one of the most interesting iridates as a result of the intriguing phase diagram namely the pyrochlore, or 227, iridates. These materials have the structure A$_2$Ir$_2$O$_7$. Several noteworthy and novel phases are predicted within these materials, caused in the main by the strong spin-orbit coupling, including topological Mott insulators, Weyl semimetals and axion insulators [87; 88; 89; 90]. This series has been investigated experimentally and both chiral spin liquid states and quantum critical semimetalic states have been observed in Pr$_2$Ir$_2$O$_7$ [91; 92; 93] and MITs have been observed in A$_2$Ir$_2$O$_7$ with A = Lu to A = Nd [94; 95]

Through changing the species, A, where A is a lanthanide, a transition from magnetically ordered insulators to spin-disordered metals, is seen; the temperature of this transition decreasing as the ionic radius increases. This transition is predicted to occur at 0 K at an ionic radius 'between' that of Nd and Pr [79], this is a quantum MIT. Neodymium iridate is the A$_2$Ir$_2$O$_7$ compound that is closest to this expected quantum transition. Note that Nd$_2$Ir$_2$O$_7$ is still expected to show this MIT, although not at zero temperature [78].

In Nd$_2$Ir$_2$O$_7$ the MIT temperature has been widely disputed. It has been found in some studies to be approximately 27K - 36K [79; 74] whilst in other cases a

MIT is not found at all [76; 96]. Other studies that investigated doping the sample, either with Ca [80], or with Pd (the next lanthanide in the series) [97] found large differences in the MIT with small amounts of doping, adding weight to the argument that these differences are driven by the stoichiometry.

5.2   Crystal Structure

$Nd_2Ir_2O_7$ has the space group Fd-3m and a lattice constant a=10.3768Å with eight formula units in the unit cell. The neodymium ion occupies the $16d$ site at (1/2, 1/2, 1/2), the iridium ion occupies the $16c$ site at (0, 0, 0), and the oxygen occupies the $48f$ site at (x, 1/8, 1/8), and the $8b$ site at (3/8, 3/8, 3/8) [98] (for $Nd_2Ir_2O_7$ $x = 0.330$ [82]). This structure, as seen in figure 5.1, is the 227 structure discussed above and is referred to as a pyrochlore compound.
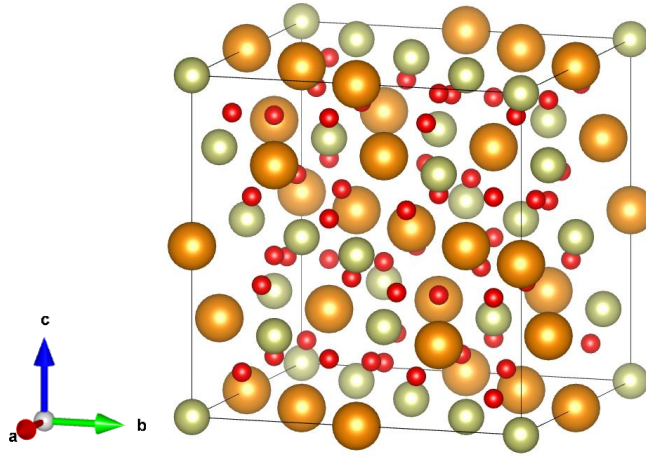
Figure 5.1: Structure of $Nd_2Ir_2O_7$.

This structure consists of two interpenetrating sublattices, each formed of corner sharing tetragonal structures of the neodymium and iridium ions respectively [99], called the pyrochlore lattice [100]. A portion of the iridium sublattice is shown in figure 5.2, demonstrating the corner sharing tetrahedra.
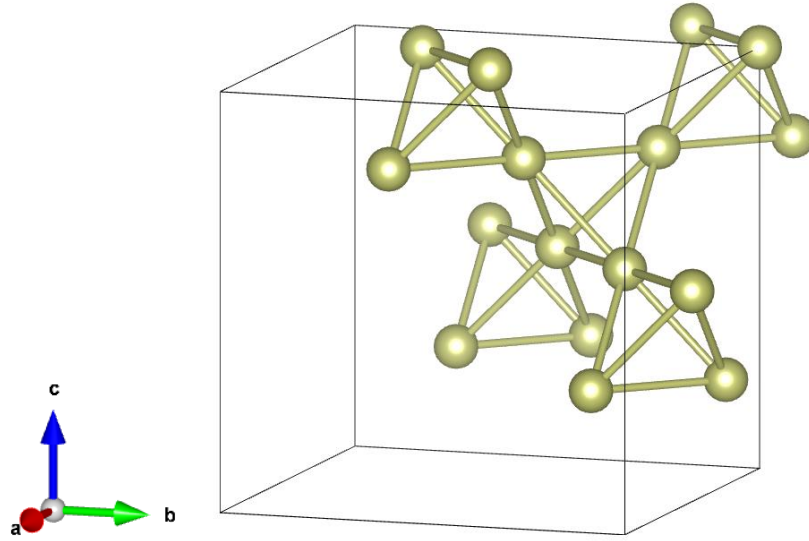
Figure 5.2: Structure of the iridium sublattice, showing the corner sharing tetrahedra.

5.3 Electronic Structure

The $4f$ electrons in neodymium and the $5d$ electrons in iridium contribute to the magnetisation in $Nd_2Ir_2O_7$. Spin and orbital moments are expected on both these species. In this material neodymium forms Nd^{3+} ions which have the electronic configuration $[Xe]\ 4f^3$, (neodymium atoms have the structure - $[Xe]\ 4f^4\ 6s^2$). The unpaired $4f^3$ electrons contribute to the magnetism of the material. Using Hund's rules, discussed in chapter 2, the first rule gives $S = \frac{3}{2}$, the second rule gives $L = 6$, and the third rule give $J = \frac{9}{2}$. The spin-orbit ratio of neodymium $4f^3$ electrons can be assumed to be -0.5, which means that the orbital moment is opposite to and twice the size of the spin moment. Using these rules, it is possible to calculate the contributions to the orbital and total moments of both the neodymium and iridium, if the spin moment contributions are known. 4f electrons are very localised in space, which means their MCP are highly broad in momentum space. For the MCP of

$Nd_2Ir_2O_7$ the tails at high momentum will be completely due to the neodymium $4f$ electrons since the momentum density of the iridium $5d$ would have be at to zero by this point, (approximately 4 A.U.). This allows the two contributions to be separately identified.

This zero point of 4 a.u. was chosen by eye, as where the neodymium 4f dominates, and the iridium $5d$ has reached zero. In further study, this needs to be more rigorously checked. Trialling other values, other than 4 a.u., would allow for higher confidence in the results and conclusions. This process of checking the data is hampered by the experimental noise, however. The small moment, at low a.u., once the Nd has been subtracted is assumed to be Ir, however experimental noise, or fitting error, can not be ruled out as a possibility for this residual moment. Without a cleaner and clearer profile it is not possible to rule this out. An attempt to produce a iridium contribution, by subtracting the neodymium profile from the experimental data, was not performed as the level of experimental noise in the data would not have produced a clear profile. Unfortunately, it was not possible to use GAMESS calculations to define this contribution as we did not have the necessary computing power needed. Presently, variations in the results and conclusions, caused by small changes to this zero value, would be lost. Despite these limitations, the value chosen within this thesis allows us to consider the behaviours observed. Future studies, with clearer data, will prove or disprove the conclusions made.

Ir^{4+} ions, as iridium forms in this sample, has the structure $[Xe]\ 4f^{14}\ 5d^5$, (iridium atoms have the electronic structure - $[Xe]\ 4f^{14}\ 5d^7\ 6s^2$). The contributing electrons are the $5d^5$, these electrons are less localised than the $4f$ electrons in Neodymium and therefore form a narrower MCP. $5d$ electrons have a less defined spin-orbit ratio as it is dependent on the species and the material. These $5d$ electrons have strong spin orbit coupling with a $J_{eff} = 1/2$ [99], as it is proposed that they occupy t_{2g} orbitals. However it has also been suggested that there is possibly some mixing of the t_{2g} and e_g orbitals [101] and due to this, metallic ground states would

71

be expected. However, these strong spin orbit interactions allow a gap to open and create Mott-like insulating ground states. These states can be observed in many iridates such as Sr_2IrO_4 [102].

One suggestion is that the moments on these atoms form an all-in-all-out structure (AIAO). This means that the tetrahedra mentioned above alternate from their moments all pointing into the centre of the structure and all pointing out from the middle, this is shown in figure 5.3. These moments then cant in an applied magnetic field, creating a net moment for these structures and, therefore, the system [103]. The iridium tetrahedra has an AIAO order whilst the neodymium sublattice forms a similar all-out-all-in order (AOAI). Under an applied field the neodymium moments can become canted and will suddenly flip to a 3-in-1-out order. This can induce a change in the iridium sublattice from a AOAI order to an AIAO order [104]. In the cases where no MIT is found, a two-in-two-out structure is proposed [96]. Since this chapter investigates a polycrystalline powder, it is not possible to see evidence of this in the results or investigate the effects.

5.4 Synthesis and Characterisation

5.4.1 Nominal Composition and Different Synthesis Methods

For these experiments, a polycrystalline powder was used. This powder was compressed into a pellet with no adhesive so that only the sample itself would be measured. Two of these thin samples were attached to each plate to increase the scattering volume whilst reducing the chance that an air pocket in the sample would cause it to break when placed in a vacuum. The size and weight of these compressed powders was measured, and the density of these samples were found to be approximately 40 times less dense than a solid grown sample. This, in itself, creates further problems due to the drastic drop in scattering volume this causes. As mentioned above, it is suspected that tiny variations in the stoichiometry cause the
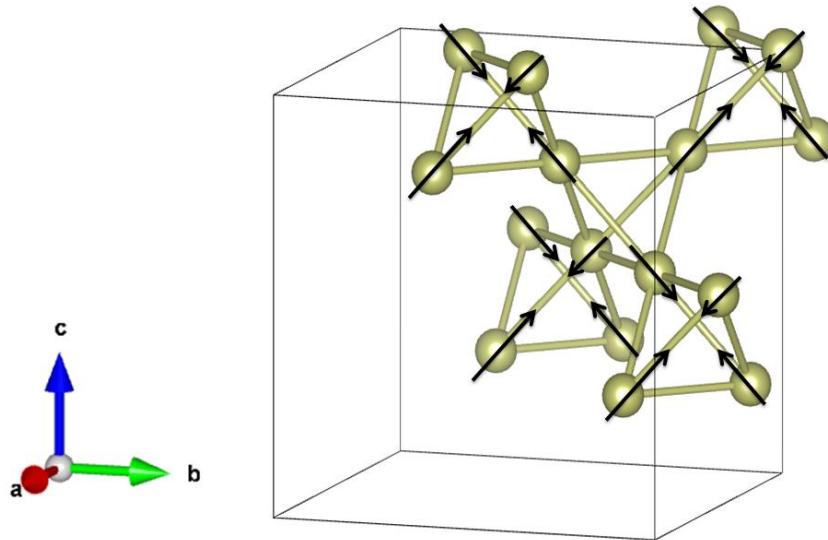
Figure 5.3: Structure of the corner sharing sublattice showing the all-out-all-in magnetic order.

large variations seen in the properties of different samples [105]. The samples that were measured were synthesised using two different methods; sample 1, which most of this chapter focuses on, was synthesised using the hydrothermal method, while sample 5 was synthesised using the solid state method [94].

5.4.2 SQuID Magnetometry

To calculate the spin and orbital moments and the contributions from the atom species it is important to measure the total moment of the different samples. As discussed in chapter 4, the method used to measure the total moment was SQuID magnetometry from which both M vs H and M vs T curves were obtained. As is shown in figures 5.4 and 5.5 and as discussed above, there is a large variation in the magnetism between the samples, likely due to differences in stoichiometry. The lack of hysteresis in the curve at 2K, in both samples, shows that it is a very soft ferromagnet. There is no hysteresis visible in any other temperature, though the

curves are more paramagnetic. Referring back to figures 5.4 and 5.5 it is shown that the moments decrease rapidly as the temperature increases.
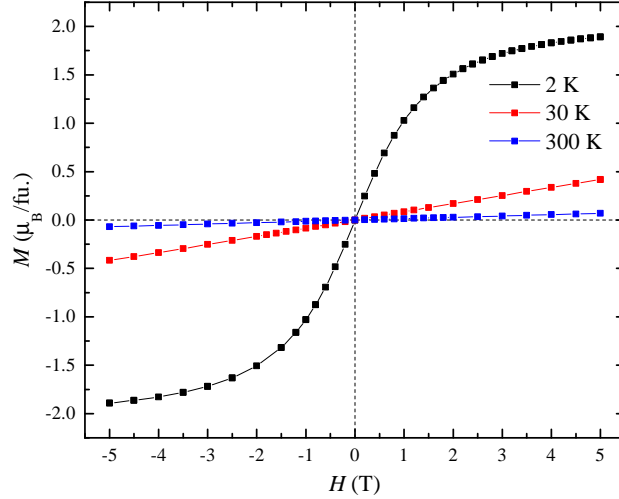
Figure 5.4: MvsH curve for $Nd_2Ir_2O_7$ (Sample 1) at 2K (black), 30K (red) and 300K (blue).

5.5 Results

5.5.1 MCPs and Spin Moments

The magnetic Compton profile was measured on sample 1 at 2K, 5K, 10K, 20K, 30K, 60K, and 300K whilst sample 5 was measured at 2K, 30K and 300K for comparison. The results at 300K have not been included in all the figures below as the moment is very small, the errors are large and there is a large temperature difference with the next highest temperature (60K), making it problematic to clearly show on a graph.

Calculations, using GAMESS, were used to obtain a theoretical profile for the neodymium $4f$ contribution to the total profile. This was then spherically averaged to obtain a polycrystalline signal. As the neodymium $4f$ moments are a lot more localised than the iridium $5d$ moments in momentum space they have a
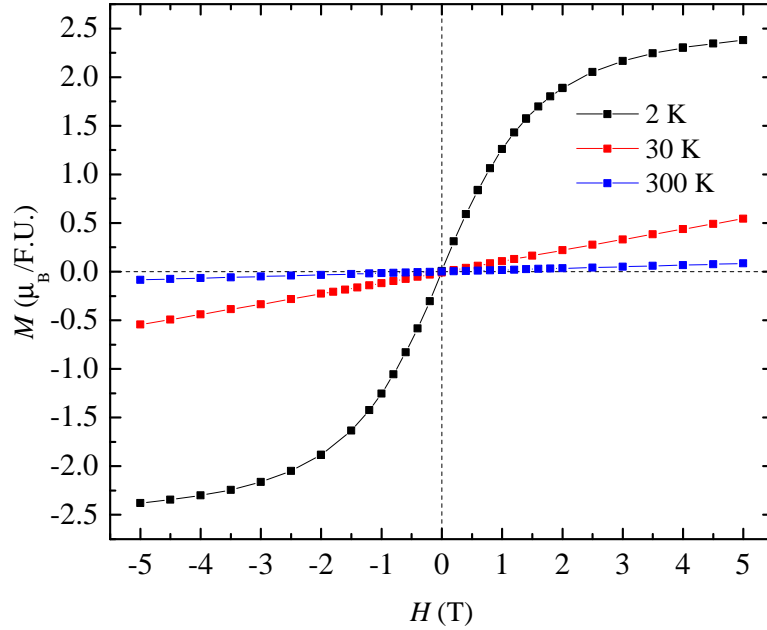
Figure 5.5: MvsH curve for $Nd_2Ir_2O_7$ (Sample 5) at 2K (black), 30K (red) and 300K (blue).

much broader Compton profile. This can be thought of as a result of Heisenberg's uncertainty principle. Using this fact, we can fit this profile to the high momentum *tails* of the experimental profile, in this case above 4 A.U., figure 5.6. This gives us a way of separating out the neodymium contribution from the spin moment of the system. Below 4 A.U., the neodymium fit is below the data, therefore this low momentum narrow peak is the iridium moment. Comparing the neodymium spin moment to the total spin moment obtained experimentally gives the iridium contribution. These results are shown in figure 5.7. These suggest that, whilst the neodymium moment decreases over this temperature range like the total moment, the iridium moment stays constant within error.

5.5.2 Orbital Contribution

As mentioned above, the well categorised spin-orbit ratio of 4f electrons allows the orbital contributions of neodymium to be obtained as it is double and the opposite sign to the spin moment. The total orbital moment can be obtained by subtracting
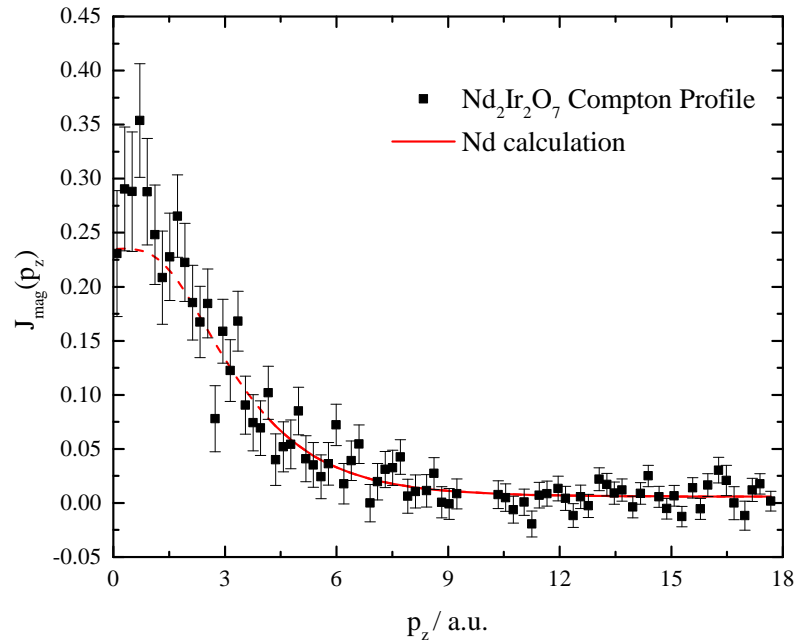
Figure 5.6: Magnetic Compton Profile of $Nd_2Ir_2O_7$ at 2K in black, GAMESS calculation for Nd in red. This red line is solid above 4 A.U., this is where the calculated profile is fitted to the data. Below 4 A.U. the calculated profile is shown with a dashed line.
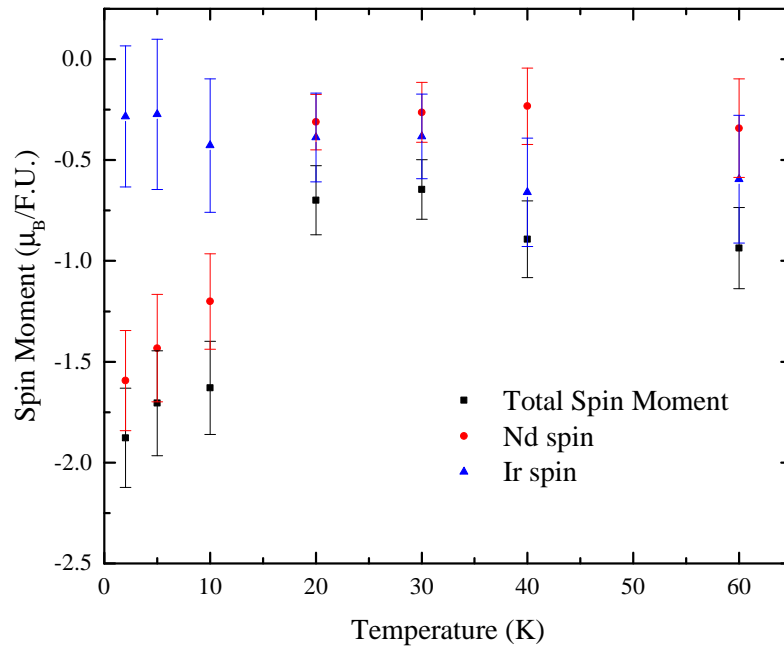
Figure 5.7: Spin moment of $Nd_2Ir_2O_7$ (Sample 1) against temperature, Total spin (black), neodymium spin (red) and iridium spin (blue).

the total spin from the total moment obtained using the SQuID. Using this total orbital moment, it is possible to also find the iridium contribution by subtracting the total orbital moment from the neodymium orbital moment. As is shown in figure 5.8, the orbital moments follow a similar pattern to the spin moments and, like the iridium spin moment, the iridium orbital moment stays constant within error over this range. As these results suggest, these iridium spin and orbital moments cancel within error providing no net total iridium moment. This implies a spin orbit ratio of -1 for the iridium contribution. It also suggests that all of the bulk total moment is from the neodymium atoms.

For both the spin, orbital and total moments, in both bulk and the separated contributions, sample 5 appears to follow the trends discussed for sample 1 (with different values for all the moments). However, more temperatures would have to be investigated to show this definitively.
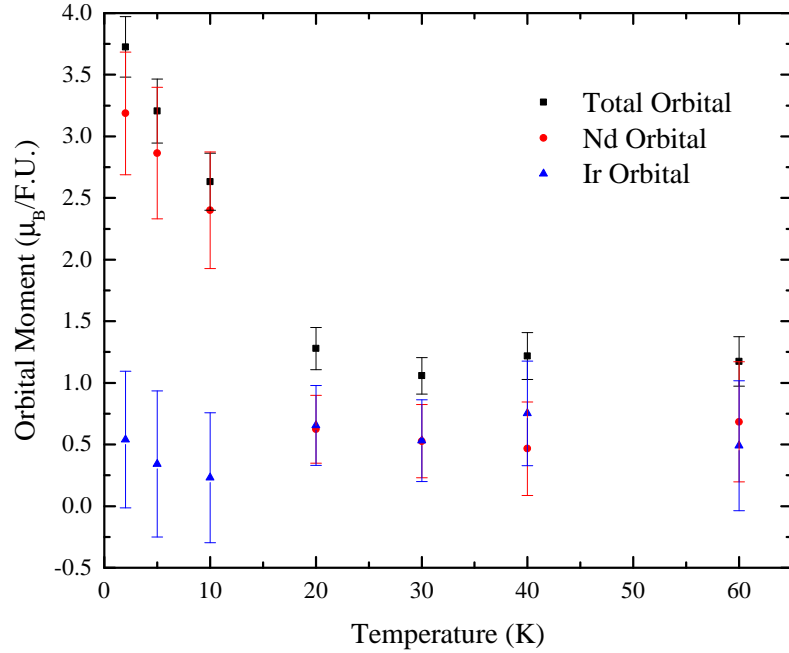
Figure 5.8: Orbital moment of $Nd_2Ir_2O_7$ (Sample 1) against temperature, Total orbital (black), neodymium orbital (red) and iridium orbital (blue).

5.5.3 Sample 1 vs Sample 5

		2K						30K					
		Sample 1			Sample 5			Sample 1			Sample 5		
Bulk	Total	1.85			2.38			0.41			0.54		
	Spin	-1.9	$\pm$	0.3	-3.5	$\pm$	0.5	-0.7	$\pm$	0.2	-0.9	$\pm$	0.2
	Orbital	3.7	$\pm$	0.3	5.9	$\pm$	0.5	1.1	$\pm$	0.2	1.5	$\pm$	0.2
	S/L	-0.50	$\pm$	0.07	-0.59	$\pm$	0.09	-0.6	$\pm$	0.2	-0.6	$\pm$	0.2
$4f$	Total	1.6	$\pm$	0.6	2.5	$\pm$	0.8	0.3	$\pm$	0.3	0.4	$\pm$	0.3
	Spin	-1.6	$\pm$	0.3	-2.5	$\pm$	0.4	0.3	$\pm$	0.2	-0.4	$\pm$	0.1
	Orbital	3.2	$\pm$	0.5	5.0	$\pm$	0.7	0.5	$\pm$	0.3	0.8	$\pm$	0.2
	S/L	0.5											
$5d$	Total	0.3	$\pm$	0.7	-0.1	$\pm$	1.1	0.2	$\pm$	0.4	0.1	$\pm$	0.4
	Spin	-0.3	$\pm$	0.4	-1.0	$\pm$	0.6	-0.4	$\pm$	0.2	-0.5	$\pm$	0.2
	Orbital	0.5	$\pm$	0.6	0.9	$\pm$	0.9	0.5	$\pm$	0.3	0.7	$\pm$	0.3
	S/L	-0.5	$\pm$	0.8	-1.1	$\pm$	1.3	-0.7	$\pm$	0.6	-0.8	$\pm$	0.5

Table 5.1: Comparison of results from sample 1 and sample 5 at 2K and 30K, including the total, spin, and orbital moments along with the spin-orbit ratio for the bulk sample as well as the contributions from the $4f$ and $5d$ sites. All moments are in $\mu_B/F.U.$

Table 5.1 shows the comparison between the moments from sample 1 and sample 5 at 2K and 30K. Sample 5 shows larger total and spin moments for the SQuID and the Compton measurements respectively, as well as a larger orbital moment at both temperatures. With regards to the moments from the $4f$ and $5d$ orbitals, whilst the moments are all bigger for sample 5 the ratio of $4f$ to $5d$ is 6 ± 7 for sample 1 and 2 ± 1 for sample 5. This could suggest a change in the ratio of neodymium to iridium in the sample, however, the small iridium moment (and its comparatively large error) make this difficult to conclude definitively. Data on sample 5 is included in table form only as a graph would not be useful. As only two data points were obtained, a graph would not be able to demonstrate any trends or conclusions. Table 5.1 best shows its comparison to sample 1.

5.6 Discussion

It has been suggested, by using μSR, that the iridium sublattice is ordered whilst the neodymium remains in a paramagnetic state [76]. This is difficult to separate out in the bulk technique of Compton scattering. As is shown in figures 5.7 and 5.8, large neodymium spin and orbital moments dominate at low temperatures with the neodymium spin moment being approximately 6 times larger than the iridium for sample 1 at 2K. As the temperature increases the neodymium spin and orbital moments rapidly decrease until they are close to the value of the iridium moment and, at approximately 20K, drop below the value for the iridium moment albeit the errors here are larger than the difference between the spin moments. From about 20K onwards iridium makes up at least half of the total spin moment on the sample and this is the same for the orbital moment.

The spin and the orbital moments of the iridium appear to cancel within error and therefore the bulk total moment is formed only of the sum of neodymium spin and orbital moments. Since the spin to orbit ratio of the neodymium is -0.5, the total moment of the sample is equal to half the orbital moment of the neodymium ions (or -1 times the spin).

This is clearly shown in figure 5.9, as the temperature increases from 2K to 60K, the spin to orbit ratio of the sample shifts from nearly -0.5 towards -1. This is as the sample becomes less dominated by the neodymium moments and more towards the ordered iridium moments. This is as expected as the neodymium is much more temperature dependent than the iridium which is approximately constant over this temperature range. Conversely, this is not what is expected from Hund's rules for iridium. Whilst a reason for this could be a more complex ground state than expected, or possible hybridisation between orbitals in the neodymium and iridium, another possible cause of this result is experimental factors.

As can be seen in figure 5.9, at 60K the error bar almost spans from the -0.5
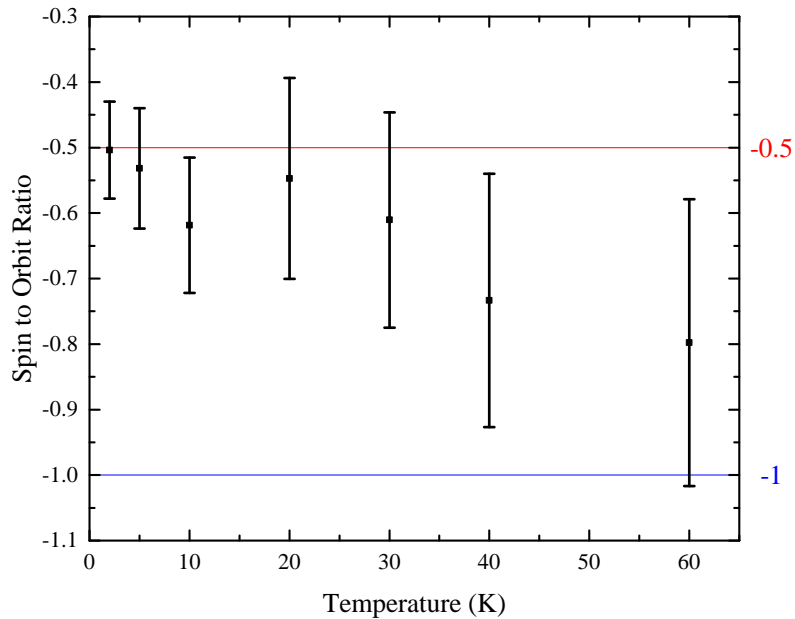
Figure 5.9: Spin to Orbit Ratio of $Nd_2Ir_2O_7$

to the -1 lines. The errors in the results are a direct result from the errors on the Compton profiles. The large errors have two causes, firstly, the moment/number of electrons in the formula unit being so small ($-1.88/330 \approx 0.0057$) (which is over three and a half times smaller than nickel which is used for the calibration sample ($0.56/28 = 0.02$)). This means that theoretically it would take over 12 times as long to get the same quality result. Secondly, it is made worse by the process of compressing the samples into a pellet (without any adhesive as that would have also been measured, creating a background that would not have been possible to separate out from the result). By necessity these samples were very thin, and the compressing created samples that were approximately 40 times less dense than solid $Nd_2Ir_2O_7$. The thinness and reduced density of the samples mean these sample have an extremely low scattering volume and this leads to a much-reduced signal to noise ratio. This led to the spin moment being measured experimentally at roughly three times smaller than the spin used after the background had been modelled and removed from the signal, which leads to large errors.

This large background is likely to be a cause of error in the spin moment. If the, mostly non-magnetic, background is underestimated it would likely lead to the measured spin moment to be smaller than the true spin moment. The total moment was measured in the SQuID and, as the pressed pellets would neither fit or survive breaking into smaller pieces without reverting to a powder, the samples were measured as a free to rotate powder. This, whilst measuring a more accurate result in terms of the total moment of the system, likely overestimated the total moment of the pellets measured in the Compton experiment. These two errors would both lead to an underestimating of the orbital moment but to what effect (and what degree) this would have on the spin to orbit ratio, is not possible to conclude.

Comparing the profiles at different temperatures, there is no sharp change in the shape around the proposed MIT that would help confirm the existence of the transition. However, the error bars on the data other than 2K make this difficult to determine, particularly with a very subtle change. This appears to agree with the conclusions found in [76; 77], which find no MIT at any temperature, but contrary to [100; 79], that find a MIT at around $\approx 36K$. To better confirm this, it would be useful to try more computational models to see if any change could be noticed, however the size of the unit cell and the number of electrons in the species make this difficult for many DFT codes. If there is no MIT in this sample, it could be due to the stoichiometry of the sample and could be present in other samples. Unfortunately, there are not enough data points on sample 5 to be able to postulate whether we can see a MIT in that sample.

5.7   Conclusion

Whilst there were not enough temperatures taken on sample 5 to reach a conclusion, the temperatures measured imply the same pattern measured in sample 1, as seen in table 5.1, but with a slightly higher moment. Sample 1's magnetism comprises

of a $4f$ moment on the neodymium and a $5d$ moment on the iridium. Separating out these contributions to the spin moment obtained from the Compton profile gives a highly temperature dependent $4f$ moment which at 60K is approximately 20% of the value at 2K. In contrast the iridium moment is constant, within error, over this range. The orbital moments follow a similar pattern, the neodymium moment is forced to follow the spin moment, by defining it from the spin-orbit ratio. However at all temperatures the iridium spin-orbit ratio is calculated to be -1, within error (however some of the errors are very large). This would imply that the total moment is only dependent on the neodymium spin and orbital moment. This is an unexpected result that would need further investigation as the current data is not sufficient to be confident in its accuracy. As discussed the best way to improve this experimental error would be to improve the quality of the sample, preferably a single crystal but a solid piece of polycrystalline sample would be an improvement in scattering volume. Another way would be to reduce the background scattering detected whilst performing the experiment, this is possible with an experimental redesign into a windowless setup.

Another notable trait of sample 1 is the Nd moment drops rapidly from 2K to 20K. Between 20K and 60K, the Nd moment appears to flatten out or decrease at a slower rate; the size of the errors means that it is not possible to determine which. There are two possible conclusions to draw from this. The first is that this is a continual decay, associated with the thermal disordering of the Nd moment. The second option would be that there is a sharp drop in the Nd moment, around 20K to 30K, which could be associated with a MIT or a magnetic transition. This reading of the data would be further complicated by the fact we would still expect to see thermal disordering, on top of this feature. Whilst the errors on the data are too large to confidently conclude which of these options are happening in the samples, I personally believe the data trends to be caused exclusively by thermal disordering, as I am not confident enough is this evidence of an MIT, however further work would

definitely be needed to confirm or disprove this.

5.7.1 Future Work

To continue this work, more measurements would be necessary on both the already obtained samples and temperatures and a greater range of samples and temperatures. However, the limiting factor of these experiments is the background to signal ratio on collecting these measurements. This was caused by the moment/number of electrons in the formula unit being extremely small (as discussed above). Also, the process of compressing the samples into a pellet created very thin samples which were better able to survive the temperature and pressure changes of taking the measurements without breaking. This, along with the significantly reduced density over a crystal of $Nd_2Ir_2O_7$, drastically reduced the scattering volume and therefore also decreased the signal to noise ratio. An enhancement to this work would be to use a single crystal or a polycrystalline pellet. This would vastly improve the results because, firstly, with a single crystal the ability to look at an individual direction rather than a polycrystalline average would increase the ability to model the data obtained, and secondly, either a single crystal or a polycrystalline pellet would provide a much denser sample than the compressed powder, vastly expanding the scattering volume and therefore the signal to noise ratio.

Whilst more data would be necessary to advance this investigation, it is likely to prove difficult to improve the statistics meaningfully with the current experimental set up within any reasonable time frame. To progress this work significantly, these samples would be better measured in a windowless set up. This setup would reduce the background signal to zero as much of the background noise is caused from scattering off the windows and, therefore, would make it possible to obtain results from these samples with much greater accuracy and speed.

Chapter 6

Studies into the Spin Moments of Off-Stoichiometric NbFe$_2$

6.1   Introduction

NbFe$_2$ has generated much interest recently due to being near to a magnetic quantum critical point. Quantum critical points are where a continuous, or second order, phase transition happens at absolute zero, 0 K. Materials near these critical points have been found to have novel and interesting ground states including superconductivity [106], nematic phases [107] and magnetic order [108], attributed to quantum fluctuations around these points.

Non-stoichiometric NbFe$_2$ (Nb$_{1-y}$Fe$_{2+y}$) has a rich magnetic phase diagram. As the value of y varies, iron rich and niobium rich samples ($y \leq -0.02$ and $y \geq 0.01$ respectively) have been thought to be ferromagnetic [109], due to remnant magnetism. However both ferromagnetic and antiferromagnetic fluctuations have been found [110] and previous Compton scattering experiments have found ferrimagnetism in the iron rich range ($y = 0.015$) [111]. Within this range, near stoichiometry ($-0.02 \leq y \leq 0.01$), there has long been debate as to the ground state [108]. It has been suggested that in this range there may be spin density wave

(SDW) order [106] or long range antiferromagnetism [108]. In addition, recent work on $Nb_{0.975}Fe_{2.025}$ postulates that as the temperature is reduced, the sample transitions from paramagnetic to ferromagnetic to a spin glass order [112], implying an even more complex phase diagram.

Whilst antiferromagnetic quantum critical points are well studied, ferromagnetic quantum critical points are notoriously difficult to investigate [113]. It is theorised that approaching the putative quantum critical point, one of two scenarios take place. Either the transition becomes discontinuous, first order, or another phase, such as spin density wave order, forms at low temperature thus hiding the quantum critical point. It has been proposed that $NbFe_2$ follows this second scenario and a ferromagnetic quantum critical point is buried in the spin density wave order phase [114].

The current state of the art knowledge for these samples is limited. Comparatively few transitional metal compounds have been studied in detail until recently. In the last decade, or so, there have been a slew of studies in this area, in quick succession. The relevant studies to our investigation, and the developments made in the area, have been picked out and discussed below.

Haynes *et. al.* [111] formed the basis for the investigations completed in this chapter. It used Compton scattering to examine the magnetic properties of a particular Fe rich sample within this series. Previous work had found samples in this region to be ferromagnetic whilst this study found them to be ferrimagnetic. In particular Moroni-Klementowicz *et. al.* [115] first populated the phase diagram suggesting the SDW state which is in debate. This diagram is discussed in figure 7.6. The aim of our study was to use Compton scattering to investigate two samples, within the theorised SDW region, and experimentally determine the true magnetic ground state.

Friedmann *et. al.* [113] also expands on the previous work completed for this sample series. Their study suggests a tricritical point over the simpler quantum

critical point discussed in other studies. This is not an issue in Haynes *et. al.* as the sample investigated is outside the region this would affect but it is significant for the samples investigated in this chapter. Friedmann *et. al.* suggest that NbFe2 is the first series in which this tricritical point has been found but it goes on to suggest that it present in other sample series, a matter which needs to be addressed going forwards.

Subedi *et. al.* [107] provides a comprehensive look at the computational aspects of this sample. It discusses multiple spin configurations within $NbFe_2$ and suggests a ferrimagnetic ground state. However, whilst discussing that stoichiometry is important, and the changing of the ground state with doping, this is not included in their computational study. In addition, SDW states are not studied in detail. This study further emphasises the need to combine experimental and theoretical work, to understand this and other samples.

6.1.1 Quantum Critical Points

A typical phase is between a paramagnetic metal and some long-range order, such as ferromagnetism. Many materials display these second order phase transitions and the transition temperature can be tuned using an external parameter such as pressure or doping [116]. It has been found that tuning this transition temperature to 0 K would give rise to critical phenomena, Hertz coined the phrase quantum criticality to explain these effects [117]. A sketch of such a phase diagram is seen in figure 6.1. However, whilst a paramagnetic to ferromagnetic transition was one of the first quantum critical points to be proposed, in the majority of ferromagnets, other behaviour intervenes before the temperature can be tuned to zero [116].

Tricritical Points

Tricritical points form at a non-zero temperature, $T_{tc} > 0K$. Above this temperature, transitions are second order and below this temperature transitions are first order.
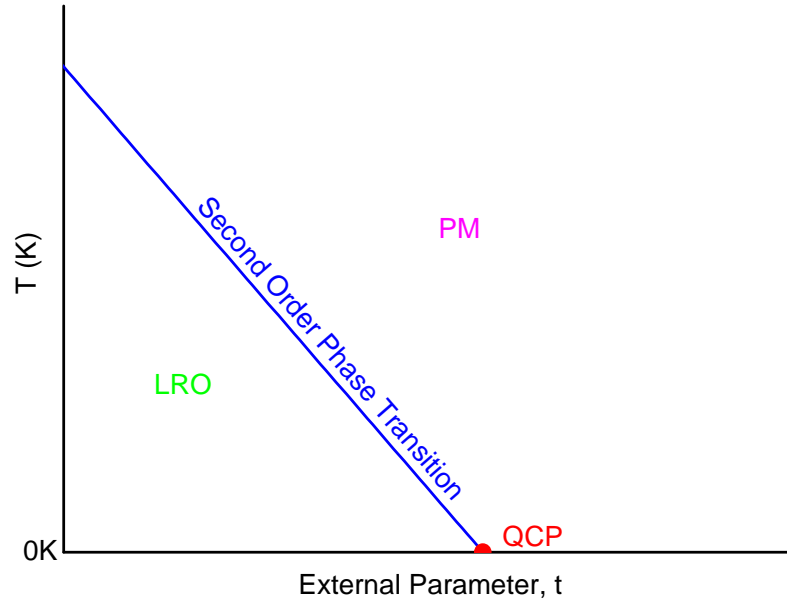
Figure 6.1: Sketch of a phase diagram with a quantum critical point (QCP) at 0 K, a continuous, second order phase transition between paramagnetism and a long-range order region. The quantum critical point is at 0 K.

However when the effect of a magnetic field is investigated, it has been found that in the three dimensional space of temperature, field and the control parameter a surface emanates from the tricritical point ending in two quantum critical points in the zero temperature plane with finite values for the magnetic field [118]. A sketch of this is shown in figure 6.2.

In $NbFe_2$ the external control parameter used for tuning is doping, that is changing the value of y in $Nb_{1-y}Fe_{2+y}$ to create iron and niobium rich samples and allowing for the tuning necessary to attempt to find quantum critical points. [119]

6.2 NbFe$_2$ Crystal Structure

$NbFe_2$ has a hexagonal C14 structure with niobium at the $4f(1/3, 2/3, x)$ and iron at the $2a(0, 0, 0)$ and $6h(z, 2z, 3/4)$ sites. Where $a = 4.8401\mathring{A}$, $c = 7.8963\mathring{A}$ [115], $x = 0.0652$ and, $z = 0.1705$. The unit cell consists of 4 formula units [106]. The structure is shown in figure 6.3. This structure and parameters were used for the
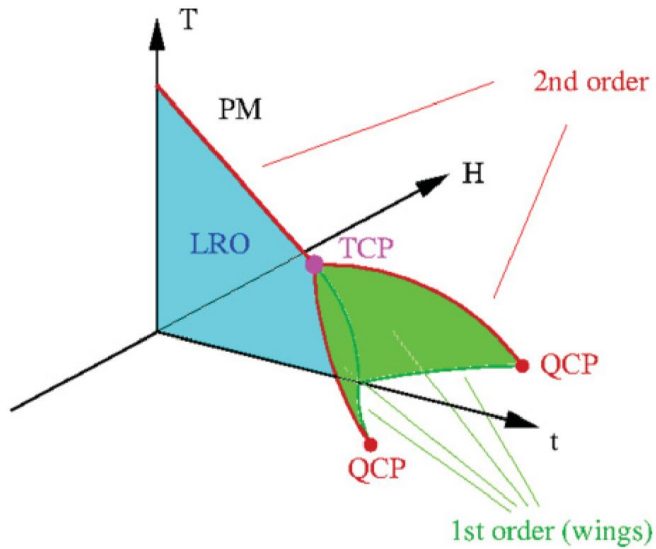
Figure 6.2: Sketch of a phase diagram with a tricritical point. Showing the quantum critical points at non-zero values of magnetic field. Adapted from [118].

full potential linearised augmented planewave code, ELK, in this chapter.

As can be seen, NbFe$_2$ forms a layered structure with alternating layers of iron on the 6h site in a hexagonal pattern and layers of niobium on the 4f site and iron on the 2a site. The niobium atoms lie within iron *cages* as is more clearly shown in figure 6.4 which illustrates a single niobium atom and its corresponding iron cage.

6.3 Electronic Structure

Several different magnetic configurations have been proposed and tested using DFT code. Ferromagnetic, ferrimagnetic and antiferromagnetic configurations have been tested in other texts [107; 111; 120] and in this thesis using the ELK DFT code. They are often tested on stoichiometric NbFe$_2$, for ease of computation, and this is the case for this chapter. The ground state configurations are chosen and the ground state energies and Compton profiles are calculated. The two possible ground state configurations that are focused on in this chapter are a *ferrimagnetic* configuration
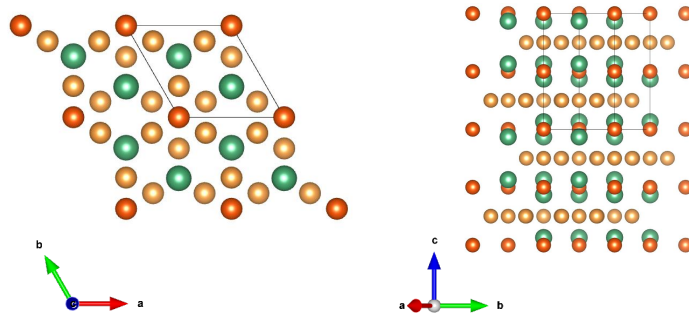
Figure 6.3: Crystal structure of NbFe$_2$. Hexagonal Laves phase space group C14 $P6_3/mmc$ (No. 194). Niobium atoms in green, iron atoms in orange ($6h$ in light orange, $2a$ in dark orange). Viewed along the c and a axis
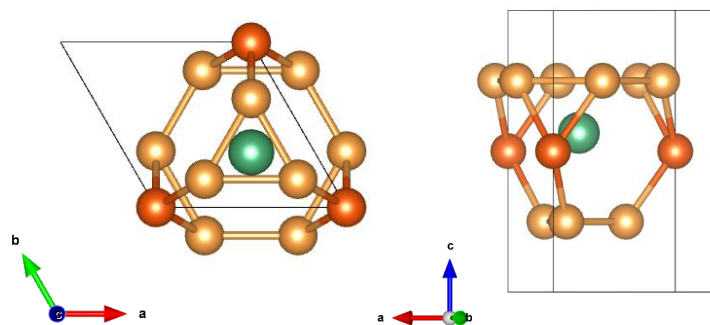
Figure 6.4: Crystal structure of NbFe$_2$ isolating a single niobium atom and the iron cage surrounding it. Niobium atoms in green, iron atoms in orange ($6h$ in light orange, $2a$ in dark orange).

where the $2a$ iron sites are anti-aligned with the $6h$ sites, and the $4f$ niobium sites are aligned with the $2a$ sites (with a much smaller moment), and also a *ferromagnetic* configuration where all the iron sites are aligned (the niobium sites are anti-aligned with the iron but with a small moment and therefore for clarity, since the iron sites are ferromagnetic, it is considered ferromagnetic). Both the ferrimagnetic and ferromagnetic configurations without the niobium sites are shown in figure 6.5.
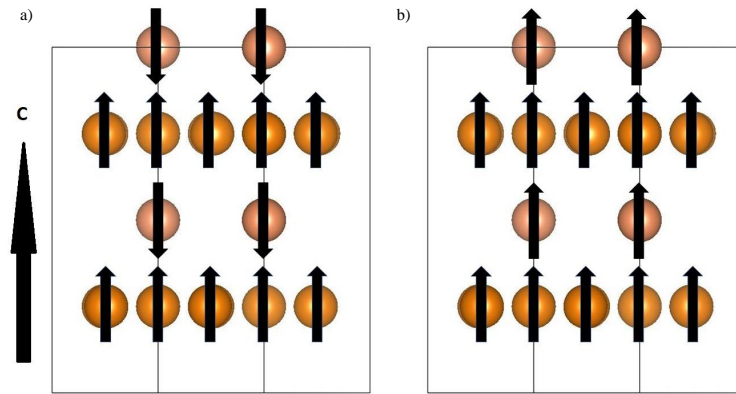
Figure 6.5: Sketch of two possible configurations of NbFe$_2$ with the iron $2a$ sites in light orange and the $6h$ iron sites in dark orange. Firstly, the ferrimagnetic case, with the iron $6h$ and the $2a$ sites antialigned and secondly the ferromagnetic case where all the iron sites are aligned.

6.4 Off-Stoichiometric Variations in the Crystal and Electronic Structure

The experimental values of a, c, x, and z in the crystal structure vary slightly for off-stoichiometric samples from the stoichiometric values quoted above. Values have been obtained for many different compositions by D. Moroni-Klementowicz *et al.* between $y = 0.2$ and $y = -0.097$ [115]. These have been found experimentally and do not include the exact compositions used in this chapter, although it has been shown that the vales of a and c decrease linearly with increasing y over the range $-0.04 \leq y \geq 0.04$ [119]. Using this fact and D. Moroni-Klementowicz *et al*

values for a and c, the values for the samples studied can be interpolated. These interpolated values can be seen in table 6.1. Comparing the off-stoichiometric values to the stoichiometric values in the table shows the extent of the variation. Whilst these values do indeed show the change, the stoichiometric values were chosen to be used for the DFT calculations in this chapter as the computational resources for calculating off-stoichiometric samples are considerable and were not available for the purposes of this thesis.

	y	a	c
Stoichiometric	0	$4.8401\mathring{A}$	$7.8963\mathring{A}$
Iron rich	0.002	$4.8398\mathring{A}$	$7.8960\mathring{A}$
Niobium rich	-0.004	$4.8410\mathring{A}$	$7.8980\mathring{A}$

Table 6.1: Lattice parameters for stoichiometric [115] and interpolated lattice parameters for off-stoichiometric [119].

The ground state electronic structure variations are one of the more interesting properties of this series of materials. It has been proposed, as stated above, that as the series progresses from iron rich to niobium rich, the ground state progresses through ferromagnetic to a complex state, generally considered to be a spin density wave state, and back to a second ferromagnetic state. A phase diagram, adapted from [111], is shown in figure 6.6. This shows the phase diagram proposed by D. Moroni-Klementowicz *et al*, with a black $\times$ marking the temperature and composition measured by T. D. Haynes *et al* and green stars marking the composition and temperature measured in this chapter.

6.5 Theoretical Calculations

Using ELK, several different electronic configurations were tested in a continuation to the A. Subedi et al paper [107]. A ferromagnetic configuration, where the $2a$ and $6h$ iron sites were aligned, and a ferrimagnetic configuration where the $2a$ and $6h$ are anti-aligned can be seen in figure 6.5.
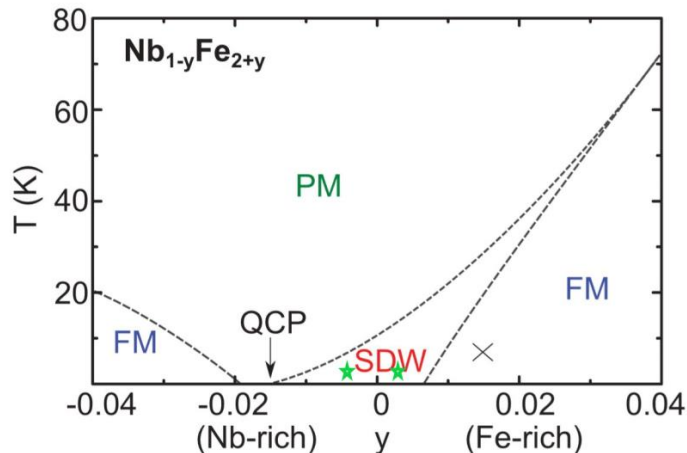
Figure 6.6: Phase diagram of $Nb_{1-y}Fe_{2+y}$. The black $\times$ marking the composition and temperature measured in [111] and the two green stars marking the composition and temperature measured in this thesis. Adapted from [111] and [115].

Both configurations were tested with both GGA and LSDA functionals, discussed in chapter 3. LSDA depends on the electronic density at any given point while GGA also depends on the gradient of the density at that point. Whilst LSDA has famously failed to calculate the correct ground state in certain materials that GGA has successfully characterised (notably iron), testing using both functionals can reveal much more information than just using GGA.

The profiles in this section (figures 6.7, 6.8, and 6.9) have been normalised so the area under the profile is equal to 1. This is done for ease of comparison as the calculated spin moments, seen in table 6.3 are so different it would not be possible to compare the shape if they are normalised to the spin moment.

These configurations were tested with and without the spin orbit coupling Hamiltonian discussed in earlier chapters. Calculations were performed to test whether the effect of spin-orbit coupling is important to the characterisation of the system in these configurations. In all cases there is no difference to the theoretical Compton profile with or without spin orbit coupling. This is illustrated in figure 6.7

where the theoretical profiles from four calculations, ferrimagnetic LSDA and ferromagnetic GGA both with and without spin orbit coupling, are shown. As can be seen there is almost complete overlap between the profiles suggesting that including spin orbit coupling in the calculations has no effect on the calculated profiles, albeit slight differences arise from the different number of k-points used in the calculation. When spin-orbit coupling is used some of the symmetry of the crystal is broken, this has the effect of reducing the number of k-points used in the calculation. When spin orbit coupling was verified as negligible, as seen in 6.7, further calculations could be performed without including spin-orbit interactions.
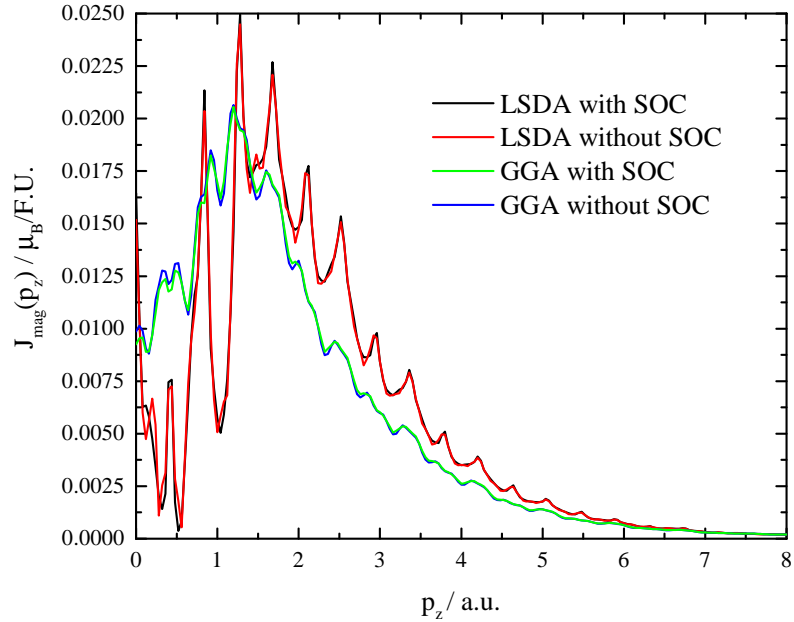
Figure 6.7: Unconvoluted theoretical magnetic Compton profiles for ferrimagnetic LSDA calculations, with and without spin orbit coupling (black and red respectively) and ferromagnetic GGA calculations, with and without spin orbit coupling (green and blue respectively), all resolved along the c axis. Normalised so $\int J_{mag} dp_z = 1$ for clarity.

The four calculations, that is, the two electron configurations using both functionals (all without spin orbit coupling), are shown in figure 6.8. As can be discerned, with both functionals, the ferrimagnetic configuration dips to a lower value at low momentum, p_z, than the ferromagnetic option.

Another feature of these profiles, especially the LSDA ferrimagnetic case (in red), is a large quantity of Umklapp features, which are caused by interactions between electrons at the Fermi level and the lattice, indicative of a rich Fermi surface [?].

Theoretical ground state energies were obtained from the two models using the two functionals, as shown in table 6.2. These are shown relative to the obtained energy from a non-spin polarised calculation run in ELK, the non-spin polarised case was renormalised to zero and the other cases relative to that. Comparing these theoretical ground state energies shows that, for the LSDA calculations, the ferrimagnetic case has a lower ground state energy, which agrees with earlier LSDA calculations [107]. However, the GGA calculations show the ferromagnetic case has a lower ground state energy, as seen in table 6.2.

Configuration	LSDA Functional	GGA Functional
Ferrimagnetic	-0.0029182	$+0.3206064$
Ferromagnetic	$+0.0167706$	-0.0037175

Table 6.2: Theoretical ground state energies for $NbFe_2$, given relative to the ground state energy of a calculated non spin polarised case. Calculations were performed in ELK and have separately used LSDA and GGA functionals. These results are given in atomic units of energy.

To compare the theoretical profiles to the experimental profiles collected at SPring8, the profiles obtained from the ELK calculations need to be convolved with a Gaussian distribution using the standard deviation of the experimental resolution, $\sigma = 0.44$ a.u.. The result of the convolution is shown in figure 6.9.

Site	LSDA, Ferri	LSDA, Ferro	GGA, Ferri	GGA, Ferro
Nb $4f$ (μ_B per site)	-0.1064	-0.3373	-0.2479	-0.2376
Fe $2a$ (μ_B per site)	-0.9510	1.7584	-4.1007	0.8946
Fe $6h$ (μ_B per site)	0.6533	1.6237	2.6415	1.3288
Total (μ_B per F.U.)	0.3734	2.9268	1.5401	2.2029

Table 6.3: Spin moments obtained theoretically from the ELK DFT code, detailing the different orientations and sizes of spin moments for the two configurations and two functionals.
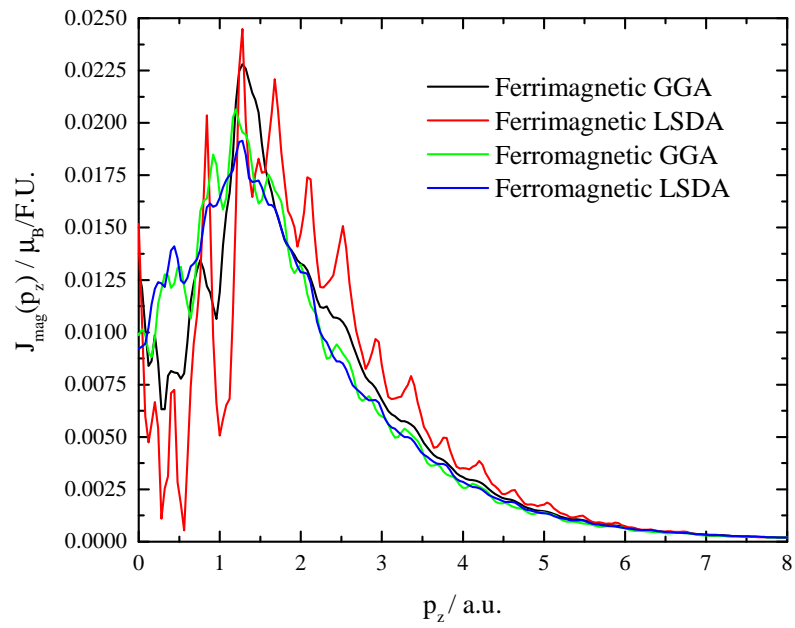
Figure 6.8: Theoretical magnetic Compton profiles. Ferrimagnetic using GGA in black, Ferrimagnetic using LSDA in red, ferromagnetic using GGA in green and finally ferromagnetic using LSDA in blue, all resolved along the c axis. All profiles have not been convoluted with experimental resolution Gaussian profile. Normalised so $\int J_{mag} dp_z = 1$ for clarity.
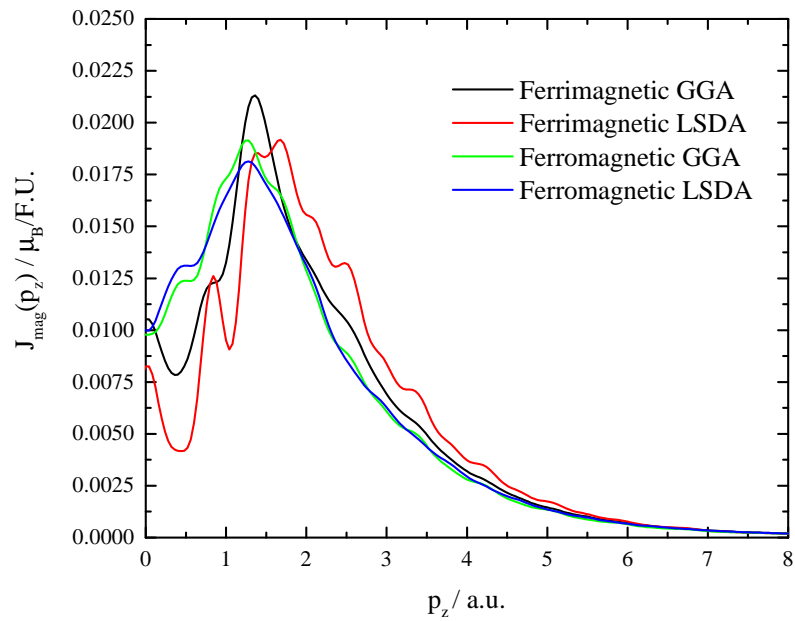
Figure 6.9: Convolved Theoretical magnetic Compton profiles. Ferrimagnetic using GGA in black, Ferrimagnetic using LSDA in red, ferromagnetic using GGA in green and finally ferromagnetic using LSDA in blue, all resolved along the c axis. (Convolved with a Gaussian distribution with $\sigma = 0.44 a.u.$). Normalised so $\int J_{mag} dp_z = 1$ for clarity.

Table 6.3 shows the spin moments calculated in ELK for the two electronic configurations and the two exchange functionals. The total moments of the two ferromagnetic calculations are similar, however, the LSDA calculation has a significantly larger moment on the $2a$ site. In contrast, the two ferrimagnetic calculations are significantly different, in both the total moment and the contributions from the sites. The much higher moments on the GGA calculations are unexpected and call for further investigations.

6.6   Experimental Results

Two different off-stoichiometric single crystal samples of $Nb_{1-y}Fe_{2+y}$ were investigated, an iron rich sample where $y = +0.002$ ($Nb_{0.998}Fe_{2.002}$) and a niobium rich sample where $y = -0.004$ ($Nb_{1.004}Fe_{1.996}$). The experiment was performed at 2K along the c-axis, the iron rich sample was measured at 1T and the niobium rich sample was measured at 2T.

In this section the computational profiles are normalised so the area under the profile is equal to the experimentally obtained spin moment. Again this is done for clarity and ease of comparison due to the variation of computational and experimental spin moments.

Starting with the iron rich sample, $y = +0.002$, the results when compared to the results for the two different functionals as shown in figure 6.10 and 6.11. With both functionals the ferrimagnetic configuration is a better fit to the experimental data than the ferromagnetic option, shown in table 6.4 showing χ^2 values for the models.

These values were calculated using a Matlab script and were calculated over all momenta. The profiles were scaled, so the area of the theoretical profiles matched those of the experimental ones, before the χ^2 was calculated. This does not take into account the different moments obtained from the ELK code, meaning that these

need to be taken into consideration when discussing the best match to the data.

This suggests that for this sample the ground state is ferrimagnetic. This sample was found to have a spin moment of $\mu_s = 0.099 \pm 0.004\mu_B$. This is much smaller than the calculated moments, likely due to the failure of the calculations to describe the spin fluctuations, which have the effect of lowering the spin moment [121].
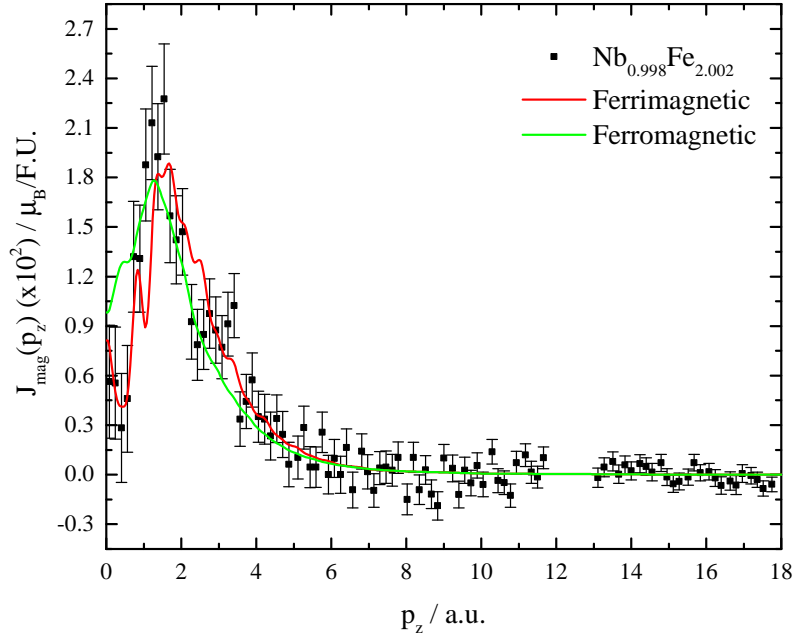
Figure 6.10: Experimental results of the iron rich sample of $Nb_{0.998}Fe_{2.002}$ in black with the LSDA functional calculation (ferrimagnetic configuration in red and ferromagnetic configuration in green)

For the niobium rich sample considerably less data was collected resulting in much larger errors. The experimentally found spin moment is $\mu_s = 0.052 \pm 0.007\mu_B$, significantly lower than the value found for the iron rich sample. Figures 6.12 and 6.13 show the experimental data plotted against the theoretical profiles.

Comparing the quality of the models to the data using a χ^2 analysis, the result are in table 6.4, these results show that for the iron rich sample, the ferrimagnetic models (with both functionals) are better fits to the data than the ferromagnetic models. The niobium rich sample shows that with the GGA functional the
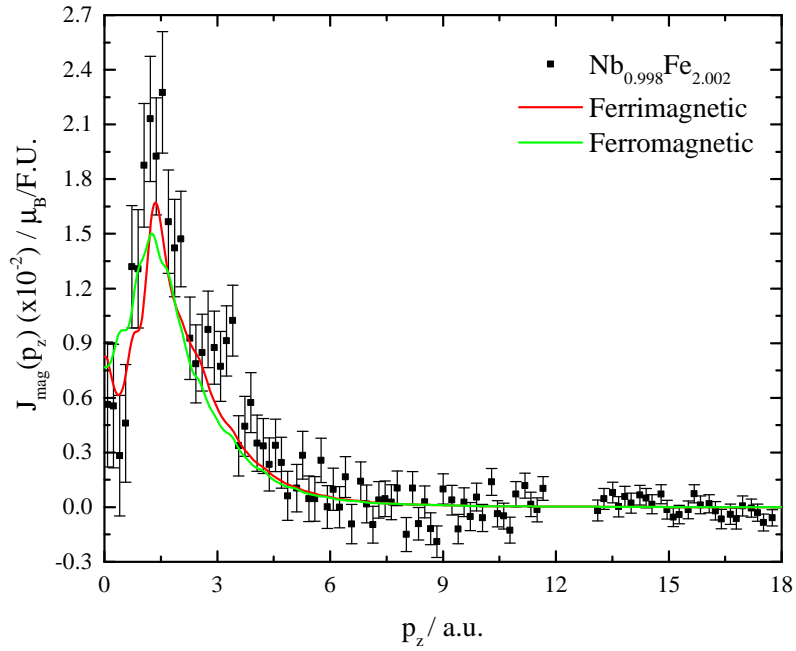
Figure 6.11: Experimental results of the iron rich sample of $Nb_{0.998}Fe_{2.002}$ in black with the GGA functional calculation (ferrimagnetic configuration in red and ferromagnetic configuration in green)
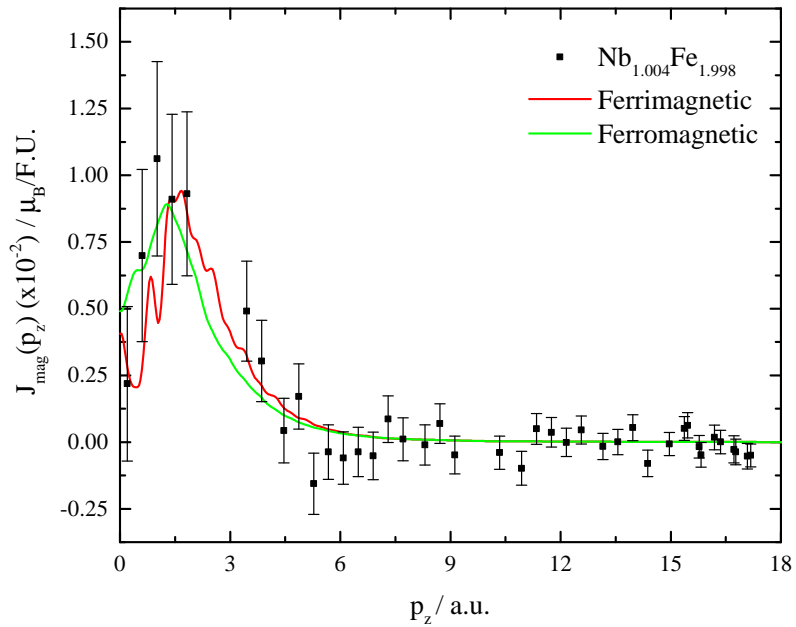
Figure 6.12: Experimental results of the niobium rich sample of $Nb_{1.004}Fe_{1.996}$ in black with the LSDA functional calculation (ferrimagnetic configuration in red and ferromagnetic configuration in green)
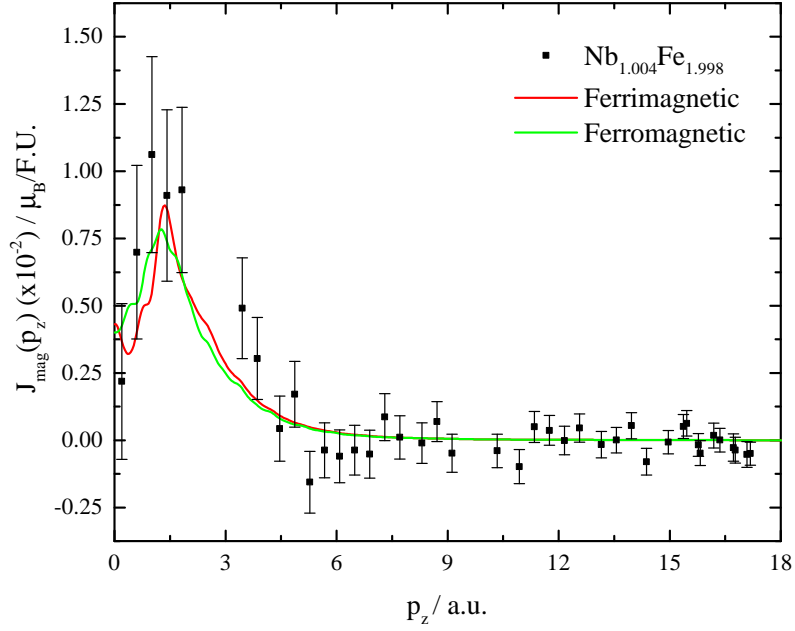
Figure 6.13: Experimental results of the niobium rich sample of $Nb_{1.004}Fe_{1.996}$ in black with the GGA functional calculation (ferrimagnetic configuration in red and ferromagnetic configuration in green)

Sample	LSDA, Ferri	LSDA, Ferro	GGA, Ferri	GGA, Ferro
$Nb_{0.998}Fe_{2.002}$	0.7694	0.9090	0.7436	0.9080
$Nb_{1.004}Fe_{1.996}$	1.4092	1.3685	1.3847	1.4067

Table 6.4: List of χ^2 values for the four models and two samples.

ferrimagnetic model fit the data better as with the other sample. However, with the LSDA functional it shows a slightly better fit with the ferromagnetic model. However, the quantity of the data and size of the errors in the niobium rich sample is much worse. This, along with the large and near identical χ^2 results, makes drawing conclusions from this data difficult as the models are arguably almost equal in the quality of the fit.

6.7 Discussion

6.7.1 Iron rich sample ($Nb_{0.998}Fe_{2.002}$)

The iron rich sample, $Nb_{0.998}Fe_{2.002}$, from comparing the magnetic Compton profile to the theory produced in ELK (figures 6.10 and 6.11), implies that the ground state is in a ferrimagnetic state where the $4f$ and the $2a$ iron sites are anti-aligned as seen in table 6.4. This is supported by the earlier LSDA stoichiometric calculations [107].

The result for the iron rich sample in this chapter contradicts the phase diagram in figure 6.6 since it is found to be in a ferrimagnetic state rather than spin density wave state expected. The most likely reason for this is that the field in which this experiment is performed takes the sample out of the spin density wave order and into a ferrimagnetic state. This can be better understood if the phase diagram is thought of with reference to the field as well. This is shown in figure 6.14, a phase diagram proposed by S. Friedemann *et al* [113]. As can be seen, a field of 1T would be outside the spin density wave region.

Considering again earlier Compton scattering experiments (on an iron rich sample of $Nb_{0.985}Fe_{2.015}$, $y = 0.015$ (black cross in figure 6.6)) performed by T. D. Haynes *et al.*, the samples were found to be in a ferrimagnetic phase [111]. However these results are contradicted by D. Rauch *et al.* who, using Mossbauer spectroscopy suggest that $Nb_{0.984}Fe_{2.016}$ is ferromagnetic [114]. This result has been confirmed by further Mossbauer studies [122] which find parallel, if smaller than theoretically expected, moments on the $2a$ and $6h$ sites. One postulated cause for this discrepancy is that the larger energy window from Compton scattering when compared to Mossbauer spectroscopy could cause slowly fluctuating moments to appear static [114]. It may also be a problem with the *ab initio* calculations used, if the Compton profile of stoichiometric $NbFe_2$ in the ferrimagnetic configuration is similar to the profile for a ferromagnetic off-stoichiometric model.
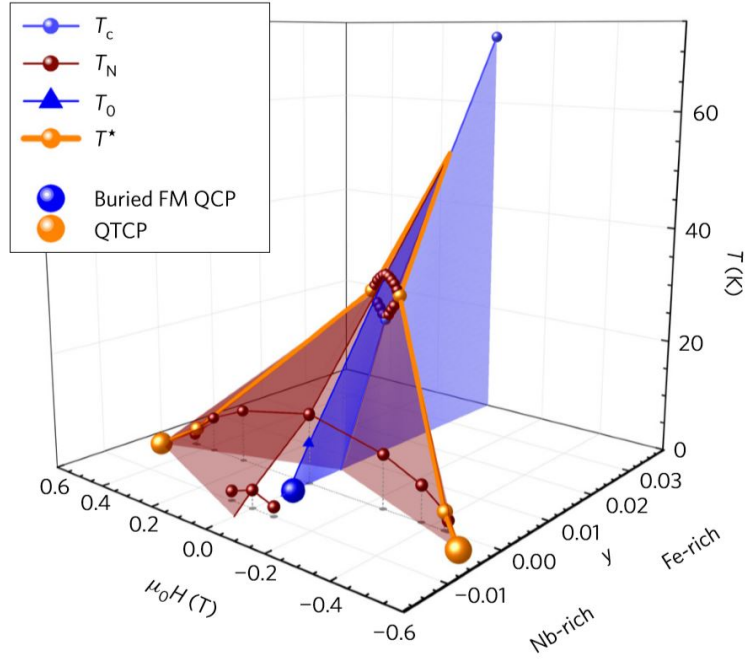
Figure 6.14: Composition-magnetic field-temperature phase diagram for $Nb_{1-y}Fe_{2+y}$. Adapted from [113].

6.7.2 Niobium Rich Sample ($Nb_{1.004}Fe_{1.996}$)

With the niobium rich sample, it has not been possible to conclude the ground state phase as the GGA calculations lowest energy is the ferromagnetic phase (table 6.2), whilst the ferrimagnetic phase has a lower χ^2 (table 6.4) and the LSDA calculations produce the opposite result. This discrepancy in the χ^2 is likely due to the quantity of this data, which is significantly less than the iron rich sample. This means that drawing conclusions on the ground state from the χ^2 values is impossible, this can be seen by eye in figures 6.12 and 6.13 (especially when compared to figures 6.10 and 6.11).

The experimental spin moments of the samples were both significantly lower than the theoretical spin moments from all the calculations seen in table 6.3. For the LSDA ferrimagnetic calculation a scaling factor of approximately 0.3 would be needed, and for the niobium rich sample a scaling factor of 0.1 is needed. T. D.

Haynes *et al* found a scaling factor of approximately 0.6 was required to match the experimental spin moment of $0.245\pm0.004\mu_B$ to their theoretical result [111]. This is probably due in part to the failure of the calculations to describe the spin fluctuations [121; 123]; However the significantly different experimental spin moments obtained suggest that this could also be accounted for, at least in part, by the fact the calculations are based on the stoichiometric system.

The difference in the calculated ground state energies in table 6.2 is interesting. Previous LSDA calculation have found the ferrimagnetic state to have the lowest energy [107], and previous measurements have found the ferrimagnetic fits the data well [111]. Nevertheless, as all these calculations work on stoichiometric systems, this may not be an accurate view of the systems measured. The complexity of the phase diagram and the substantial changes in the system, from small changes in y, shows that stoichiometry is particularly important for this series. More calculations are needed as the samples measured in this chapter, and in the earlier work by the group [111], may fit better to different configurations when calculations are performed on the true structure of the sample.

Also, it is important to note the ferrimagnetic phase is the lowest energy in the calculations in ELK, using the LSDA functional. This agrees with other calculations done by others using LSDA functionals [107; 111]. However, interestingly, using the GGA functional the lowest energy ground state is found to be the ferromagnetic state. Without a stoichiometric sample to test and compare the models against (or off-stoichiometric calculations), it is difficult to tell which configuration would be the ground state for the stoichiometric sample. However, both ferrimagnetic configurations, using both functionals, appear to fit the data better than the ferromagnetic models, with the exception of the LSDA functional for the niobium rich sample. This apparently fits the ferromagnetic better, although this is likely due to a lesser quality and quantity of data in comparison to the iron rich sample.

6.8 Conclusion

In summary, the niobium rich sample data $y = -0.004$ is inconclusive as insufficient data was collected to provide a clear distinction as to which model fits the data more closely. Using the LSDA functional the ferromagnetic calculation fits the data better and using the GGA functional the ferrimagnetic model fits better. The probable cause of this discrepancy is insufficient data and therefore, to categorise this sample, more data would need to be collected.

In contrast, the iron rich sample is more closely aligned to the ferrimagnetic stoichiometric configuration of the electronic structures tested in this chapter, as opposed to the stoichiometric ferromagnetic configuration. However it was expected for this sample to have a spin density wave order. The probable cause for the absence of this order is the size of the field applied to the samples when the profiles were measured. It is likely that the field was large enough to move out of the spin density wave phase and into the ferromagnetic or ferrimagnetic phase.

As to the debate between ferrimagnetic and ferromagnetic, whist the sample fits better to the stoichiometric ferrimagnetic calculation, further off-stoichiometric calculations are necessary to make this claim definitively. It may be that the orientation on the iron on the niobium sites (and vice versa) could change the shape of the profile enough to change the fit. Further investigations and calculations would be necessary to test this.

In addition to this there are possible features observable on the profiles, for example a noticeable jump at approximately 3 A.U.. This is fairly noticeable on the iron rich sample and arguably present on the niobium rich sample. However, with the poor quality of data, this cannot be claimed with any certainty. This feature does not appear in the computational data and further, increasingly complex, calculations may reveal the source of these jumps. With the size of these features, and the size of the error on the experimental data, there is a distinct possibility that they are

simply experimental noise. Further experimental data, along with the calculations discussed above, would be needed to truly ascertain the nature of these jumps.

6.8.1 Future Work

The next step in developing this work further would be to perform more calculations using the off-stoichiometric values. This would require using, for example, the KKR code, rather than the ELK code, although this would need considerably more computing power than was available in this thesis. This would be important to the development of this work as it would provide a better understanding of if and when the ground state changes as the value of y changes in $Nb_{1-y}Fe_{2+y}$.

Secondly more experimental data would be preferable in the niobium rich sample. The data collected for this sample, partly because it has a smaller moment, is not as accurate as that of iron rich sample.

Finally, data on more samples with different values of y across this range would provide a more complete picture of the phase diagram and how the ground state changes and if and how this effects the magnetic Compton profile.

Chapter 7

Conclusion

In this thesis, the spin densities of four samples of polycrystalline $GdCo_{5-x}Ni_x$, two samples of nominally identical $Nd_2Ir_2O_7$, and two different off-stoichiometric single crystal samples of $Nb_{1-y}Fe_{2+y}$ were measured using the magnetic Compton scattering technique (MCS) at the BL08W beamline at the SPring-8 synchrotron in the Hyōgo prefecture, Japan. This was supported by the use of density functional theory (DFT) codes, which were used to provide theoretical models that can be tested against the data. In addition to the primary technique of MCS, characterisation techniques were used on the samples, including magnetometry and Laue diffraction, in order to provide more information on the magnetic structure and to align crystals along the desired directions.

The purpose behind this work was to use MCS and the supporting techniques mentioned, along with theoretical methods, to investigate the magnetic phases and properties of the above mentioned materials.

7.1 Results

7.1.1 $\mathrm{GdCo}_{5-x}\mathrm{Ni}_x$

GdCo_5 is a member of the RETM_5 class of materials, which have many interesting magnetic properties, dependent on the rare earth species. This material was investigated for the interplay of transition metal and rare earth electrons and the compensation temperature, where the sign of the moments on the antiparallel sublattices switch and which is found in the nickel doped $\mathrm{GdCo}_{5-x}\mathrm{Ni}_x$.

Four samples of $\mathrm{GdCo}_{5-x}\mathrm{Ni}_x$, with increasing levels of nickel were investigated of which two had transition temperatures within the measurable range, namely $\mathrm{GdCo}_{3.72}\mathrm{Ni}_{1.28}$ and $\mathrm{GdCo}_3\mathrm{Ni}_2$.

$\mathrm{GdCo}_3\mathrm{Ni}_2$ has previously been experimentally shown to have a transition temperature of 230K and the work in this chapter supports this result. However, the magnetic Compton profiles have revealed more information on the behaviour of the bulk total, spin, and orbital moment. It is shown that whilst the total moment does not reach zero at the transition temperature, the spin moment passes through zero and becomes negative for a range of temperatures where the orbital moment dominates. Furthermore, using theoretical models to separate out the contributions to the spin from the gadolinium and cobalt-nickel sublattices provides a very clear picture at the point the signs on the spin moments flip. This happens at a temperature at which the gadolinium spin moment is still larger then the spin moment on the cobalt-nickel sublattice, however, the total moments on the sublattices compensate due to the orbital moment on the cobalt sites. This result can only be seen with a technique that not only measures the spin moment but is also capable of separating out the contributions to the moments, such as MCS.

With regard to $\mathrm{GdCo}_{3.72}\mathrm{Ni}_{1.28}$, a transition temperature was determined to be between $\approx 110\mathrm{K}$ and $\approx 130\mathrm{K}$. This follows the pattern of transition temperatures found in this chapter and outlined in other texts, although the large temperature

range over which the transition takes place coupled with the low spin moments makes it difficult to as accurately pin point as was determined with $GdCo_3Ni_2$.

$GdCo_4Ni$, only had one measurement taken at 300K. This measurement does not contradict any conclusions drawn from the other samples and follows the pattern expected, having a positive $3d$ moment and a negative $4f$ moment.

$GdCo_2Ni_3$ was the only sample not to repeat the pattern of the other three. The spin moments, both the total and the $3d$ and $4f$ contributions, follow the expected trend, i.e. the gadolinium moment is positive and the cobalt-nickel moment is negative albeit that the expected transition temperature of 323K was outside the experimental range. However, the orbital moment is positive and antiparallel to the cobalt-nickel $3d$ spin moment. This is a differing result from the other three samples and requires investigation to understand why this has occurred. Theoretical work using DFT codes could help to explain this anomaly. Nonetheless, it would be preferable if a repeat of the experiment, with more results from samples with a similar nickel doping could be carried out to clarify the results and aid in understanding.

7.1.2 $Nd_2Ir_2O_7$

The pyrochlore iridate $Nd_2Ir_2O_7$, has attracted interest due to a debated metal to insulator transition, both as to its temperature and even its existence, as well as the many novel magnetic phases attributed to strong spin-orbit coupling and electron correlations.

Sample 1's magnetism comprises of a $4f$ moment on the neodymium and a $5d$ moment on the iridium. Separating out these contributions to the spin moment obtained from the Compton profile gives a highly temperature dependent $4f$ moment which at 60K is approximately 20% of the value at 2K. In contrast, the iridium moment is constant, within error, over this range. The orbital moments follow a similar pattern, the neodymium moment is forced to follow the spin moment by

defining it from the spin-orbit ratio. Nonetheless, at all temperatures the iridium spin-orbit ratio is calculated to be -1 within error (albeit some of the errors are very large). This would imply that the total moment is only dependent on the neodymium spin and orbital moment. Whilst there were not enough temperatures taken on sample 5 to reach a conclusion, the temperatures measured imply the same pattern measured in sample 1, albeit with a slightly higher moment.

This is an unexpected result. As before, more information gleaned from repeating the experiments, with more measurements on both the already obtained samples and temperatures and a greater range of samples and temperatures would help clarify the reason for the generally anomalous result.

However, the limiting factor of these experiments was the signal to noise ratio on collecting these measurements. This was caused by the moment/number of electrons in the formula unit being extremely small. Also, the process used of compressing the samples into a pellet created very thin samples which, though better able to survive the temperature and pressure changes of taking the measurements, along with the significantly reduced density over a crystal of $Nd_2Ir_2O_7$, drastically reduced the scattering volume and therefore also decreased the signal to noise ratio. Whilst more data is key to advancing this investigation, it is likely to prove difficult to improve the statistics significantly with the current experimental set up.

To progress this work significantly, therefore, firstly it would be advantageous to use a single crystal or a polycrystalline lump. This would improve the results since, with a single crystal, the ability to look at an individual direction rather than a polycrystalline average would increase the ability to model the data obtained and, also, either a single crystal or a polycrystalline lump would provide a much denser sample than the compressed powder, vastly expanding the scattering volume and, therefore, the signal to noise ratio. Secondly, these samples would be better measured in a windowless set up. Such a setup would reduce the background signal to zero as much of the background noise is caused from scattering off the windows

and, therefore, it would make it possible to obtain results from these samples with much greater accuracy and speed.

7.1.3 $Nb_{1-y}Fe_{2+y}$

The interest in $NbFe_2$ is caused by the complex, composition driven phase diagram. Over a small range of y, $Nb_{1-y}Fe_{2+y}$ passes through several interesting phases, including a proposed spin density wave order and a putative quantum critical point.

In summary, the iron rich sample was more closely aligned to the ferrimagnetic stoichiometric configuration of the electronic structures tested in this chapter, compared to the stoichiometric ferromagnetic configuration. It has been suggested that at these compositions a spin density wave order is expected. The probable cause is the size of the applied field in which the samples were measured. It is likely that the external field was large enough to move out of the spin density wave phase, however it is predicted that it will move into a ferromagnetic phase rather than the ferrimagnetic phase observed. As for the debate between ferrimagnetic and ferromagnetic, whilst the sample fits better to the stoichiometric ferrimagnetic calculation, further off-stoichiometric calculations are necessary to make this claim definitively. It is possible that the orientation of the moments of the iron on the niobium sites (and vice versa) could change the shape of the profile enough change which configuration best agrees with the data.

In contrast, the niobium rich sample data $y = -0.004$ was inconclusive as it was not possible to establish a clear distinction as to which model fit the data more closely. Whilst the χ^2 values show a possible slight better fit in some of the models the nearly identical values (all significantly higher than with the iron rich sample) mean that conclusions cannot be drawn.

The next step in developing this work further would be to perform more calculations using the off-stoichiometric values. This would require using, for example, the KKR code, rather than the ELK code. A significant downside to this is that

considerably more computing power would be needed. If this could be achieved, it would provide a better understanding of if and when the ground state changes as the value of y changes in $Nb_{1-y}Fe_{2+y}$. Secondly more experimental data would be preferable in the niobium rich sample. The data collected for this sample, partly because it has a smaller moment, was not as accurate as that of the iron rich sample. Finally, data on more samples with different values of y across this range would provide a more complete picture of the phase diagram and how the ground state changes and if and how this effects the magnetic Compton profile.

Bibliography

[1] M. Cooper, P. Mijnarends, N. Shiotani, N. Sakai, A. Bansil, *X-Ray Compton Scattering.* Oxford Series on Synchrotron Radiation. OUP Oxford, 2004.

[2] A. H. Compton, *A Quantum Theory of the Scattering of X—Rays by Light Elements* Phys. Rev. **21**, (1923), 483.

[3] O. Klein and T. Nishina., *Über die Streuung von Strahlung durch freie Elektronen nach der neuen relativistischen Quantendynamik von Dirac*, Zeitschrift fr Physik A , **52**, 853 (1929).

[4] F. W. Lipps and H. A. Tolhoek. *POLARIZATION PHENOMENA OF ELECTRONS AND PHOTONS. I: GENERAL METHOD AND APPLICATION TO COMPTON SCATTERING.* Physica, 20(16):85-98, 9952

[5] F. W. Lipps and H. A. Tolhoek. *POLARIZATION PHENOMENA OF ELECTRONS AND PHOTONS. II: RESULTS FOR COMPTON SCATTERING* Physica, 20(16):385-405, 9952

[6] C. Kittel *Introduction to Solid State Physics* Wiley, (2004).

[7] J. R. Hook and H. E. Hall *Solid State Physics* Wiley (2013).

[8] J. Callaway *Quantum Theory of the Solid State* Academic Press (1991).

[9] Proc. Royal Soc. Lond. **106** 563-477 (1924).

[10] D. W. Brenner *Empirical potential for hydrocarbons for use in simulating the chemical vapor deposition of diamond films* Phys. Rev. B. **42** 9458 (1990).

[11] J. Tersoff Phys. Rev. B. **42** 6991 (1988).

[12] P. Drude *Zur Elektronentheorie der Metalle* Annalen der Physik **306** 566 (1990).

[13] P. Drude *Zur Elektronentheorie der Metalle; II. Teil. Galvanomagnetische und thermomagnetische Effecte* Annalen der Physik **308** 369 (1990).

[14] R. Leighton, *The Vibrational Spectrum and Specific Heat of a Face-Centered Cubic Crystal* Rev. Mod. Phys. **20** 165 (1948).

[15] J. Singleton *Band Theory and Electronic Properties of Solids* OUP Oxford (2001).

[16] F. Hund, *Zur Deutung verwickelter Spektren, insbesondere der Elemente Scandium bis Nickel.* Zeitschrift für Physik volume 33, pages 345–371 (1925).

[17] F. Hund, *Atomtheoretische Deutung des Magnetismus der seltenen. Erden..* Zeitschrift für Physik volume 33, pages 855–859 (1925).

[18] W. Kutzelnigg, J.D. Morgan III. *Hund's rules* Zeitschrift für Physik D Atoms, Molecules and Clusters volume 36, pages 197–214 (1996).

[19] W. Pauli *ber den Einflußder Geschwindigkeitsabhngigkeit der Elektronenmasse auf den Zeemaneffekt* Zeitschrift fr Physik **31**, 373–385 (1925)

[20] C. Zener and R. R. Heikes. *Exchange Interactions.* Rev. Mod. Phys. 25, 191 (1953).

[21] U. Larson. *The RKKY indirect exchange interaction in metals in arbitrary continuous dimension.* Phys. Lett. A **85A**, 8-9 (1981).

[22] D. E. Eastman, F.J. Himpsel, and J. A. Knapp. *Experimental Exchange-Split Energy-Band Dispersions for Fe, Co, and Ni.* Phys. Rev. Lett. 44, 95

[23] G.W. Femando, A.N. Kocharian, R.E. Watson, M. Weinert. *Stoner criterion of ferromagnetism and moment saturation in the Hubbard model with an applied magnetic field.* Physica B 230-232 (1997) 509-512.

[24] S. Blundell *Magnetism in Condensed Matter* OUP Oxford (2001).

[25] J Laukkanen, K Hmlinen and S Manninen. *The absolute double-differential Compton scattering cross section of Cu 1s electrons.* J. Phys.: Condens. Matter 8 (1996) 2153–2162.

[26] M.J. Cooper, C. Shenton-Taylor, J.A. Duffy, C.A. Steer, L.V. Blaauw, *A Short History of Magnetic Compton Scattering*, Nucl. Instr. and Meth. A 580 (2007) 1.

[27] M. Cooper, E. Zukowski, S. P. Collins, D. N. Timms, F. Itoh, H. Sakurai, *Does magnetic Compton scattering only measure spin magnetization?.* J. Phys. Condens. Matter **4** L399 (1992).

[28] J. E. McCarthy, J. A. Duffy, C. Detlefs, M. J. Cooper, and P. C. Canfield, *4f spin density in the reentrant ferromagnet $SmMn_2Ge_2$.* Phys. Rev. B **62** R6073 (2000).

[29] University of Graz, The Elk Code, *http://elk.sourceforge.net/* 15/09/2021.

[30] D. Singh *Planewaves, Pseudopotentials, and the LAPW Method* Springer, (2006).

[31] John P. Perdew and Yue Wang. *Accurate and simple analytic representation of the electron-gas correlation energy.* Phys. Rev. B **45** 13244 (1992).

[32] John P. Perdew, Kieron Burke, and Matthias Ernzerhof. *Generalized Gradient Approximation Made Simple.* Phys. Rev. Letts. **77**, 3865 (1996).

[33] E L Peltzer y Blanc, C O Rodrguez, J Shitu and D L Novikov. *Degree of localization of the exchange-correlation hole and its influence on the ground-state (structural and magnetic) properties of d metals.* J. Phys. Condens. Matter **13** 9463, (2001).

[34] University of Graz, The Elk Code Manual, *https://elk.sourceforge.io/elk.pdf* 15/09/2021.

[35] M. Schmidt, K. Baldridge, J. Boatz, S. Elbert, M. Gordon, J. Jensen, S. Koseki, N. Matsunaga, K. Nguyen, S. Su, T. Windus, M. Dupuis and J. Montgomery Jr. *General Atomic and Molecular Electronic Structure System.* J. Comput. Chem **14** 11, 1347-1363 (1993).

[36] J. G. Valatin. *Generalized Hartree-Fock Method* Phys. Rev. **122** 4 (1961)

[37] M. Lasinski, N. Romero, S. Brown, and J. Blaudeau. *Recent performance improvements to the DFT and TDDFT in GAMESS* J. Comput. Chem **33** 7, 723-731 (2012).

[38] G Srivastava, *Broyden's method for self-consistent field convergence acceleration.* J. Phys. A **17** L317 (1984).

[39] K.T. Compton, E.A. Trousdale, *The Nature of the Ultimate Magnetic Particle,* Phys. Rev. 5 (1915) 315

[40] A.H. Compton, *The Spectrum of Scattered X-Rays,* Phys. Rev. 22 (1923) 409.

[41] N. Sakai and K. Ono, *Compton Profile Due to Magnetic Electrons in Ferromagnetic Iron Measured with Circularly Polarized γ Rays,* Phys. Rev. Lett. 37 (1976) 351.

[42] R.S. Holt, D. Laundy, D.A. Cardwell, M. Cooper, T. Naylor, *Polarized X-Ray Study of the Spin-Dependent Compton Profile of Ferromagnetic Iron ,* Nucl. Instr. and Meth. A 243 (1986) 608

[43] M.J. Cooper, S.P. Collins, D.N. Timms, A. Brahmia, P.P. Kane, R.S. Holt, D. Laundy, *Magnetic Anisotropy in the Electron Momentum Density of Iron* , Nature (London) 333 (1988) 151.

[44] G. W. C. Kaye, and T. H. Laby. *Kaye and Laby Tables of Physical Chemical Constants.* [Middlessex, England]: National Physical Laboratory, 2005.

[45] P. Holm. *Relativistic Compton cross section for general central-field Hartree-Fock wave functions.* Phys. Rev. A **37** 3706-3719 (1988).

[46] Y. Kubo and S. Asano. *Magnetic Compton profiles of iron and nickel.* Phys. Rev. B **42** 4431 (1990).

[47] H. Danan, A. Herr, and A. J. P. Meyer. *New Determinations of the Saturation Magnetization of Nickel and Iron.* Journal of Applied Physics **39**,669 (1968).

[48] H. Wiedemann *Synchrotron Radiation. In: Particle Accelerator Physics.* Springer, Berlin, Heidelberg. (2003).

[49] B. Kincaid *A short-period helical wiggler as an improved source of synchrotron radiation* J. Appl. Phys 48, 2684 (1977);

[50] J. Pfluger and G. Heintze. *The Asymmetric Wiggler at HASYLAB* Nucl. Instrum. Methods Phys. Res A289 (1990) 300-306

[51] R. L. Fagaly *Superconducting quantum interference device instruments and applications* Rev. Sci. Instrum. 77, 101101 (2006)

[52] D. O. Smith. *Development of a Vibrating-Coil Magnetometer.* Rev. Sci. Instrum **27** 261-268 (1956).

[53] K Kumar. $RETM_5$ and RE_2TM_{17} *permanent magnets development.* J. Appl. Phys. 63 R13 (1988).

[54] K. Strnat, G. Hoffer, J. Olson, and W. Ostertag. *A Family of New Cobalt-Base Permanent Magnet Materials.* J. Appl. Phys. **38**, 1001 (1967).

[55] C.E. Patrick, , Santosh Kumar, Geetha Balakrishnan, Rachel S. Edwards, Martin R. Lees, Eduardo Mendive-Tapia, Leon Petit, and Julie B. Staunton. *Rare-earth/transition-metal magnetic interactions in pristine and (Ni,Fe)-doped YCo_5 and $GdCo_5$.* Phys. Rev. Mater. **1**, 024411 (2017).

[56] Amy L. Tedstone, Christopher E. Patrick, Santosh Kumar, Rachel S. Edwards, Martin R. Lees, Geetha Balakrishnan, and Julie B. Staunton. *Structural and magnetic properties of $GdCo_{5x}Ni_x$.* Phys. Rev. Mater. **3** 034409 (2019).

[57] D. Gignoux, D.Givord, A.Del Moral. *Magnetic properties of $Gd_xY_{1x}Ni_5$ alloys.* Solid State Commun. **19**, 891 (1976).

[58] R. M. Grechishkin and M. S. Kustov. *Thermoreversible permanent magnets in the quasibinary $GdCo_{5x}Cu_x$ system.* Appl. Phys. Lett. **89**, 122505 (2006).

[59] K.H. Bushchow and M. Brouha. *Narrow Bloch walls in the RCo_5-type rare-earth–cobalt compounds.* J. Appl. Phys. **47** 1653 (1976).

[60] Y.C. Chuang and C. H. Wu. *Investigation of the Structure and Phase Equilibria of $Nd(Co_{1-x}M_x)_5$ Compounds (M = Ni, Cu, Al)* J. Less-Common Met. **78**, 219 (1981).

[61] J. P. Liu, X. P. Zhong, F. R. de Boer, and K. H. J. Buschow. *Magnetic coupling in $CaCu_5$-type rare earth cobalt compounds.* J. Appl. Phys. **69** 5536 (1991).

[62] E. Burzo, V. Pop. *Magnetic behaviour of $GdCo_{4-x}Ni_xAl$ intermetallic compounds.* J. Magn. Magn. Mater. **196-197** 768 (1999).

[63] A. Ermolenko. *Magnetocrystalline anisotropy of rare earth intermetallics.* IEEE Trans. Magn. **12** 992 (1976).

[64] J. Deportes, D. Givord, J. Schweizer, and F. Tasset. *Different contributions of the two cobalt sites to the magnetocrystalline anisotropy of YCo5and related compounds.* IEEE Trans. Magn. 12, 1000 (1976).

[65] E. A. Nesbitt, R. H. Willens, R. C. Sherwood, E. Buehler, and J. H. Wernick. *New Permanent Magnet Materials.* Appl. Phys. Lett. **12**, 361 (1968).

[66] A.M Mulders, C.T Kaiser, P.C.M Gubbens, A Amato, F.N Gygax, M Pinkpank, A Schenck, P.Dalmas de Réotier, A Yaouanc, K.H.J Buschow, F Kayzel, A Menovsky. *Positive muon diffusion and localization sites in $GdNi_5$*, Physica B Condens. Matter 289-290 (2000).

[67] A. Bajorek, G.Chełkowska, and B.Andrzejewski. *Magnetic properties, crystal and electronic structure of $GdNi_{5x}Cu_x$ series.* J. Alloy. Compd **509**, 578 (2011).

[68] E. A. Nesbitt, J. H. Wernick, and E. Corenzwit. *Magnetic Moments of Alloys and Compounds of Iron and Cobalt with Rare Earth Metal Additions.* J. Appl. Phys. **30** 365 (1959).

[69] K. H. J. Buschow. *Intermetallic compounds of rare-earth and 3d transition metals.* Rep. Prog. Phys. **40** 1179 (1977).

[70] K. Nassau, L.V.Cherry, and W.E.Wallace. *Intermetallic compounds between lanthanons and transition metals of the first long period: II—Ferrimagnetism of AB_5 cobalt compounds.* J. Phys. Chem. Solids **16** 131-137 (1960).

[71] O. Isnard, Y. Skourski, L. V. B. Diop, Z. Arnold, A. V. Andreev, J. Wosnitza, A. Iwasa, A. Kondo, A. Matsuo, and K. Kindo. *High magnetic field study of the Gd-Co exchange interactions in $GdCo_{12}B_6$.* J. Appl. Phys. **111** 093916 (2012).

[72] M. D. Kuz'min, Y. Skourski, D. Eckert, M. Richter, K.-H. Müller, K. P. Skokov, and I. S. Tereshina. *Spin reorientation in high magnetic fields and the Co-Gd exchange field in $GdCo_5$.* Phys. Rev. B. **70** 172412 (2004).

[73] C.E. Patrick, Santosh Kumar, Kathrin Gtze, Matthew J Pearce, John Singleton, George Rowlands, Geetha Balakrishnan, Martin R Lees, Paul A Goddard and Julie B Staunton. *Field-induced canting of magnetic moments in GdCo5 at finite temperature: first-principles calculations and high-field measurements.* J. Phys.: Condens. Matter **30** 32 (2018).

[74] W. Liu, H. Han, L. Ma, L. Pi, L. Zhang, and Y. Zhang. *Different pressure effects in $A_2Ir_2O_7$ (A=Gd, Eu, and Sm).* J. Alloy. Compd. **741** 182-187 (2018).

[75] Xiangang Wan, Ari M. Turner, Ashvin Vishwanath, and Sergey Y. Savrasov. *Topological semimetal and Fermi-arc surface states in the electronic structure of pyrochlore iridates.* Phys. Rev. B 83, 205101 (2011)

[76] S. M. Disseler, C. Dhital, T. C. Hogan, A. Amato, S. R. Giblin, C. de la Cruz, A. Daoud-Aladine, S. D. Wilson, and M. J. Graf. *Magnetic order and the electronic ground state in the pyrochlore iridate $Nd_2Ir_2O_7$* Phys. Rev. B **85**, 174441 (2012).

[77] D. Yanagishima and Y. Maeno. *Metal-Nonmetal Changeover in Pyrochlore Iridates.* J. Phys. Soc. Jpn. 70, 2880 (2001).

[78] K. Matsuhira, M. Wakeshima, R. Nakanishi, T. Yamada, A. Nakamura, W. Kawano, S. Takagi, and Y. Hinatsu. *Metal–Insulator Transition in Pyrochlore Iridates $Ln_2Ir_2O_7$ (Ln = Nd, Sm, and Eu).* J. Phys. Soc. Jpn. 76, 043706 (2007).

[79] Z. Tian, Yoshimitsu Kohama, Takahiro Tomita, Hiroaki Ishizuka, Timothy H. Hsieh, Jun J. Ishikawa, Koichi Kindo, Leon Balents, and Satoru Nakatsuji. *Field-induced quantum metal–insulator transition in the pyrochlore iridate $Nd_2Ir_2O_7$.* Nature Phys. **12**, 134-138 (2015).

[80] Zach Porter, Eli Zoghlin, Samuel Britner, Samra Husremovic, Jacob P. C. Ruff, Yongseong Choi, Daniel Haskel, Geneva Laurita, and Stephen D. Wilson. *Evo-*

lution of structure and magnetism across the metal-insulator transition in the pyrochlore iridate $(Nd_{1-x}Ca_x)_2Ir_2O_7$. Phys. Rev. B **100** 054409 (2019).

[81] Hongbin Zhang, Kristjan Haule, and David Vanderbilt. *Metal-Insulator Transition and Topological Properties of Pyrochlore Iridates.* Phys. Rev. lett. **118** 026404 (2017).

[82] Hiroshi Takatsu, Kunihiko Watanabe, Kazuki Goto, and Hiroaki Kadowaki. *Comparative study of low-temperature x-ray diffraction experiments on $R_2Ir_2O_7$ (R = Nd, Eu, and Pr).* Phys. Rev. B **90**, 235110 (2014).

[83] Svein Stølen, Reidar G.Trønnes. *The perovskite to post-perovskite transition in $CaIrO_3$: Clapeyron slope and changes in bulk and shear moduli by density functional theory.* Phys Earth Planet In. **164** 50-62 (2007).

[84] A. Subedi. *First-principles study of the electronic structure and magnetism of $CaIrO_3$.* Phys. Rev. B **85** 020408(R) (2012).

[85] Jaehong Jeong, Yvan Sidis, Alex Louat, Véronique Brouet Philippe Bourges. *Time-reversal symmetry breaking hidden order in $Sr_2(Ir,Rh)O_4$.* Nat. Commun. **8** 15119 (2017).

[86] J. Fujioka, T. Okawa, A. Yamamoto, and Y. Tokura. *Correlated Dirac semimetallic state with unusual positive magnetoresistance in strain-free perovskite $SrIrO_3$.* Phys. Rev. B **95** 121102(R) (2017).

[87] D. Pesin, and L. Balents. *Mott physics and band topology in materials with strong spin–orbit interaction.* Nature Phys. **6** 376-381 (2010).

[88] William Witczak-Krempa and Yong Baek Kim. *Topological and magnetic phases of interacting electrons in the pyrochlore iridates.* Phys. Rev. B **85** 045124 (2012).

[89] Bohm-Jung Yang and Naoto Nagaosa. *Emergent Topological Phenomena in Thin Films of Pyrochlore Iridates*. Phys. Rev. Lett. **112** 246402 (2014).

[90] William Witczak-Krempa, Ara Go, and Yong Baek Kim. *Pyrochlore electrons under pressure, heat, and field: Shedding light on the iridates*. Phys. Rev. B **87** 155101 (2013).

[91] Y. Tokiwa, J. J. Ishikawa, S. Nakatsuji, and P. Gegenwart. *Quantum criticality in a metallic spin liquid*. Nature Mater., **13** 356-359 (2014).

[92] S. Nakatsuji, Y. Machida, Y. Maeno, T. Tayama, T. Sakakibara, J. van Duijn, L. Balicas, J. N. Millican, R. T. Macaluso, and Julia Y. Chan. *Metallic Spin-Liquid Behavior of the Geometrically Frustrated Kondo Lattice $Pr_2Ir_2O_7$*. Phys. Rev. Lett. **96** 087204 (2006).

[93] Yo Machida, Satoru Nakatsuji, Shigeki Onoda, Takashi Tayama Toshiro Sakakibara. *Time-reversal symmetry breaking and spontaneous Hall effect without magnetic dipole order*. Nature **463** 210-213 (2010).

[94] Kazuyuki Matsuhira, Makoto Wakeshima, Yukio Hinatsu, and Seishi Takagi. *Metal–Insulator Transitions in Pyrochlore Oxides $Ln_2Ir_2O_7$*. J. Phys. Soc. Jpn. **80** 094701 (2011).

[95] Keisuke Tomiyasu, Kazuyuki Matsuhira, Kazuaki Iwasa, Masanori Watahiki, Seishi Takagi, Makoto Wakeshima, Yukio Hinatsu, Makoto Yokoyama, Kenji Ohoyama, and Kazuyoshi Yamada. *Emergence of Magnetic Long-range Order in Frustrated Pyrochlore $Nd_2Ir_2O_7$ with Metal–Insulator Transition*. J. Phys. Soc. Jpn. **81** 034709 (2012).

[96] S. M. Disseler, S. R. Giblin, Chetan Dhital, K. C. Lukas, Stephen D. Wilson, and M. J. Graf. *Magnetization and Hall effect studies on the pyrochlore iridate $Nd_2Ir_2O_7$*. Phys. Rev. B **87**, 060403(R) (2013).

[97] K. Ueda, J. Fujioka, C. Terakura, and Y. Tokura. *Pressure and magnetic field effects on metal-insulator transitions of bulk and domain wall states in pyrochlore iridates.* Phys. Rev. B **92** 121110(R) (2015).

[98] Nobuyuki Taira, Makoto Wakeshima, and Yukio Hinatsu. *Magnetic properties of iridium pyrochlores $R_2Ir_2O_7$ (R = Y, Sm, Eu and Lu).* J. Phys.: Condens. Matter **13**, 5527-5533 (2001).

[99] M J Graf, S M Disseler, C Dhital, T Hogan, M Bojko, A Amato, H Luetkens, C Baines, D Margineda, S R Giblin, M Jura, and S D Wilson. *Magnetism and magnetic order in the pyrochlore iridates in the insulator-to-metal crossover region.* J. Phys.: Conf. Ser. **551**, 012020 (2014).

[100] Kazuyuki Matsuhira, Masashi Tokunaga, Makoto Wakeshima, Yukio Hinatsu, and Seishi Takagi. *Giant Magnetoresistance Effect in the Metal–Insulator Transition of Pyrochlore Oxide $Nd_2Ir_2O_7$.* J. Phys. Soc. Jpn. **82**, 023706 (2013).

[101] Georgios L. Stamokostas and Gregory A. Fiete. *Mixing of $t_{2g}e_g$ orbitals in 4d and 5d transition metal oxides.* Phys. Rev. B **97**, 085150 (2018).

[102] B. J. Kim, Hosub Jin, S. J. Moon, J.-Y. Kim, B.-G. Park, C. S. Leem, Jaejun Yu, T. W. Noh, C. Kim, S.-J. Oh, J.-H. Park, V. Durairaj, G. Cao, and E. Rotenberg. *Novel J_{eff} = 1/2 Mott State Induced by Relativistic Spin-Orbit Coupling in Sr_2IrO_4.* Phys. Rev. lett. **101**, 076402 (2008).

[103] T. Arima. *Time-Reversal Symmetry Breaking and Consequent Physical Responses Induced by All-In-All-Out Type Magnetic Order on the Pyrochlore Lattice.* J. Phys. Soc. Jpn. **82** 013705 (2013).

[104] Woo Jin Kim, John H. Gruenewald, Taekoo Oh, Sangmo Cheon, Bongju Kim, Oleksandr B. Korneta, Hwanbeom Cho, Daesu Lee, Yoonkoo Kim, Miyoung Kim, Je-Geun Park, Bohm-Jung Yang, Ambrose Seo, and Tae Won Noh.

Unconventional anomalous Hall effect from antiferromagnetic domain walls of $Nd_2Ir_2O_7$ thin films. Phys. Rev. B **98** 125103 (2018).

[105] Jun J. Ishikawa, Eoin C. T. O'Farrell, and Satoru Nakatsuji. *Continuous transition between antiferromagnetic insulator and paramagnetic metal in the pyrochlore iridate $Eu_2Ir_2O_7$.* Phys. Rev. B **85**, 245109 (2012).

[106] Brian P. Neal, Erik R. Ylvisaker, and Warren E. Pickett. *Quantum criticality in $NbFe_2$ induced by zero carrier velocity.* Phys. Rev. B **84**, 085133 (2011).

[107] Alaska Subedi and David J. Singh. *Band structure and itinerant magnetism in quantum critical $NbFe_2$.* Phys. Rev. B **81**, 024422 (2010).

[108] D. Margineda, J. A. Duffy, J. W. Taylor, S. R. Giblin. *μSR study of stoichiometric $NbFe_2$.* Physica B **504** (2017) 121-126.

[109] W. J. Duncan, O. P. Welzel, D. Moroni-Klementowicz, C. Albrecht, P. G. Niklowitz, D. Grner, M. Brando, A. Neubauer, C. Pfleiderer, N. Kikugawa, A. P. Mackenzie, and F. M. Grosche. *Quantum phase transitions in $NbFe_2$ and $Ca_3Ru_2O_7$.* Phys. Status Solidi B **247**. 544 (2010).

[110] Dennis Moroni Klementowicz, Richard Burrell, David Fort, and Malte Grosche. *Quantum criticality in the frustrated Laves phase compound $NbFe_2$.* Physica B **359-361**, 80-82 (2005).

[111] T. D. Haynes, I. Maskery, M. W. Butchers, J. A. Duffy, J. W. Taylor, S. R. Giblin, C. Utfeld, J. Laverock, S. B. Dugdale, Y. Sakurai, M. Itou, C. Pfleiderer, M. Hirschberger, A. Neubauer, W. Duncan, and F. M. Grosche. *Ferrimagnetism in Fe-rich $NbFe_2$.* Phys. Rev. B **85**, 115137 (2012).

[112] Maria Bałanda, and Stanislaw M.Dubiel. *On the magnetism of the C14 $Nb_{0.975}Fe_{2.025}$ Laves phase compound: Determination of the H-T phase diagram.* J. Magn. Magn. Mater. **454** 386-391 (2018).

[113] Sven Friedemann, Will J. Duncan, Max Hirschberger, Thomas W. Bauer, Robert Kchler, Andreas Neubauer, Manuel Brando, Christian Pfleiderer, and F. Malte Grosche. *Quantum tricritical points in NbFe$_2$*. Nature Physics **14** 62 (2018).

[114] D. Rauch, M. Kraken, F. J. Litterst, S. Süllow, H. Luetkens, M. Brando, T. Förster, J. Sichelschmidt, A. Neubauer, C. Pfleiderer, W. J. Duncan, and F. M. Grosche. *Spectroscopic study of metallic magnetism in single-crystalline $Nb_{1y}Fe_{2+y}$*. Phys. Rev. B **91** 174404 (2015).

[115] D. Moroni-Klementowicz, M. Brando, C. Albrecht, W. J. Duncan, F. M. Grosche, D. Grüner, and G. Kreiner. *Magnetism in $Nb_{1y}Fe_{2+y}$: Composition and magnetic field dependence.* Phys. Rev. B **79**, 224410 (2009).

[116] G. J. Conduit, A. G. Green, and B. D. Simons. *Inhomogeneous Phase Formation on the Border of Itinerant Ferromagnetism.* Phys Rev Lett **103** 207201 (2009).

[117] J. A. Hertz. Quantum critical phenomena. Phys. Rev. B. **14** 1165 (1976).

[118] T. R. Kirkpatrick and D. Belitz. *Universal low-temperature tricritical point in metallic ferromagnets and ferrimagnets.* Phys. Rev. B **85** 134451 (2012).

[119] Masayuki Shiga, and Yoji Nakamura. *Magnetic Properties of Stoichiometric and Off-Stoichiometric NbFe$_2$*. J. Phys. Soc. Jpn. **56** 4040-4046 (1987).

[120] D. A. Tompsett, R. J. Needs, F. M. Grosche, and G. G. Lonzarich. *Doping-driven magnetic instabilities and quantum criticality of NbFe$_2$*. Phys. Rev. B **82** 155137 (2010).

[121] A. Aguayo, I. I. Mazin, and D. J. Singh. *Why Ni_3Al Is an Itinerant Ferromagnet but Ni_3Ga Is Not.* Phys. Rev. Letts. **92** 147201 (2004).

[122] Jan ukrowski1 and Stanislaw M. Dubiel. *Mssbauer-effect study of dynamic, magnetic, and electronic properties of C14 Laves phase $Nb_{0.975}Fe_{2.025}$*. J. Appl. Phys. **123** 223902 (2018).

[123] M. W. Butchers, J. A. Duffy, J. W. Taylor, S. R. Giblin, S. B. Dugdale, C. Stock, P. H. Tobash, E. D. Bauer, and C. Paulsen. *Determination of spin and orbital magnetization in the ferromagnetic superconductor UCoGe*. Phys. Rev. B **92**, 121107(R) (2015).